Designing of Iron Group Metallic Nanomaterials via Electroless Deposition

Makoto Kawamori

Department of Materials Science and Engineering,

Kyoto University

2013

Contents

Chapter 1

General Introduction

1.1 Introduction

Iron group metallic nanomaterials are attractive for a wide variety of applications, and thus, numerous fabrication methods of metallic nanomaterials have been reported. Among them, the electroless deposition is one of the most promising approaches for practical applications. The aim of the present thesis is to establish a scientific principle for designing iron group metallic nanomaterials by electroless deposition. In order to control the fabrication process of metallic nanomaterials via electroless deposition, a systematic study to explore their formation mechanism in solution is required. For this purpose, the electrochemical approaches are applied to precisely evaluate the state of the metallic nanomaterials, which is one of the important achievements in the present study. That is a mixed potential measurement, quartz crystal microbalance measurement, and cyclic voltammetry.

In the first chapter, a brief overview of applications of metallic nanomaterials is described, from zero-dimensional (0D) nanoparticles to 1D nanowires and furthermore 3D nano-archtectures. Then, the fabrication methods of metallic nanomaterials are reviewed, including the electroless deposition. Finally, the general description of lithium ion batteries is described as an application of iron group metallic nanomaterials, where we propose the novel concept of high-cyclability electrode for lithium ion batteries. The outline of the present study will be formed at the end of this chapter.

1.2 Iron group nanomaterials; from 0D nanoparticles to 3D nano-architectures

Zero-dimensional nanoparticles have received considerable attention, both theoretically and experimentally, due to their unique magnetic,[1,2] electronic,[3,4] optical,[5,6] and catalytic properties,[7,8] which are occasionally different from these of the bulk. Especially, the nanoparticles of iron group metals (i.e. Fe, Co, Ni) and their alloys have been extensively investigated because of various applications, for example, hard magnetic nanoparticles with high crystal magnetic anisotropy (such as Fe-Pt, Fe-Pd, and Co-Pt) for high density recording devices.[9-11] On the other hand, soft magnetic nanoparticles with large permeability and high saturation magnetization (such as Fe, Fe-Co, Co-Ni, and Fe-Ni) are believed to be candidates for applications such as read-write heads of magnetic storage devices,[12] magnetic fluids,[13] MRI agents,[14] drug delivery,[15] and antennas,[16] etc. Additionally, it is noted that the nanoparticles of iron group metals work as good catalysts for the formation of carbon nanotubes,[17] an oxidation reaction of hydrazine,[18,19] and evolution of hydrogen gas.[20]

The dimensional extension of nanoparticles to 1D and 3D nanomaterials results in more varieties of applications. For example, 1D nanowires have been paid a great attention because of their unique properties resulting from uniaxial anisotropies. Taking advantages of the magnetic shape anisotropies and their 1D shapes, metallic nanowires are used for high density recording devices,[21-23] transparent conductive films,[24] and anisotropic conductive films.[25] Recently, the 3D interconnected nano-architectures, such as nanopillar arrays,[26,27] inverse opal structures,[28] and nanoporous materials,[29,30] have also attracted attention due to their potential applications in rechargeable batteries, as discussed in the section 1.4.

1.3 Electroless deposition

Owing to the great efforts by many researchers, the significant progress has been made regarding 0D nanostructures. For example, a lot of methods have already been developed for synthesizing nanoparticles with wide variety of materials and well-controlled sizes. Numerous synthesis processes of iron group alloy nanoparticles have been reported using hydrogen plasma-metal reduction,[31] thermal decomposition,[32] magnetron sputtering,[33] gas reduction in a biopolymer,[34] gas reduction combined with a sol-gel method,[35,36] polyol reduction,[37,38] reverse micelle method,[39,40] and electroless deposition.[41,42]

Compared to the nanoparticles, the few researches for fabrication of 1D nanostructures has been reported until very recently because of more difficulties associated with the fabrication of nanostructures with well-controlled dimensions, morphology, and chemical composition.[43] 1D nanostructures can now be fabricated by a number of advanced techniques based on six different strategies[43]; (i) a dictation by the anisotropic crystallographic structure of a solid,[44] (ii) confinement by a liquid droplet as in the vapor-liquid-solid (VLS) process,[45,46] (iii) direction through the use of a template,[47,48] (iv) kinetic control provided by a capping reagent,[49] (v) self-assembly of 0D nanostructures,[50] and (vi) size reduction of a 1D microstructure.[51] The further development of fabrication methods is, however, required for practical routes. Similarly, some sophisticated methods for 3D nano-architectures have been reported using template method,[52,53] VLS method,[54] and electrospinning method.[55,56] The complexity of these fabrication processes are not appropriate to the practical applications. For example, the template methods need several steps including fabrication and removal of templates to obtain 3D nano-architectures. Hence, for the mass production of these nanomaterials, it is indispensable to establish a simple and inexpensive fabrication method.

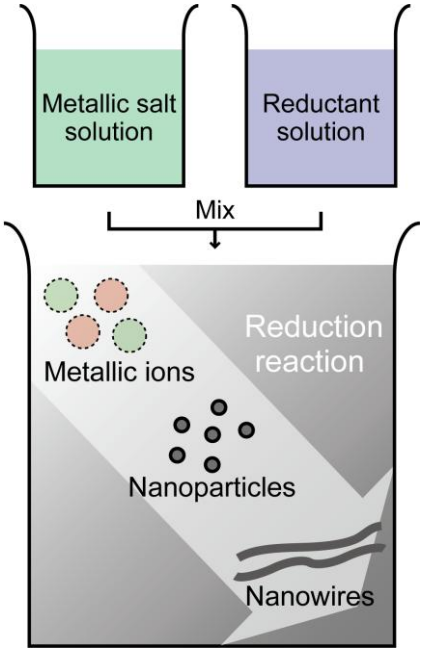

Figure 1.1 Schematic illustration of formation of metallic nanomaterials via electroless deposition.

In the present work, we focused on the electroless deposition using reducing agents, where metallic nanomaterials are formed by mixing two solutions containing metallic ions and reducing agents as schematically shown in Figure 1.1. The nucleation and growth of the particles proceed in the simultaneous reactions of oxidation of the reducing agents and reduction of metallic ions. Therefore, the formation of metallic nanoparticles via electroless deposition is an electrochemical process. The electroless deposition is one of the most promising methods because it is relatively simple method to fabricate nanoparticles with a wide variety of compositions and sizes in a large-scale. Thus, it is suitable for a practical application. Additionally, the nanoparticles of iron group metals and alloys can be aligned along an applied magnetic field due to their shape magnetic anisotropy. Thus, nanowires are formed by preparing nanoparticles under a magnetic field. This method for the formation of self-assemble nanowires under a magnetic field is a simple method without complex equipments and procedures.

Although 3D metallic nanostructures composed of nanowires (such as composites of metallic nanoparticles with polymer-nanowire-nonwoven cloths,[63] nanopillars on a substrate,[64] and carbon nanofibers encapsulating metallic nanoparticles[65]) are recently synthesized, they require composite compounds and/or templates to grow nanowires. On the other hand, a nanowire sheet is often prepared as a nonwoven cloth. For example, the nanowire-nonwoven cloths of various polymers and oxides have been prepared by the electro-spinning method.[59-62] In this study the author tried to fabricate metal-nanowire-nonwoven cloths (MNNCs) from metallic nanowires in a simple step. To our knowledge, there have been no reports about one-step fabrication methods of free-standing metal-nanowire-nonwoven cloths. If free-standing MNNCs are obtained by a simple and easy fabrication method, they will be applied to a lot of applications which cannot be achieved by existing nanomaterials (as discussed in the next section).

In the formation of metallic nanoparticles, nanowires, and nanowire-nonwoven cloths by electroless deposition, various factors (such as reaction temperature, concentration of metallic ions/reducing agents, and strength of magnetic fields) affect the morphology, composition ratio, and crystal structure of the products. Thus, the optimization of reaction solutions is necessary in order to control their formation, however, the reaction solutions have been optimized by a trial and error method. As a reason for this, there is little quantitive consideration of a formation process of nanoparticles and nanowires from the viewpoint of electrochemistry, while metallic nanomaterials are electrochemically formed. One major achievement of the present research is the establishment of electrochemical approaches to investigate the formation process of metallic nanomaterials via electroless deposition.

1.4 High-cyclability electrode based on metal-nanowire-nonwoven cloth for lithium ion batteries

A conventional composite electrode used in the present batteries is composed mainly of four components (active materials, binders, conductive additives, and current collectors) as shown in Figure 1.2a.[66] The conventional design of the composite electrode is suitable for mass production, which have brought an innovative breakthrough in the widespread use of the batteries. Especially, lithium ion batteries (LIBs) hold a key technology in the electrochemical energy storage for various portable electronic devices, since they possess high gravimetric and volumetric energy density compared to other batteries.[66-68] However, the further development of LIBs with high energy and high power densities is required for the future needs as hybrid electric vehicle (HEV) and EV.[66-71]

To improve the energy density of LIBs, negative electrode materials alternative to the present graphite electrode, such as silicon,[72,73] tin-based alloy,[74,75] and various oxide materials,[76-78] have been widely investigated. These materials exhibit a larger capacity than graphite, but the volume change accompanied by lithiation/delithiation processes is so large that the electrodes quickly deteriorate with an increase in cycles.[79,80] This deterioration process is schematically drawn in Fig. 1.2a. To circumvent the capacity fading due to pulverization, the use of nanoparticles as active materials was frequently discussed.[81] The nanoparticles shows the better cyclability and the enhancement of electrochemical reactions due to their large specific surface areas. However, the advantages of nanoparticles cannot be utilized efficiently in the composite electrode, because the aggregations of nanoparticles during a slurry dying process decrease the intrinsic surface areas of nanoparticles.[82] Additionally, the interspaces in the electrode would be insufficient to accommodate large volume expansion.[83] It is believed that loss of the electrical contact between active materials

and a current collector due to the large volume change is one of the causes of the capacity fading, and it is difficult to prevent the degradation of composite electrodes by using a conventional polyvinylidene fluoride (PVDF) binder.[84,85] Though several kinds of binders have been studied, they are not good enough to solve the problem.[86-88] Consequently, it is still a great issue to develop composite electrodes with high energy and high power densities.

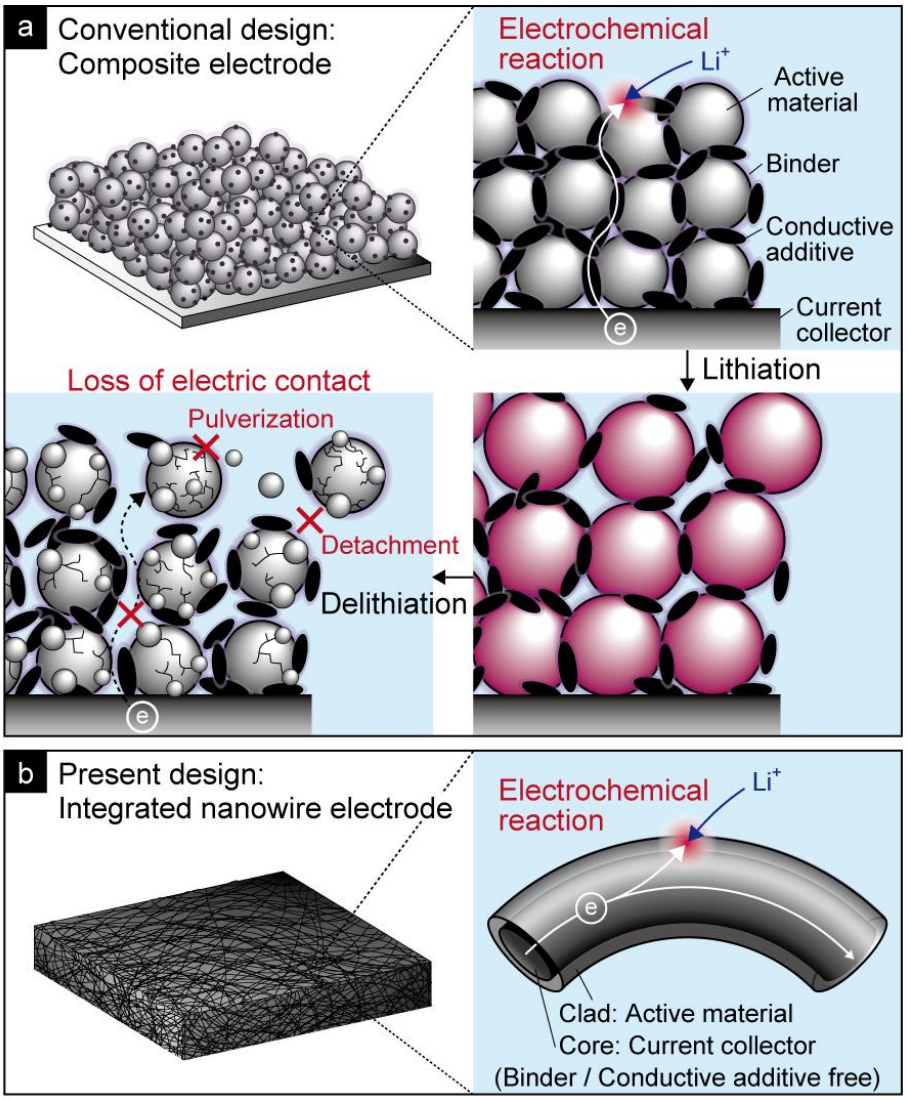

Figure 1.2 Schematic illustration of the electrode designs. (a) A conventional composite electrode which consists of the four components; active materials, binders, conductive additives, and current collectors. (b) An integrated nanowire electrode composed of three-dimensionally-tangled core-clad nanowires. The core and clad of the nanowires works as a current collector and an active material, respectively. This binder/conductive additive free electrode solely works as an electrode for LIBs.

Recently, several designs of electrode have been proposed, such as metal pillar arrays,[89,90] carbon networks,[91,92] inverse opal structures,[93] and mesoporous materials.[94] They consist of three-dimensional (3D) interconnected nano-architectures exhibiting an ideal electrode structure for battery systems, which provide efficient ion/electron transports as well as sufficient interspaces to accommodate large volume changes.[95] It is extensively demonstrated that these 3D nano-electrodes show high rate capabilities without a capacity fading due to their highly-controlled interspaces.[89-95] Thus, the use of 3D nano-structured electrode is a promising approach to realize excellent battery performances with high energy and high power densities.

In the present study, we propose an integrated-nanowire electrode based on MNNC as a new design of high-cyclability electrode. The electrode consists of three-dimensionally-tangled conductive metallic nanowires and active materials deposited or coated on them. The basic morphology is schematically shown in Fig. 1.2b. It is expected that large surface areas can provide efficient ion/electron transports as well as very short solid-state diffusion lengths, and sufficient interspaces can accommodate large volume changes, which is especially important in the negative electrode of LIBs. The advantages of the present metal-nanowire electrode will be verified by applying it to the negative electrode of LIBs.

1.5 Outline of this study

The outline of this study is explained in Figure 1.3. The present thesis is composed of two parts. Namely, the first fundamental part (chapters 2 to 6) describes electrochemical analysis in formation of iron group nanomaterials via electroless deposition, and the second part (chapter 7) deals with applications of iron group nanomaterials to electrodes of LIBs.

In chapter 2, we propose the electrochemical in-situ measurements (such as a mixed potential measurement and a quartz crystal microbalance measurement) as novel monitoring methods for formation of metallic nanoparticles by electroless deposition. The electrochemical in-situ measurements are applied to the formation process of cobalt nanoparticles in aqueous solution, where the electrochemical consideration is relatively easy because the thermodynamic data of various chemical species have been already published. The reduction ability in reaction solution is evaluated by comparing an experimental mixed potential and a redox potential of metal thermodynamically calculated.

In chapter 3, the electrochemical in-situ measurements are expanded to the formation process of cobalt nanoparticles in nonaqueous solution, where the thermodynamic consideration is difficult because of the lack of thermodynamic data. The electrochemical quartz crystal microbalance (EQCM) method combined with the electrochemical in-situ measurements enables us to evaluate the reduction ability even in nonaqueous solution.

In chapter 4, the effect of a magnetic field on formation of nickel nanoparticles and nanowires is investigated by using the electrochemical analyses which are discussed in chapter 2 and 3. Based on the results of the electrochemical in-situ measurements, we propose a formation mechanism of metallic nanowires and a method to control their morphology.

In chapter 5 and 6, we investigate the alloying effect on the formation of metallic nanoparticles and nanowires in Co-Ni and Fe-Co systems. The electrochemical measurements revealed that the catalytic activities of these metals strongly affect the morphology, composition ratio, and crystal structure of the metallic nanomaterials. We experimentally demonstrated that the formation of metallic nanomaterials via electroless deposition results in the electrode reaction of metals, which is the key to design the metallic

nanomaterials.

Chapter 7 deals with the application of the iron group metallic nanomaterials. We propose a new design of high-cyclability integrated-nanowire electrode, in which active materials are deposited or coated on MNNC. To demonstrate the advantages over the conventional composite electrode, as a prototype, we fabricate a NiO-covered nickel-nanowire-nonwoven cloth (NNNC) and evaluate its electrochemical performance.

Chapter 8 is the summary of each chapter.

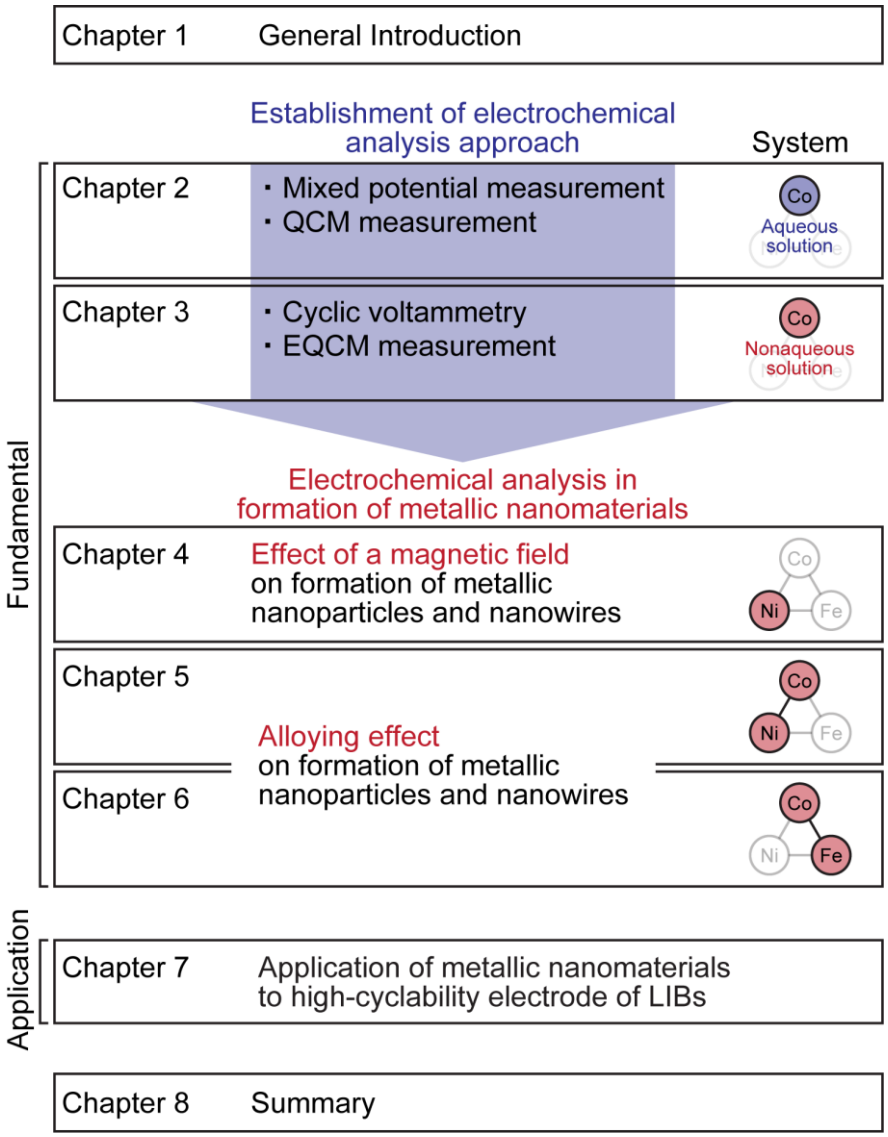

Figure 1.3 Outline of the present study.

References

1. A.-H. Lu, E. L. Salabas, and F. Schüth, *Angew. Chem. Int. Ed.*, **46**, 1222 (2007).
2. S. Laurent, D. Forge, M. Port, A. Roch, C. Robic, L. V. Elst, and R. N. Muller, *Chem. Rev.*, **108**, 2064 (2008).
3. X. Chen and S. S. Mao, *Chem. Rev.*, **107**, 2891 (2007).
4. A. N. Shipway, E. Katz, and I. Willner, *CHEMPHYSCHEM*, **1**, 18 (2000).
5. M.-C. Daniel and D. Astruc, *Chem. Rev.*, **104**, 293 (2004).
6. H. Sugimura, S. Nanjo, H. Sano, and K. Murase, *J. Phys. Chem.*, **113**, 11643 (2009).
7. D. Astruc, F. Lu, and J. R. Aranzaes, *Angew. Chem. Int. Ed.*, **44**, 7852 (2005).
8. B. Lim, M. Jiang, P. H. C. Camargo, E. C. Cho, J. Tao, X. Lu, Y. Zhu, and Y. Xia, *Science*, **324**, 1302 (2009).
9. S. Sun, C. B. Murray, D. Weller, L. Folks, A. Moser, *Science*, **287**, 1989 (2000).
10. D. Alloyeau, C. Ricolleau, C. Mottet, T. Oikawa, C. Langlois, Y. Le Bouar, N. Braidy, and A. Loiseau, *Nature Mater.*, **8**, 940 (2009).
11. A. Alam, B. Kraczek, and D. D. Johnson, *Phys. Rev. B*, **82**, 024435 (2010).
12. V. Tzitzios, G. Basina, D. Niarchos, W. Li, and G. Hadjipanayis, *J. Appl. Phys.*, **109**, 07A313 (2011).
13. H. Bönnemann, R. A. Brand, W. Brijoux, H.-W. Hofstadt, M. Frerichs, V. Kempter, W. M.-Friedrichs, N. Matoussevitch, K. S. Nagabhushana, F. Voigts, and V. Caps, *Appl. Organometal. Chem.*, **19**, 790 (2005).
14. W.S. Seo, J.H. Lee, X. Sun, Y. Suzuki, D. Mann, Z. Liu, M. Terashima, P. C. Yang, M. V. Mcconnell, D. G. Nishimura, and H. Dai, *Nature Mater.*, **5**, 971 (2006).
15. Q. A. Pankhurst, J. Connolly, S. K. Jones, and J. Dobson, *J. Phys. D: Appl. Phys.*, **36**, R167 (2003).

16. Y. Shirakata, N. Hidaka, M. Ishitsuka, A. Teramoto, and T. Ohmi, *IEEE Trans. Magn.*, **44**, 2100 (2008).

17. W.-H. Chiang and R. M. Sankaran, *Nature Mater.*, **8**, 882 (2009).

18. S. K. Singh, X.-B. Zhang, and Q. Xu, *J. Am. Chem. Soc.*, **131**, 9894 (2009).

19. K. Asazawa, K. Yamada, H. Tanaka, A. Oka, M. Taniguchi, and T. Kobayashi, *Angew. Chem. Int. Ed.*, **46**, 8024 (2007).

20. Önder Metin, V. Mazumder, S. Özkar, and S. Sun, *J. Am. Chem. Soc.*, **132**, 1468 (2010).

21. S. Sharma, A. Barman, M. Sharma, L. R. Shelford, V. V. Kruglyak, and R. J. Hicken, *Solid State Communications*, **149**, 1650 (2009).

22. J.-H. Lim, A. Rotaru, S.-G. Min, L. Malkinski, and J. B. Wiley, *J. Mater. Chem.*, **20**, 9246 (2010).

23. A. J. Yin, J. Li, W. Jian, A. J. Bennett, and J. M. Xu, *Appl. Phys. Lett.*, **79**, 1039 (2001).

24. A. Lonjon, L. Laffont, P. Demont, E. Dantras, and C. Lacabanne, *J. Phys. Chem*, **113**, 12002 (2009).

25. T. Nagai, N. Aoki, Y. Ochiai, and K. Hoshino, *ACS Appl. Mater. Interfaces*, **3**, 2341 (2011).

26. M.-H. Park, M. G. Kim, J. Joo, K. Kim, J. Kim, S. Ahn, Y. Cui, and J. Cho, *Nano Lett.*, **9**, 3844 (2009).

27. H. Guan, X. Wang, S. Chen, Y. Bandob, and D. Golberg, *Chem. Commun.*, **47**, 12098 (2011).

28. H. Zhang and P. V. Braun, *Nano Lett.*, **12**, 2778 (2012).

29. H. Kim, B. Han, J. Choo, and J. Cho, *Angew. Chem. Int. Ed.*, **47**, 10151 (2008).

30. X. Xin, X. Zhou, F. Wang, X. Yao, X. Xu, Y. Zhu, and Z. Liu, *J. Mater. Chem.*, **22**, 7724 (2012).

31. X. Li and S. Takahashi, *J. Magn. Magn. Mater.*, **214**, 195 (2000).

32. K. A. Tarasov, V. P. Isupov, B. B. Bakhonov, Y. A. Gapnov, B. P. Tolochko, M. M. Yulikov, A. Davidson, P. Beaunier, E. Marceau, and M. Che, *Microporous Mesoporous Mater.*, **107**, 202 (2008).

33. J. H. Kim and C. S. Yoon, *Thin Solid Films*, **516**, 4845 (2008).

34. R. Brayner, M.-J. Vaulay, F. Fiévet, and T. Coradin, *Chem. Mater.*, **19**, 1190 (2007).

35. G. Mattei, C. de Julián Fernández, P. Mazzoldi, C. Sada, G. De, G. Battaglin, C. Sangregorio, and D. Gatteschi, *Chem. Mater.*, **14**, 3440 (2002).

36. C. de Julián Fernández, C. Sangregorio, C. Innocenti, G. Mattei, and P. Mazzoldi, *Inorg. Chim. Acta*, **361**, 4138 (2008).

37. V. F. Meshcheryakov, Y. K. Fetisov, A. A. Stashkevich, and G. Viau, *J. Appl. Phys.*, **104**, 063910 (2008).

38. Y. M. Lee, C. W. Park, H. K. Choi, B. H. Koo, and C. G. Lee, *Met. Mater. Int.*, **14**, 117 (2008).

39. S. H. Naik, K. J. Carroll, and E. E. Carpenter, *J. Appl. Phys.*, **109**, 07B519 (2011).

40. J. Eastoe, S. Stebbing, J. Dalton, R. K. Heenan, *Colloids and Surfaces A*, **119**, 123 (1996).

41. J. Vargas, C. Ramos, R. D. Zysler, and H. Romero, *Physica B*, **320**, 178 (2002).

42. Y. Li, C. Zhu, and C. Wang, *J. Phys. D*, **41**, 125303 (2008).

43. Y. Xia, P. Yang, Y. Sun, Y. Wu, B. Mayers, B. Gates, Y. Yin, F. Kim, and H. Yan, *Adv. Mater.*, **15**, 353 (2003).

44. J. Stejny, R. W. Trinder, and J. Dlugosz, *J. Mater. Sci.*, **16**, 3161 (1981).

45. R. S. Wagner and W. C. Ellis, *Appl. Phys. Lett.*, **4**, 89 (1964).

46. B. Tian, X. Zheng, T. J. Kempa, Y. Fang, N. Yu, G. Yu, J. Huang, and C. M. Lieber, *Nature*, **449**, 885 (2007).

47. Y. Li, X. Li, Z.-X. Deng, B. Zhou, S. Fan, J. Wang, and X. Sun, *Angew. Chem. Int. Ed.*, **41**, 333 (2002).

48. T. Thurn-Albrecht, J. Schotter, G. A. Kästle, N. Emley, T. Shibauchi, L. Krusin-Elbaum, K. Guarini, C. T. Black, M. T. Tuominen, and T. P. Russell, *Science*, **290**, 2126 (2000).

49. B. Messer, J. H. Song, M. Huang, Y. Wu, F. Kim, and P. Yang, *Adv. Mater.*, **12**, 1526 (2000).

50. B. A. Korgel and D. Fitzmaurice, *Adv. Mater.*, **10**, 661 (1998).

51. G. F. Taylor, *Phys. Rev.*, **23**, 655 (1924).

52. S.-W. Woo, N. Okada, M. Kotobuki, K. Sasajima, H. Munakata, K. Kajihara, K. Kanamura, *Electrochim. Acta*, **55**, 8030 (2010).

53. T. A. Schaedler, A. J. Jacobsen, A. Torrents, A. E. Sorensen, J. Lian, J. R. Greer, L. Valdevit, W. B. Carter, *Science*, **334**, 962 (2011).

54. H. Peng, S. Meister, C. K. Chan, X. F. Zhang, and Y. Cui, *Nano Lett.*, **7**, 199 (2007).

55. M. Graeser, M. Bognitzki, W. Massa, C. Pietzonka, A. Greiner, and J. H. Wendorff, *Adv. Mater.*, **19**, 4244 (2007).

56. D. Li and Y. Xia, *Adv. Mater.*, **16**, 1151 (2004).

57. C. Petit, J. Legrand, V. Russier, and M. P. Pileni, *J. Appl. Phys.*, **91**, 1502 (2002).

58. M. Grzelczak, J. Pérez-Juste, B. Rodríguez-González, M. Spasova, I. Barsukov, M. Farle, and L. M. Liz-Marzán, *Chem. Mater.*, **20**, 5399 (2008).

59. A. Greiner and J. H. Wendorff, *Angew. Chem. Int. Ed.*, **46**, 5670 (2007).

60. J. Hu and S. Chen, *J. Mater. Chem.*, **20**, 3346 (2010).

61. D. Li and Y. Xia, *Nano Lett.*, **3**, 555 (2003).

62. W. E. Teo and S Ramakrishna, *Nanotechnology*, **17**, R89 (2006).

63. S. Yagi, T. Nakagawa, E. Matsubara, S. Matsubara, S. Ogawa, and H. Tani, *Solid-State Lett.*, **11**, E25 (2008).

64. F.-F. Cao, J.-W. Deng, S. Xin, H.-X. Ji, O. G. Schmidt, L.-J. Wan, and Y.-G. Guo, *Adv. Mater.*, **23**, 4415 (2011).

65. Y. Yu, L. Gu, C. Wang, A. Dhanabalan, P. A. van Aken, and J. Maier, *Angew. Chem. Int. Ed.*, **48**, 6485 (2009).

66. J.-M. Tarascon and M. Armand, *Nature*, **414**, 359 (2001).

67. M. Armand and J.-M. Tarascon, *Nature*, **451**, 652 (2008).

68. P. G. Bruce, B. Scrosati, and J.-M. Tarascon, *Angew. Chem. Int. Ed.*, **47**, 2930 (2008).

69. B. Kang and G. Ceder, *Nature*, **458**, 190 (2009).

70. C. K. Chan, H. Peng, G. Liu, K. Mcilwrath, X. F. Zhang, R. A. Huggins, and Y. Cui, *Nat. Nanotechnol.*, **3**, 31 (2008).

71. S. W. Lee, N. Yabuuchi, B. M. Gallant, S. Chen, B.-S. Kim, P. T. Hammond, and Y. Shao-Horn, *Nat. Nanotechnol.*, **5**, 531 (2010).

72. A. Magasinski, P. Dixon, B. Hertzberg, A. Kvit, J. Ayala, and G. Yushin, *Nature Mater.*, **9**, 353 (2010).

73. W. Wang and P. N. Kumta, *ACS Nano*, **4**, 2233 (2010).

74. G. Wang, B. Wang, X. Wang, J. Park, S. Dou, H. Ahn, and K. Kim, *J. Mater. Chem.*, **19**, 8378 (2009).

75. L. Bazin, S. Mitra, P. L. Taberna, P. Poizot, M. Gressier, M. J. Menu, A. Barnabé, P. Simon, J.-M. Tarascon, *J. Power Sources*, **188**, 578 (2009).

76. Y. Li, B. Tan, and Y. Wu, *Nano Lett.*, **8**, 265 (2008).

77. J. Chen, L. Xu, W. Li, and X. Gou, *Adv. Mater.*, **17**, 582 (2005).

78. H. Wu, M. Xu, H. Wu, J. Xu, Y. Wang, Z. P. and G. Zheng, *J. Mater. Chem.*, **22**, 19821

(2012).

79. T. Ichitsubo, S. Yukitani, K. Hirai, S. Yagi, T. Uda, and E. Matsubara, *J. Mater. Chem.*, **21**, 2701 (2011).
80. M. Winter and J. O. Besenhard, *Electrochim. Acta*, **45**, 31 (1999).
81. D.-H. Ha, M. A. Islam, and R. D. Robinson, *Nano Lett.*, **12**, 5122 (2012).
82. Y. Wang, J. Y. Lee, and B.-H. Chen, *Solid-State Lett.*, **6**, A19 (2003).
83. N. Liu, H. Wu, M. T. McDowell, Y. Yao, C. Wang, and Y. Cui, *Nano Lett.*, **12**, 3315 (2012).
84. W.-R. Liu, M.-H. Yang, H.-C. Wu, S. M. Chiao, and N.-L. Wu, *Solid-State Lett.*, **8**, A100 (2005).
85. S. Komaba, K. Shimomura, N. Yabuuchi, T. Ozeki, H. Yui, and K. Konno, *J. Phys. Chem. C*, **115**, 13487 (2011).
86. J. Li, D.-B. Le, P. P. Ferguson, and J.R. Dahn, *Electrochim. Acta*, **55**, 2991 (2010).
87. I. Kovalenko, B. Zdyrko, A. Magasinski, B. Hertzberg, Z. Milicev, R. Burtovyy, I. Luzinov, and G. Yushin, *Science*, **334**, 75 (2011).
88. G. Liu, S. Xun, N. Vukmirovic, X. Song, P. Olalde-Velasco, H. Zheng, V. S. Battaglia, L. Wang, and W. Yang, *Adv. Mater.*, **23**, 4679 (2011).
89. P. L. Taberna, S. Mitra, P. Poizot, P. Simon, and J.-M. Tarascon, *Nature Mater.*, **5**, 567 (2006).
90. J. Hassoun, S. Panero, P. Simon, P. L. Taberna, and B. Scrosati, *Adv. Mater.*, **19**, 1632 (2007).
91. H. Ji, L. Zhang, M. T. Pettes, H. Li, S. Chen, L. Shi, R. Piner, and R. S. Ruo, *Nano Lett.*, **12**, 2446 (2012).
92. B. Liu, J. Zhang, W. Xianfu, G. Chen, D. Chen, C. Zhou, and G. Shen, *Nano Lett.*, **12**,

3005 (2012).

93. H. Zhang, X. Yu, and P. V. Braun, *Nat. Nanotechnol.*, **6**, 277 (2011).

94. Y. Shi, B. Guo, S. A. Corr, Q. Shi, Y.-S. Hu, K. R. Heier, L. Chen, R. Seshadri, and G. D. Stucky, *Nano Lett.*, **9**, 4215 (2009).

95. J. W. Long, B. Dunn, D. R. Rolison, and H. S. White, *Chem. Rev.*, **104**, 4463 (2004).

Chapter 2

Application of Electrochemical In-situ Measurements for Formation of Cobalt Nanoparticles in Aqueous Solution

2.1 Introduction

As discussed in the previous chapter, the electroless deposition is suitable for practical applications among many methods for syntheses of metallic nanoparticles.[1-3] However, the designing of nanomaterials is existential and the preparation conditions of nanomaterials have been often optimized after a repeated trial and error. There has been little discussion on the formation process of nanoparticles from the viewpoint of thermodynamics, specifically electrochemistry. For the quantitative assessment of the reaction system, it is important to monitor the reaction process by using the electrochemical in-situ measurements.

In this chapter, first, a general concept of the electrochemical in-situ measurements, that is the mixed potential measurement and the QCM measurement, will be described. Then, these methods are applied to the formation process of cobalt particles in aqueous solution to show the effectiveness of the electrochemical in-situ measurements. By comparing the mixed potential and the thermodynamically calculated potential-pH diagram, we evaluate the driving force of the cobalt deposition. Additionally, the deposition behavior of metal is estimated by using the quartz crystal microbalance (QCM) substrate as a working electrode.

For ease in analysis, a simple reaction solution is selected. As a reducing agent, we use hydrazine, by which almost pure metal can be obtained,[4] while the use of other reducing

agents (such as hypophosphite, borohydride, and alkylamine boranes) leads to P or B impurities in deposit.[5,6] The aqueous solution is adopted since there are a lot of thermodynamic data of chemical species, and the thermodynamic consideration for metal deposition in aqueous solution is relatively easier than that in nonaqueous solution.

2.2 Electrochemical in-situ measurement

2.2.1 Mixed potential measurement

In the electroless deposition, the formation of metal proceeds with the simultaneous reactions of the oxidation of a reducing agent and the reduction of metallic ions. Therefore, the metal shows a certain potential which is determined by a balance of the total of anodic currents $I_{a,total}$ and the total of cathodic currents $I_{c,total}$ without any current flow from the outside (Figure 2.1).[7-9] This is called the mixed potential. By comparing kinetically determined mixed potential and thermodynamically calculated potential-pH diagram, it is possible to estimate whether the electrochemical reactions proceed as anodic reactions or cathodic reactions.[8] Namely, the electrochemical reaction proceeds as an anodic reaction when its redox potential is lower than the mixed potential. On the contrary, the electrochemical reaction, whose redox potentials is higher than the mixed potential, proceeds as a cathodic reaction. In the electroless deposition of metal, the difference of the redox potential of metal and the mixed potential corresponds to a driving force of the metal deposition. The reduction reaction of metallic ions proceeds when the mixed potential is lower than the redox potential of metal. Therefore, a mixed potential is a good indicator of a reduction ability in the reaction solution, and it is important to evaluate a reduction ability for the control of size of particles as well as their product phase.

Obviously, it is almost impossible to directly measure the mixed potential of metallic

nanoparticles formed in the reaction solution, because it is not practical to connect the potentiostat with each particle. Thus, we indirectly evaluate the mixed potential of the metallic particles by measuring a mixed potential of metal immerged in the reaction solution as a working electrode.

2.2.2 QCM measurement

In general, it is difficult to obtain the kinetic information on the deposition behavior of metallic nanoparticles synthesized by electroless deposition. In the present work, the formation of metallic nanomaterials is investigated by an in-situ QCM measurement in conjunction with the mixed potential measurement. Figure 2.2 shows the schematic of the QCM measurement and the photos of QCM substrate before and after the reaction. When metallic nanoparticles form in the reaction solution, the same metal simultaneously deposits on the QCM substrate by the electroless plating. A weight of the metal deposited on the QCM electrode, Δm, is calculated from the change in a resonance frequency of the QCM electrode, Δf, by Sauerbrey's equation[10];

$$\Delta m = -\frac{A\sqrt{\rho_q \mu_q}}{2 f_0^{\,2}} \Delta f \quad , \qquad [2.1]$$

where f_0 is the frequency of the QCM electrode before the deposition, A the active area of the QCM electrode (0.196 cm^2), ρ_q the density of quartz (2.648 g cm^{-3}), and μ_q the shear modulus of quartz (2.947 x 10^{11} g cm^{-1} s^{-2}). The in-situ QCM measurement enables us to evaluate kinetic information on the deposition behaviors of metal, such as a deposition rate, a start point, and a terminal point of the deposition reaction.

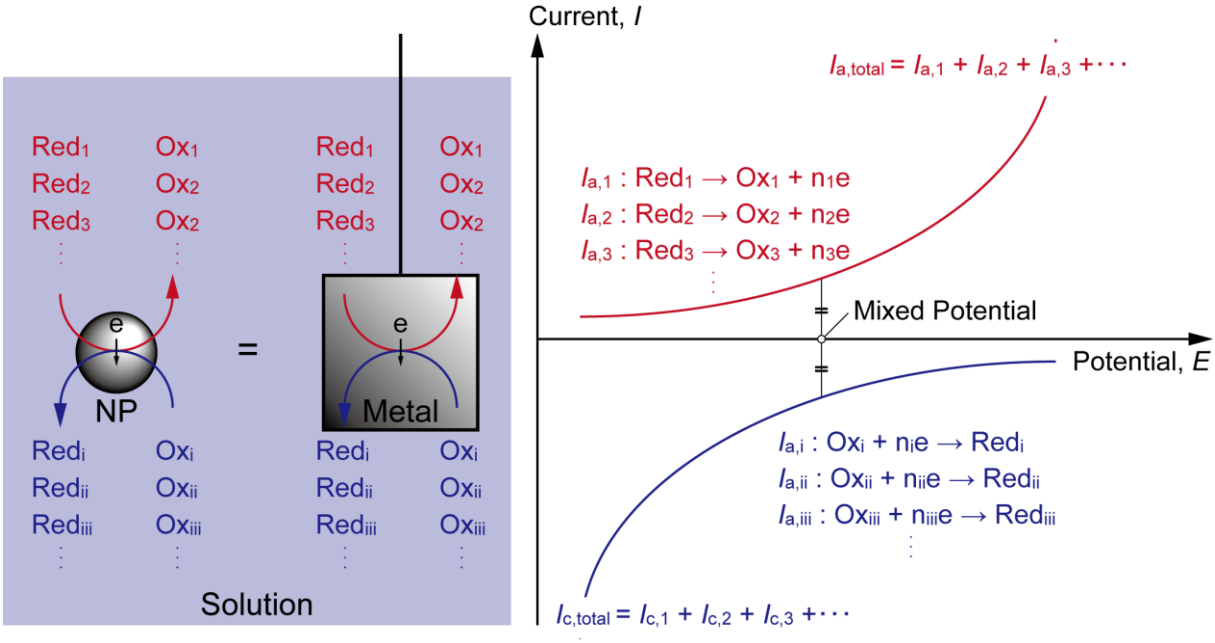

Figure 2.1 Schematic illustration of potential-current curves. Mixed potential is determined at the value where the total of anodic currents $I_{a,total}$ balances the total of cathodic currents $I_{c,total}$ unless current flows outside.

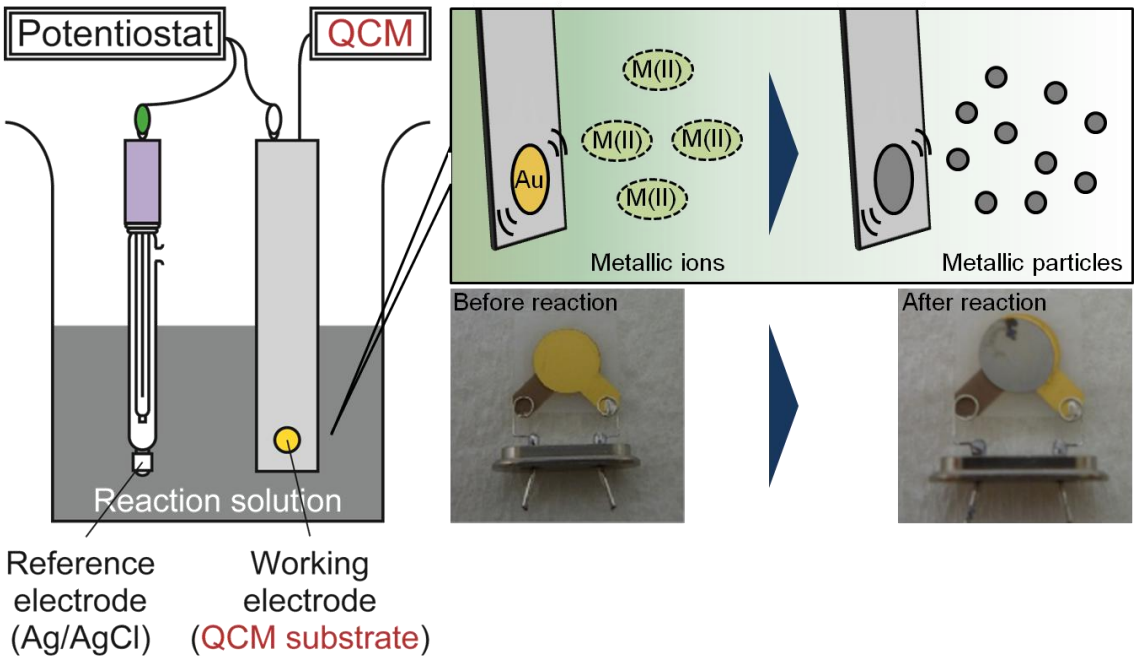

Figure 2.2 Schematic illustration of the mixed potential measurement and the in-situ QCM measurement. Photos of the QCM substrates before and after the reaction are also indicated.

2.3 Experimental

2.3.1 Synthesis method and characterization of cobalt particles

The reaction solutions were prepared using cobalt chloride hexahydrate ($CoCl_2 \cdot 6H_2O$) as a source of cobalt ions, hydrazine monohydrate ($N_2H_4 \cdot H_2O$) as a reducing agent, and sodium hydroxide (NaOH) for adjusting pH of the reaction solution. These reagents are all reagent-grade (Nacalai Tesque, Inc.) and used without further purification.

First, 54 cm^3 cobalt chloride solution containing 0.100 M $CoCl_2$ was prepared, where M corresponds to mol dm^{-3}. The pH of the solution was adjusted to 12.0 and 14.0 at 298 K by sodium hydroxide aqueous solution with a pH meter (Horiba D-54). Cobalt ions dissolved in the solution is almost all hydrolyzed to cobalt hydroxide. Next, the same amount of the aqueous solution containing 1.0 M N_2H_4 was also prepared. The pH of the hydrazine solution was adjusted to 12.0 and 14.0 at 298 K by a NaOH aqueous solution. The compositions of reaction solutions are summarized in Table 2.1. The temperature of the solutions was kept at 353 K with nitrogen gas bubbling to remove the dissolved oxygen. The metallic salt solution and the hydrazine solution were mixed at 353 K. After the mixing of the metallic salt solution and the hydrazine solution, the compositions of Co(II) and N_2H_4 are 0.050 M and 0.50 M, respectively. The reaction solution was agitated at a rate of 500 rpm with a magnetic stirring unit at 353 K during the reaction. After the reaction, the precipitates were separated from the solution by centrifugation and washed several times with ion-exchanged water and ethanol.

The crystalline structure of the precipitates was investigated by X-ray diffraction (XRD, MAC Science M03XHF22) using Mo *K*α radiation. The morphology of the precipitates was observed by a field-emission scanning electron microscope (JEOL Ltd., JSM-6500F).

Table 2.1 Compositions of the metallic salt solutions and the hydrazine solutions for the synthesis of cobalt particles.

	Compositions of metallic salt solutions		Compositions of hydrazine solutions	
	$[CoCl_2]$ / M	pH	$[N_2H_4]$ / M	pH
(a)	0.100	12.0	1.00	12.0
(b)	0.100	14.0	1.00	14.0

2.3.2 In-situ electrochemical measurements of cobalt deposition

During the synthesis of cobalt particles, the rate of cobalt deposition was evaluated in situ QCM measurement using round 9 MHz AT-cut quartz crystal substrates (QCM substrates), on both sides of which Au layers with a 5.0 mm diameter were sputtered with an underlying Ti buffer layer. The Au-plated QCM substrate was fixed inside a dipping-type Teflon holder (Seiko EG&G QCA917-21) with a circular window so that one surface of the substrate was exposed to deposition solutions through the window while the other surface was isolated from the solutions; the electrochemically active area of the QCM substrate on one side was thus 0.196 cm^2. The holder with an oscillating circuit was connected to a frequency counter (Seiko EG&G QCA917) with a coaxial cable.

The mixed potential on the QCM electrode was measured by a potentiostat/galvanostat (Hokuto Denko Co., Ltd., HA-151) using a Ag/AgCl (3.33 M KCl) electrode (Horiba, 2565A-10T) as a reference electrode. Internal liquid of the reference electrode was separated into two rooms by porous ceramics. The internal room involving a Ag/AgCl electrode was always filled with 3.33 mol dm^{-3} KCl aqueous solution saturated with AgCl. The external room was filled with 3.33 mol dm^{-3} KCl aqueous solution. In this work, discussion proceeds on the basis that the effect of the liquid junction potential difference is small enough to be ignored.

2.4 Results

In the present method, pH of the reaction suspension was initially adjusted at 298 K, and actual pH at reaction temperatures was different from the adjusted value, which is ascribable to the change in the ionic product for water. pH decreases with increasing temperature, and the value of the reaction solutions becomes 10.8 and 11.9, which is initially adjusted to 12.0 and 14.0 at 298 K, respectively.

Figure 2.3 shows the XRD patterns of precipitates obtained just after mixing the solutions containing Co(II) and hydrazine and after the 1 and 2 hour reactions. In both cases, the cobalt ions dissolved in the metallic salt solutions were almost hydrolyzed to cobalt hydroxide before adding the hydrazine solution. The peaks of $Co(OH)_2$ are observed in the XRD patterns of the precipitates obtained in the solution of pH 10.8 at each reaction time. At pH 11.9, the hexagonal closepacked (hcp) peaks and the face-centered cubic (fcc) peaks of cobalt are observed after the 1 hour reaction.

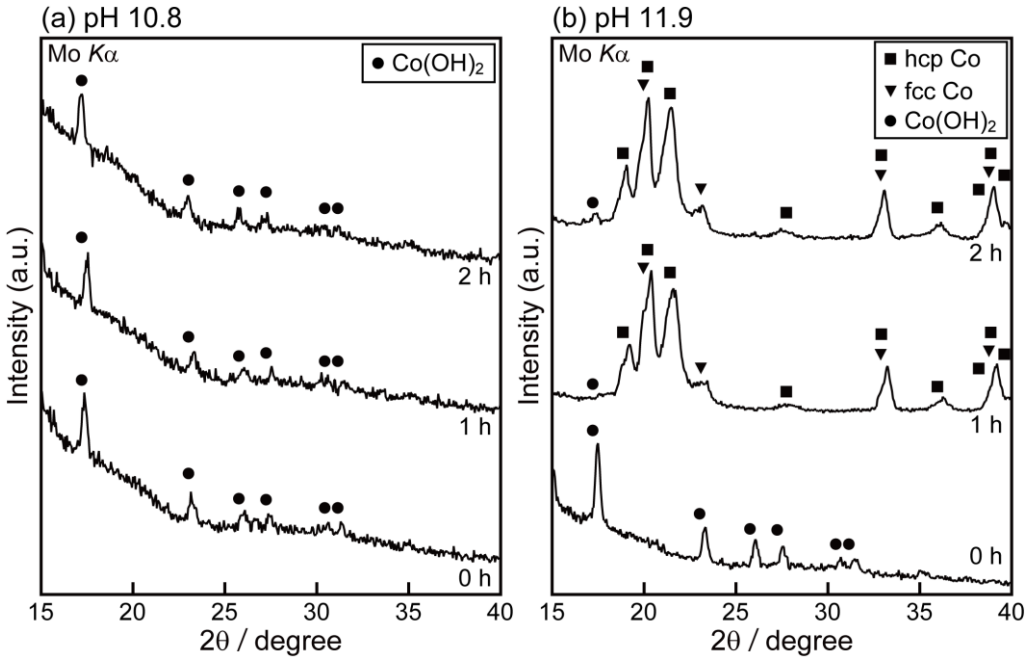

Figure 2.3 XRD patterns of the precipitates synthesized at 353 K from the solutions containing 0.050 M Co(II) and 0.500 M N_2H_4 at pH (a) 10.8 and (b) 11.9.

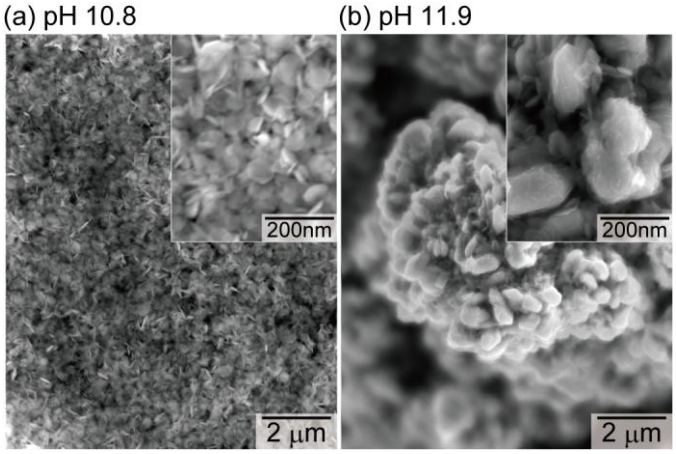

Figure 2.4 SEM images of the precipitates synthesized at 353 K from the solutions containing 0.050 M Co(II) and 0.500 M N_2H_4 at pH (a) 10.8 and (b) 11.9 by the 2 hour reaction.

Figure 2.4 shows the SEM images of the precipitates obtained from the solutions at pH 10.8 and 11.9 after the 2 hour reaction. The $Co(OH)_2$ flakes about 100 nm are observed at pH 10.8. By contrast, the dendritic cobalt particles are obtained from the reaction solution at pH 11.9.

The weight change of cobalt deposited on the QCM substrate is shown in Figure 2.5. At pH 11.9, the cobalt deposition on the QCM substrate is observed after mixing the solutions containing Co(II) and hydrazine. The weight of cobalt increases with time and reaches about 72 μg in 19 minutes, which is the maximum value observable in the present system. At pH 10.7, the cobalt deposition is hardly observed on the QCM substrate.

Consequently, pH of the reaction solution strongly affects the formation of cobalt; the cobalt deposition is not observed at pH 10.7 but at pH 11.9. In the next section, the effect of pH on the formation of cobalt is discussed by comparison of the mixed potential and the thermodynamically drawn potential-pH diagram.

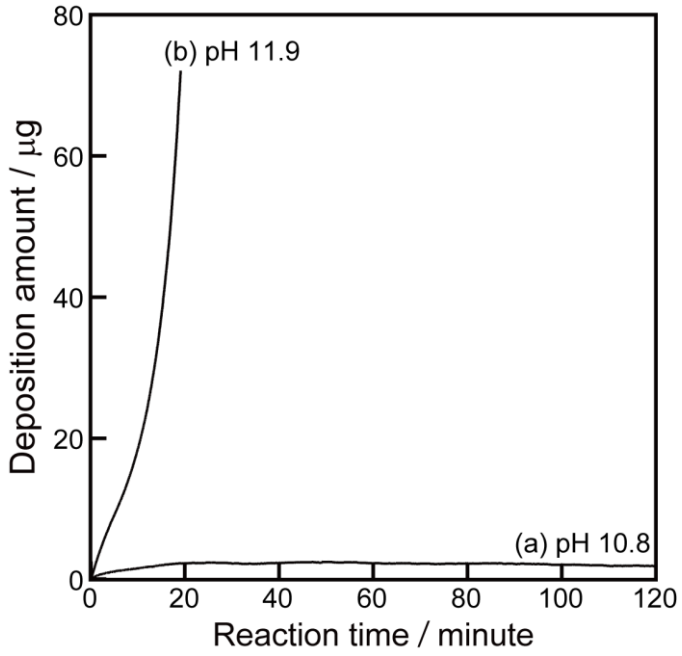

Figure 2.5 Weight change of metal deposited on the gold-sputtered QCM substrate from the solutions containing 0.050 M Co(II) and 0.500 M N_2H_4 at pH (a) 10.8 and (b) 11.9.

2.5 Discussion

2.5.1 Thermodynamic calculation for potential-pH diagrams

The formation of cobalt by electroless deposition proceeds in the simultaneous oxidation reaction of a reducing agent and the reduction reaction of metallic ions. In the present process, the following hydrazine oxidation reaction mainly occurs as an anodic reaction[11];

$$N_2H_4 + 4OH^- \rightarrow N_2 + 4H_2O + 4e \quad [2.2]$$

Cathodic reactions are mainly the cobalt deposition reaction and hydrogen evolution reaction as follows;

$$Co(II) + 2e \rightarrow Co \quad [2.3]$$

$$2H_2O + 2e \rightarrow H_2 + 2OH^- \ , \quad [2.4]$$

where Co(II) represents all the Co(II) species, e.g., Co^{2+}, $Co(OH)_2$, $HCoO_2^-$ or $Co(OH)_3^-$, and

CoO_2^{2-} or $Co(OH)_4$.[12] The redox potential of these electrochemical reactions can be calculated by using the thermodynamic data.

When the Co^{2+} aquo ions are in equilibrium with $Co(OH)_2$ in the following equation, the change of Gibbs free energy is 0 at a temperature *T* and a pressure of 1 atm.

$$Co^{2+} + 2H_2O = Co(OH)_2 + 2H^+ \quad [2.5]$$

$$\Delta G_{[2.5]} = \mu^0_{T\,Co(OH)_2} + 2(\mu^0_{T\,H^+} + RT \ln a_{H^+}) - (\mu^0_{T\,Co^{2+}} + RT \ln a_{Co^{2+}}) - 2\mu^0_{T\,H_2O} = 0 \quad , [2.6]$$

where ΔG is the change in Gibbs free energy of the reaction, μ^0 is the standard chemical potential of a chemical species, *R* is the gas constant, *T* is the temperature, and *a* is the activities of a chemical species. The standard chemical potentials of chemical species μ^0_T, are calculated using the standard heat of formation ΔH^0_{298}, standard entropy S^0_{298}, and specific heat at constant pressure C_p, namely,

$$\mu^0_T = \Delta H^0_{298} + \int_{298}^{T} C_p dT - T\left(S^T_{298} + \int_{298}^{T} \frac{C_p}{T} dT \right) \quad . \quad [2.7]$$

The activities of Co^{2+} aquo ions is calculated from the equations [2.6] and [2.7] by substituting the thermodynamic data in Table 2.2.[12-14] The activities of Co^{2+} aquo ions is expressed as function of pH,

$$a_{Co^{2+}} = 4.02 \times 10^{9-2pH} \quad . \quad [2.8]$$

Figure 2.6 shows the change of the activities of Co^{2+} aquo ions with respect to pH. The activity of Co^{2+} aquo ions exponentially decreases in an increase of pH. Using the experimentally measured pH in the solution, the activities of Co^{2+} in the aqueous solution can be obtained.

Table 2.2 List of standard heat of formation, entropy at 298 K and 1 atm, and specific heat at constant pressure (1 atm) considered and used for thermodynamic calculation.

Chemical speicies	Standard heat of formation $\Delta H^0_{298\,K}$ (kJ mol^{-1})	Standard entropy $S^0_{298\,K}$ (J K^{-1} mol^{-1})	Specific heat at constant pressure $C_p = a + b \times 10^{-3}\,T + c \times 10^5\,T^2$ (J K^{-1} mol^{-1})			References
			a	b	c	
H^+ (aq)	0.0	0.0	0.0	–	–	[12]
H_2 (g)	0.0	130.7	27.3	3.3	0.5	[13]
O_2 (g)	0.0	205.0	30.0	4.2	–1.7	[13]
H_2O (l)	−285.8	70.0	75.4	–	–	[13]
Co (s)	0.0	30.0	24.8	–	–	[12]
Co^{2+} (aq)	−57.6	−107.4	−32.6	–	–	[12]
$Co(OH)_2$ (s)	−540.8	96.0	97.1	–	–	[12]
N_2H_4 (l)	50.6	121.6	72.7	87.2	0.6	[14]
N_2 (g)	0.0	191.5	27.9	4.3	–	[13]

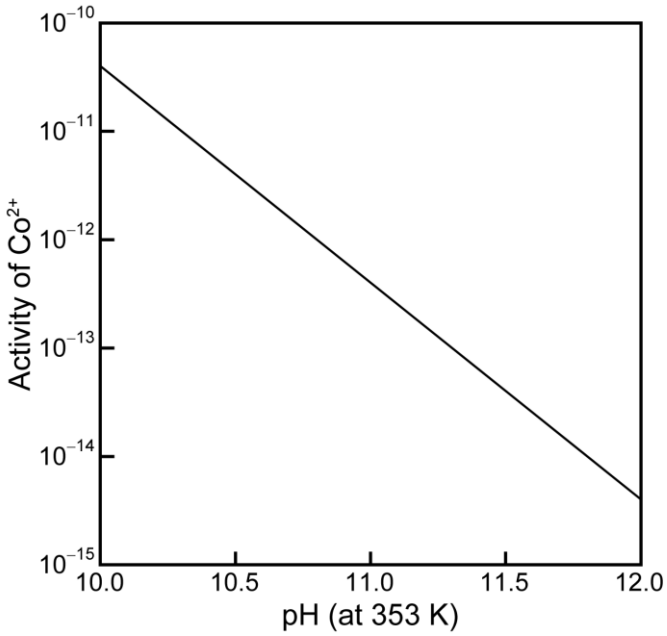

Figure 2.6 pH-dependence of the activity of Co^{2+} aquo ions calculated in Equation [2.8] from the thermodynamic data in Table 2.2.

When the Co^{2+} aquo ions are in equilibrium with cobalt metal, the equilibrium reaction is written as follows;

$$Co^{2+} + 2e = Co \qquad [2.9]$$

It is necessary to combine equation [2.9] with the redox reaction for the H^+/H^2 redox pair;

$$2H^+_{(SHE)} + 2e = H_{2(SHE)} \quad [2.10]$$

in order to determine the redox potential of Co^{2+}/Co redox pair with respect to standard hydrogen electrode (SHE). According to the Nernst equation, the redox potential of Co^{2+}/Co redox pair is calculated using the thermodynamic data (Table 2.2) as follows;

$$Co^{2+} + H_{2(SHE)} = Co + 2H^+_{(SHE)} \quad [2.11]$$

$$\begin{aligned}\Delta G &= \mu^0_{T\,Co} + 2(\mu^0_{T\,H^+(SHE)} + RT\ln a_{H^+(SHE)}) \\ &\quad -(\mu^0_{T\,Co^{2+}} + RT\ln a_{Co^{2+}}) - (\mu^0_{T\,H_{2(SHE)}} + RT\ln a_{H_{2(SHE)}}) \\ &= -2FE_{Co^{2+}/Co}\ ,\end{aligned} \quad [2.12]$$

where F is the Faraday constant (96485 C mol^{-1}), $a_{H^+(SHE)}$ and $a_{H_2(SHE)}$ are the activities of H^+ aquo ions and H_2 in SHE, whose values are 1. Similarly, the redox potential of N_2H_4 with respect SHE is calculated in the following reaction;

$$N_2 + 4H^+ + H_{2(SHE)} = N_2H_4 + 2H^+_{(SHE)} \quad [2.12]$$

$$\begin{aligned}\Delta G &= (\mu^0_{T\,N_2H_4} + RT\ln a_{N_2H_4}) + 2(\mu^0_{T\,H^+(SHE)} + RT\ln a_{H^+(SHE)}) \\ &\quad -(\mu^0_{T\,N_2} + RT\ln P_{N_2}) - 4(\mu^0_{T\,H^+} + RT\ln a_{H^+}) \\ &\quad -(\mu^0_{T\,H_{2(SHE)}} + RT\ln a_{H_{2(SHE)}}) \\ &= -4FE_{N_2/N_2H_4}\ ,\end{aligned} \quad [2.13]$$

where $a_{N_2H_4}$ is the activity of N_2H_4, which is set to be equal to the concentration of N_2H_4. The partial pressure of N_2, P_{N_2}, is assumed to 1 because N_2 gas flows during the reaction. The activity of Co(II) ions and the redox potentials of electrochemical reactions as discussed above are summarized in Table 2.3. Figure 2.7 shows the potential-pH diagram in the Co-H_2O and N_2H_4-H_2O systems. It is possible from the potential-pH diagram to know what chemical species is stable at a certain pH and potential.

Table 2.3 List of oxidation-reduction potentials calculated for partial reactions considered in this system. Activity of each chemical species is substituted by the actual molar concentration in the present reaction system, and specifically, activities of N_2 and H_2 are substituted by 1 and 10^{-6} to obtain reference values.

	Partial reaction	Oxidation-reduction potential / V vs. SHE
(a)	$Co^{2+} + 2e^- = Co$	$E = -0.279 + 0.035 \log a_{Co^{2+}}$
(b)	$Co(OH)_2 + 2H^+ + 2e^- = Co + 2H_2O$	$E = 0.057 - 0.070$ pH
(c)	$N_2 + 4H^+ + 4e^- = N_2H_4$	$E = -0.639 - 0.070$ pH
(d)	$2H_2O + 2e^- = H_2 + 2OH^-$	$E = 0.210 - 0.070$ pH

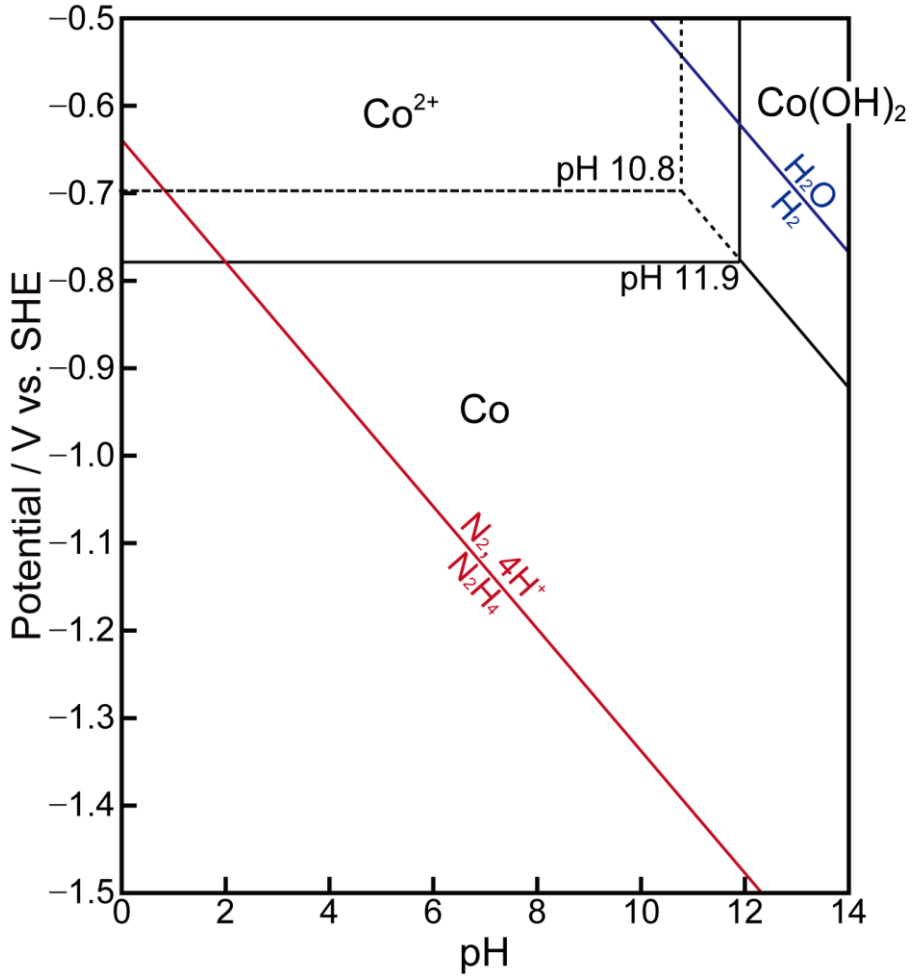

Figure 2.7 Potential–pH diagrams drawn at the equilibrium activities of Co^{2+} aquo ions at pH 10.8 and 11.9 at 353 K considering the chemical species of Co^{2+}, $Co(OH)_2$, Co, N_2, N_2H_4, H_2O, H^+, OH^-, and H_2. The partial pressures of N_2 and H_2 are set to 1 and 10^{-6}, respectively.

2.5.2 Comparison of mixed potential and potential-pH diagrams

Figure 2.8 shows the time-dependence of mixed potentials during the synthesis of cobalt particles in solutions of pH 10.8 and 11.9 at 353 K. The potential of the reference electrode could be expressed as a function of temperature and the following equation is used for the conversion of the mixed potential vs. Ag/AgCl electrode to vs. SHE electrode.

$$E_{\text{vs. Ag/AgCl}} = -206 + 0.7 \times (T(\text{K}) - 298) + E_{\text{vs.SHE}}\ (\text{mV})\ . \qquad [2.14]$$

The redox potentials of Co^{2+}/Co obtained from the potential-pH diagram (Fig. 2.7) are also indicated in Fig. 2.8. The mixed potential in the solution of pH 10.8 is always higher value than the redox potential of Co^{2+}/Co redox pair, indicating the cobalt deposition is thermodynamically impossible. It is estimated from the potential-pH diagram (Fig. 2.7) that $Co(OH)_2$ is stable in this condition, which is consistent with the result of XRD measurement as shown in Fig. 2.3a.

According to the potential-pH diagram as shown in Fig 2.7, the redox potential of N_2/N_2H_4 redox pair decreases in an increase of pH. This indicates that the reduction ability of hydrazine is higher at higher pH. Actually, the mixed potential at pH 11.9 is much lower than that at pH 10.8, which results from the higher reduction ability of hydrazine at a higher pH. At pH 11.9, the mixed potential drops below the redox potential of Co^{2+}/Co redox pair just after mixing the solutions containing Co(II) ions and hydrazine. Therefore, the cobalt deposition is thermodynamically possible in this condition. In fact, the deposition of cobalt metal is observed in the XRD profile (Fig. 2.3b) and the in-situ QCM measurement (Fig. 2.5b). It is noted that the mixed potential increases with time at about 60 minutes after the start of the reaction. Increase of potential with time can be mainly attributed to a consumption of hydrazine for the reduction of Co(II) and H_2O, because the mixed potential is mainly determined by a balance of an oxidation reaction of hydrazine and the reduction

reactions of Co(II) ions and H_2O.

In this way, the driving force of the metal deposition can be evaluated by comparing a mixed potential with a redox potential of metal. It is possible to predict stable chemical species from the mixed potential measurement, which is effectively used for optimization of a reaction system.

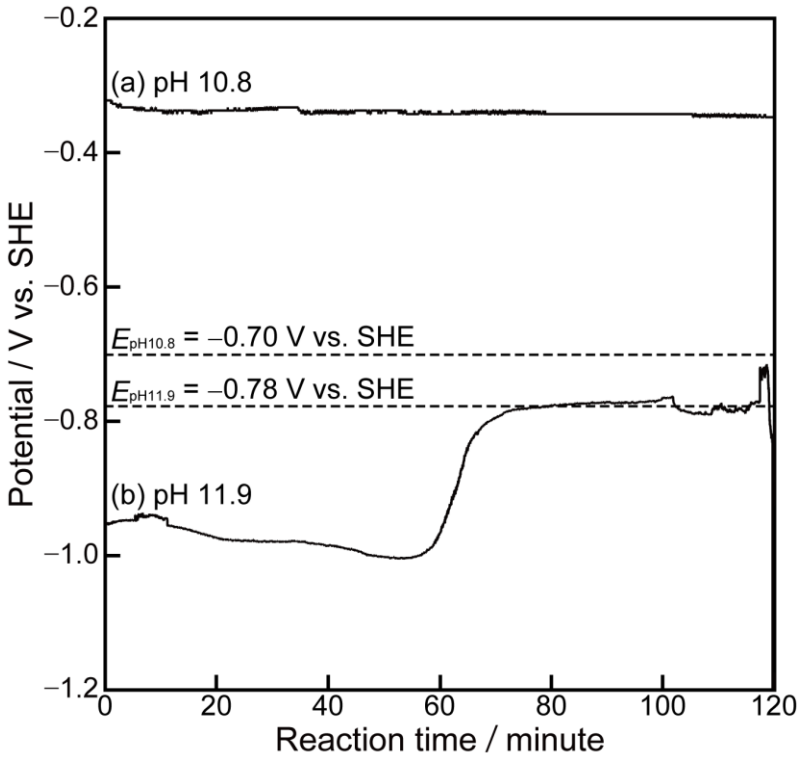

Figure 2.8 Time dependence of mixed potential in the solution containing 0.050 M Co(II), 0.50 N_2H_4 at pH (a) 10.8 and (b) 11.9. The redox potentials of Co^{2+}/Co redox pair are also indicated.

2.6 Conclusions

In this chapter, we described a general concept of the mixed potential measurement and the QCM measurement. These electrochemical in-situ measurements were applied to the formation of cobalt metal in the aqueous solution system. Through the present experiments, we have obtained the following results.

1. The formation of cobalt particles is strongly affected by pH of a solution; the cobalt deposition is more favorable at a higher pH.
2. The driving force of metal deposition is evaluated by comparing the mixed potential with the thermodynamically calculated redox potential of metal.
3. The cobalt deposition is observed in the aqueous solution of pH 11.9 at 353 K, where the mixed potential is lower than the redox potential of Co^{2+}/Co redox pairs

We have experimentally demonstrated that the mixed potential is the effective indicator of the reduction ability in the reaction solution, which is useful for prediction of chemical species of the product.

References

1. S. Ram, *Mater. Sci. Eng., A,* **304**, 923 (2001).
2. Y. Li, C. Zhu, and C. Wang, *J. Phys. D*, **41**, 125303 (2008).
3. S. Sun and C. B. Murray, *J. Appl. Phys.*, **85**, 4325 (1999).
4. S. S. Djkic, *J. Electrochem. Soc*., **144**, 2358 (1997).
5. J. Vargas, C. Ramos, R. D. Zysler, and H. Romero, *Physica B,* **320**, 178 (2002).
6. J. S. Judge, J. R. Morrison, D. E. Speliotis, and G. Bate, *J. Electrochem. Soc*., **112**, 681 (2008).

7. S. Yagi, H. Nakanishi, E. Matsubara, S. Matsubara, T. Ichitsubo, K. Hosoya, and Y. Matsuba, *J. Electrochem. Soc.*, **155**, D474 (2008).
8. S. Yagi, H. Nakanishi, T. Ichitsubo, and E. Matsubara, *J. Electrochem. Soc.*, **156**, D321 (2009).
9. M. D. L. Balela, S. Yagi, and E. Matsubara, *Electrochem. Solid-State Lett.*, **13**, D4 (2010).
10. A. Janshoff, H. J. Galla, and C. Steinem, *Angew. Chem. Int. Ed.*, **39**, 4004 (2000).
11. S. S. Djokic, *J. Electrochem. Soc.*, **144**, 2358 (1997).
12. J. Chivot, L. Mendoza, C. Mansour, T. Pauporté, and M. Cassir, *Corr. Sci.*, **50**, 62 (2008).
13. O. Kubaschewski, and C. B. Alcock, *Metallurgical Thermochemistry*, 5th ed. revised and enlarged, El sevier, New York (1979).
14. D. R. Stull, and H. Prophet, *JANAF Thermochemical Tables*, 2nd ed., NSRDS-NBS, Washington, DC (1971).

Chapter 3

Application of Electrochemical In-situ Measurements for Formation of Cobalt Nanoparticles in Nonaqueous Solution

3.1 Introduction

In the previous chapter, we applied the electrochemical in-situ measurements to fabrication of cobalt particles in aqueous solution. The driving force of metal deposition is evaluated by comparing the mixed potential with potential-pH diagrams (Pourbaix diagrams). This method is only effective for the metal deposition in aqueous solution, where there are many thermodynamic data of various chemical species for the thermodynamic calculations.

The nonaqueous solutions (e.g., ethylene glycol and propylene glycol) are often used as a solvent for syntheses of iron group nanoparticles by electroless deposition, for the following reasons; (i) The nonaqueous solutions have better compatibilities with organic surfactants which are used for the dispersive agents of the metallic nanoparticles.[1-6] (ii) The nonaqueous solutions usually have wider potential window than aqueous solutions, which results in the oxidation stability of metallic nanoparticles. (iii) The yield of metallic nanoparticles by electroless deposition in nonaqueous solutions is relatively high since the reductive decomposition of the nonaqueous solutions is unfavorable compared to the aqueous solutions. However, the thermodynamic calculation cannot be easily adopted to reaction systems using nonaqueous solutions because of the lack of thermodynamic data. Therefore, it is necessary to experimentally obtain a redox potential of metal by using a cyclic voltammetry. In order to obtain the redox potential of metal precisely, the reduction current of metal must be separately measured from the cathodic current because of the presence of a

decomposition of the solvent. Often, the latter current is dominant in a deposition of relatively-less noble metals, such as Fe, Co, Ni, etc. When a solvent decomposes during the cathodic reduction of a less noble metal, the reduction current of the metal is hardly measured from the total current by the usual voltammetry due to a large contribution of decomposition of the solvent. Therefore, in the present study, both a weight of deposited metal and a total current of the electrochemical reaction are simultaneously measured by the voltammetry combined with the QCM electrode, which is called an electrochemical QCM (EQCM) method.[7-9]

In this chapter, the formation process of cobalt nanoparticles in nonaqueous solution (ethylene glycol; EG) is electrochemically investigated. We experimentally determine the redox potential of the Co(II)/Co redox pair in EG by the EQCM method. The electrochemical analysis, which was applied to the formation of metal deposition in aqueous solution, is expanded to the analysis in formation of metallic nanoparticles in nonaqueous solution. The effect of a concentration of hydrazine on the formation of cobalt is investigated by comparison of the mixed potential and the redox potential of Co(II)/Co obtained by EQCM. Additionally, we investigate the effect of the nucleating agent on the deposition behavior of cobalt nanoparticles by the in-situ QCM measurement in conjunction with the mixed potential measurement.

3.2 Experimental

3.2.1 Synthesis method and characterization of cobalt nanoparticles

The reaction solutions were prepared using cobalt chloride hexahydrate ($CoCl_2 \cdot 6H_2O$) as a source of cobalt ions, ethylene glycol (EG) as a solvent, and hydrazine monohydrate ($N_2H_4 \cdot H_2O$) as a reducing agent. Sodium hydroxide (NaOH) was used as a

source of OH^- ions. Chloroplatinic acid hexahydrate ($H_2PtCl_6 \cdot 6H_2O$) were used as a nucleating agent. These reagents are all reagent-grade (Nacalai Tesque, Inc.) and used without further purification.

First, 27 cm^3 of EG solution containing 0.10 M $CoCl_2$, 1.4 M NaOH, and H_2PtCl_6 (0 - 10 mM) was prepared. Meanwhile, 27 cm^3 of EG solution containing N_2H_4 (5.0×10^{-3} - 1.0 M) and 0.6 M NaOH was prepared. The compositions of reaction solutions are summarized in Table 3.1. The temperature of the solutions was kept at a reaction temperature of 353 K on a hot plate with nitrogen gas bubbling to remove the dissolved oxygen. The metallic salt solution and the hydrazine solution were mixed at 353 K. The total amount of the reaction solution was 54 cm^3, and thus, the reaction solution contained 0.050 M $CoCl_2$ and 1.0 M NaOH. The reaction solution was agitated at a rate of 500 rpm with a magnetic stirring unit at 353 K during the reaction for the synthesis of cobalt particles.

The morphology of products was observed by a field-emission scanning electron microscope (JEOL Ltd., JSM-6500F). The mean diameter and size distribution of the cobalt particles were determined by an image analysis for randomly selected 300 particles. The crystalline structure of precipitates was investigated by XRD (Rigaku Co., Ltd., RINT-2200 and MAC Science M03XHF22) using Cr *K*α and Mo *K*α radiation.

Table 3.1 Compositions of the metallic salt solutions and the hydrazine solutions for the synthesis of cobalt particles in ethylene glycol.

	Compositions of metallic salt solutions			Compositions of hydrazine solutions	
	$[CoCl_2]$ (M)	[NaOH] (M)	$[H_2PtCl_6]$ (mM)	$[N_2H_4]$ (M)	[NaOH] (M)
(a)	0.100	1.4	–	5.0×10^{-3}	0.6
(b)	0.100	1.4	–	1.0×10^{-1}	0.6
(c)	0.100	1.4	–	1.0	0.6
(d)	0.100	1.4	0.5	1.0	0.6
(e)	0.100	1.4	2.0	1.0	0.6
(f)	0.100	1.4	10.0	1.0	0.6

3.2.2 Electrochemical in-situ measurement of cobalt deposition

During the syntheses of Co particles, the gold-sputtered QCM electrode (SEIKO EG&G QA-A9M-AU) was immersed in the reaction solution, and the mixed potential of the QCM electrode was measured by a potentiostat/galvanostat (Hokuto Denko Co., Ltd., HA-151) using a Ag/AgCl (3.33 M KCl) electrode (Horiba 2565A-10T) as a reference electrode. The weight of deposits on the QCM electrode was calculated from the change in resonance frequency of the QCM electrode by Sauerbrey's equation.

3.2.3 Measurement of the redox potential of Co(II)/Co redox pair by EQCM

The cyclic voltammogram was measured in 120 cm^3 of EG solution containing 0.050 M $CoCl_2$ and 1.0 M NaOH by the potentiostat/galvanostat using a gold-sputtered QCM electrode as a working electrode, a platinum electrode (20 x 20 mm) as a counter electrode, and a Ag/AgCl electrode as a reference electrode (Figure 3.1). During the measurement, the temperature of the solutions was kept at a reaction temperature of 353 K on a hot plate with nitrogen gas bubbling to remove the dissolved oxygen.

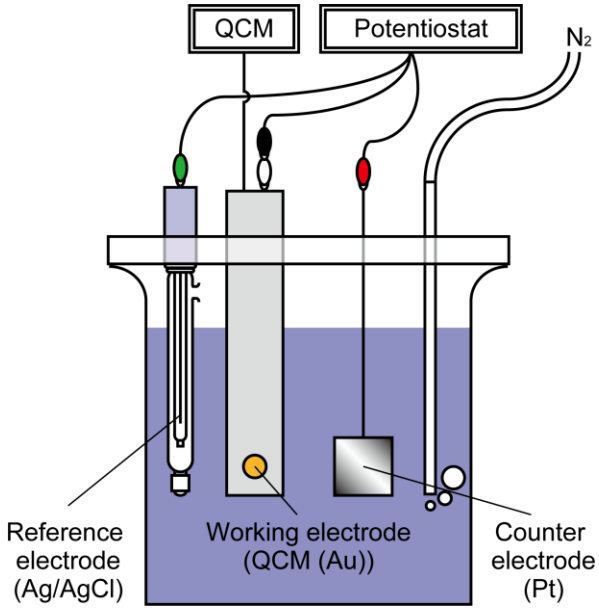

Figure 3.1 Schematic illustration of the set up for the cyclic voltammetry by the QCM electrode.

3.3 Effect of hydrazine concentration on formation of cobalt nanoparticles

3.3.1 Results

Figure 3.2 shows the XRD patterns of the specimens obtained from the solutions after the 2 hour reaction by changing the concentration of N_2H_4. In both cases, the cobalt ions dissolved in the metallic salt solutions were hydroxylated to form a green Co(II) hydroxide sol before adding the hydrazine solution. The hcp and fcc peaks of cobalt are observed in the XRD patterns of the precipitates obtained in the solution containing 0.50 M N_2H_4 (Fig. 3.2c). In contrast, the peaks of cobalt are not observed in the XRD patterns at 2.5 x 10^{-3} M and 5.0 x 10^{-2} M N_2H_4, indicating that the formation of cobalt particles does not occur in these condition.

Figure 3.3 shows the SEM images of cobalt particles obtained in the solution containing 0.50 M N_2H_4. The particles are almost spherical and the mean diameter of the particles is 930 nm.

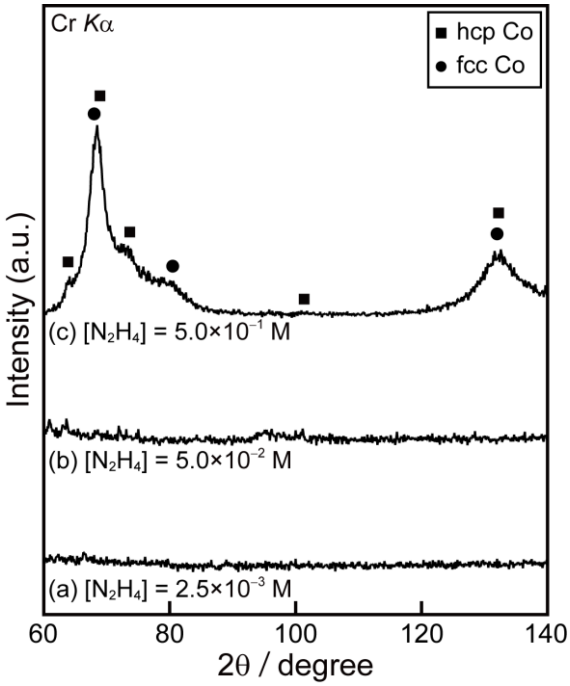

Figure 3.2 XRD patterns of the precipitates synthesized at 353 K from the solutions containing 0.050 M Co(II), (a) 2.5 x 10^{-3} M, (b) 5.0 x 10^{-2} M, and (c) 5.0 x 10^{-1} M N_2H_4.

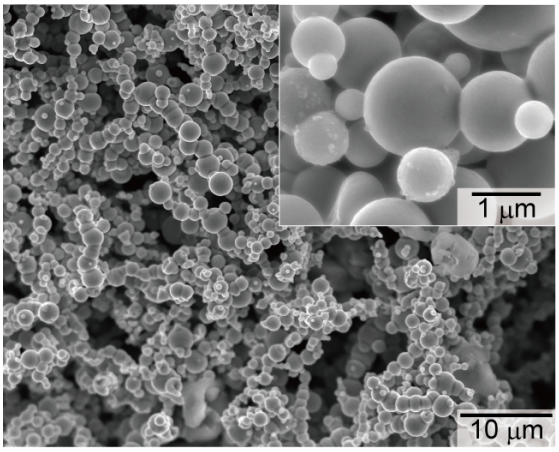

Figure 3.3 SEM images of the precipitates synthesized at 353 K from the solutions containing 0.050 M Co(II) and 5.0 x 10^{-1} M N_2H_4.

Figure 3.4 shows the photos of the QCM substrates immerged in the solutions at the different concentrations of N_2H_4. The weight change of cobalt deposited on the QCM

substrate is shown in Figure 3.5. The cobalt deposition is hardly observed on the QCM substrate at 2.5 x 10^{-3} M as shown in Figs. 3.4a and 3.5a. At 5.0 x 10^{-2} M and 0.50 M N_2H_4, the cobalt deposition is clearly observed on the QCM substrate (Figs. 3.4b and c). The weight of cobalt increases with time and reaches a constant value after a certain reaction time. The slope of the curves, which corresponds to the deposition rate of cobalt, becomes bigger at a higher concentration of N_2H_4 due to the higher reduction ability in reaction solution. On the other hand, the total amount of cobalt deposited on the QCM substrate after 60 minutes reaction is smaller at 0.50 M N_2H_4 than that at 5.0 x 10^{-2} M N_2H_4. At 0.50 M N_2H_4, a homogeneous nucleation of cobalt particles occurs in the solution, which suppresses a heterogeneous nucleation of cobalt on the QCM substrate. The relationship between the homogeneous nucleation of cobalt in solution and the heterogeneous nucleation of cobalt on the QCM substrate is circumstantially discussed in section 3.4.

Consequently, the concentration of N_2H_4 strongly affects the deposition behavior of cobalt by electroless deposition. The cobalt deposition was not observed at 2.5 x 10^{-3} M N_2H_4. At 5.0 x 10^{-2} M N_2H_4, the cobalt deposition was observed on the QCM substrate, however, the cobalt particles were not formed in the solution. Namely, this solution corresponds to the condition for the electroless plating of cobalt. At 0.50 M N_2H_4, the cobalt particles were formed by the homogeneous nucleation in the reaction solution.

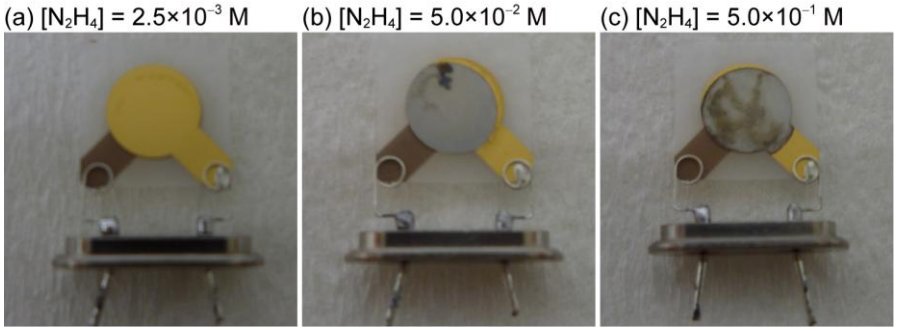

Figure 3.4 Photos of the gold-sputtered QCM substrates immerged in the solutions containing 0.050 M Co(II), (a) 2.5 x 10^{-3} M, (b) 5.0 x 10^{-2} M, and (c) 5.0 x 10^{-1} M N_2H_4.

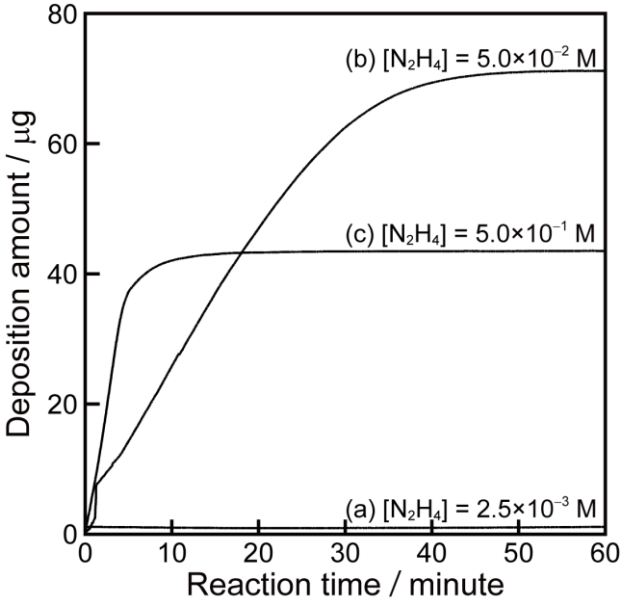

Figure 3.5 Weight change of metal deposited on the gold-sputtered QCM substrate from the solutions containing 0.050 M Co(II), (a) 2.5 x 10^{-3} M, (b) 5.0 x 10^{-2} M, and (c) 5.0 x 10^{-1} M N_2H_4.

3.3.2 Discussion

The results obtained through the present experiments are inevitable because it is easily expected that the cobalt deposition is more favorable at a higher concentration of N_2H_4. However, it is difficult to quantitatively predict a condition for cobalt deposition without

using the electrochemical in-situ measurements. In order to evaluate the driving force of the cobalt deposition, the redox potential of Co(II)/Co redox pair was measured by the EQCM method. The following reduction reaction of Co(II) was separately evaluated from the weight change of metal deposited on the QCM substrate

$$\mathrm{Co(II)} + 2\mathrm{e} \rightarrow \mathrm{Co} \qquad [3.1]$$

where Co(II) represents all the cobalt(II) species, e.g., Co^{2+}, $Co(OH)_2$, $HCoO_2^-$, and cobalt alkoxide sol.[10,11] Figure 3.6 shows cyclic voltammograms measured at 1 mV s^{-1} in 120 cm^3 of EG containing 0.050 M $CoCl_2 \cdot 6H_2O$ and 1.0 M NaOH by a potentiostat using the gold-sputtered QCM substrate as a working electrode. The photos of QCM substrates before and after the CV are shown in Figure 3.7. The surface of the gold-sputtered QCM substrate is almost entirely covered with cobalt metal after the 1st cycle. In the cyclic voltammogram by a potentiostat (Fig. 3.6, dotted line), the cathodic current of hydrogen generation (reductive decomposition of EG) is observed below –1.04 V in addition to the cathodic current of cobalt deposition. The oxidization current of adsorbed hydrogen on the QCM substrate is observed above –1.04 V only in the anodic sweep. The usual cyclic voltammogram by a potentiostat includes all the information of oxidation-reduction reactions on the QCM substrate. However, the cyclic voltammogram with the weight change of the QCM substrate only contains the information of cobalt deposition and cobalt dissolution (Fig. 3.6, solid line).

In the cyclic voltammogram by QCM, the cathodic current of cobalt deposition is seen below ca. –0.98 V vs. Ag/AgCl during the cathodic sweep. Once cobalt covers the gold-sputtered QCM substrate, the cobalt deposition is observed below ca. –0.85 V. Therefore, cobalt has a higher catalytic activity for cobalt deposition than gold, resulting in the small overpotential. Above –0.85 V, the anodic current of cobalt dissolution is observed. Thus, the redox potential of the Co(II)/Co redox pair can be determined to be approximately

–0.85 V vs Ag/AgCl. The anodic current due to the oxidation of cobalt is hardly observed above –0.64 V, which results from the passivation of cobalt.

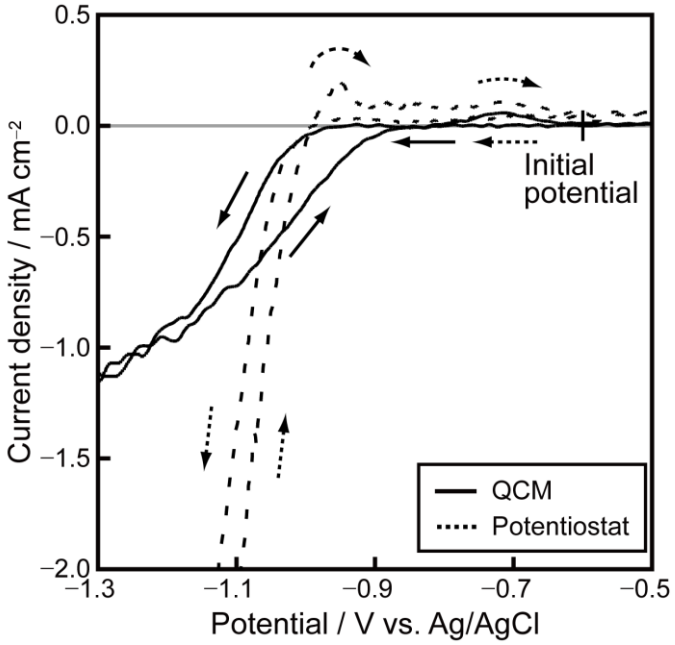

Figure 3.6 Cyclic voltammograms measured at 1 mV s^{-1} in EG containing containing 0.050 M $CoCl_2 \cdot 6H_2O$ and 1.0 M NaOH by a potentiostat (dotted line) and QCM (solid line). The initial potential is –0.64 V.

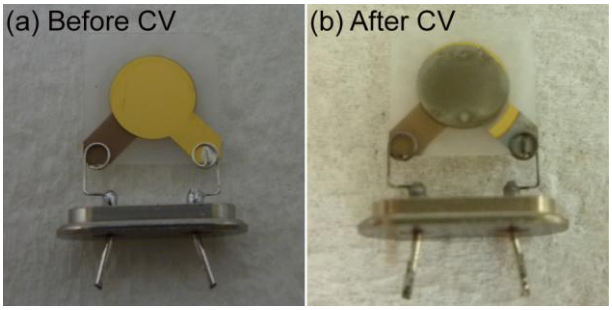

Figure 3.7 Photos of the QCM substrates (a) before and (b) after the CV measured at 1 mV s^{-1} in 120 cm^3 of EG containing 0.050 M $CoCl_2 \cdot 6H_2O$ and 1.0 M NaOH.

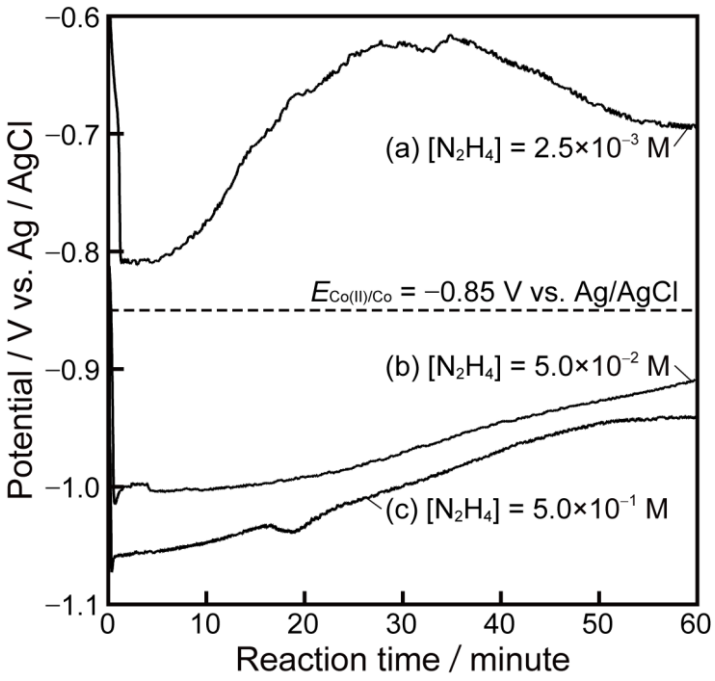

Figure 3.8 Time dependence of the mixed potential in the solution containing 0.050 M Co(II), (a) 2.5 x 10^{-3} M, (b) 5.0 x 10^{-2} M, and (c) 5.0 x 10^{-1} M N_2H_4. The redox potential of Co(II)/Co redox pair is also indicated.

Figure 3.8 shows the time-dependence of mixed potential in the solution during the sysnthesis of cobalt particles at various concentrations of N_2H_4. The redox potential of Co(II)/Co obtained in Fig. 3.6 is also indicated. The mixed potential becomes lower at a higher concentration of N_2H_4, which results from the bigger anodic current of N_2H_4 oxidation. At 2.5 x 10^{-3} M N_2H_4 (Fig. 3.8a), the mixed potential is higher than the redox potential of Co(II)/Co, indicating that the cobalt deposition is thermodynamically impossible. As described above, the cobalt deposition is not observed for this condition, which is consistent with the result of the mixed potential measurement. On the other hand, the mixed potential at 5.0 x 10^{-2} M and 0.50 M N_2H_4 is lower than the redox potential of Co(II)/Co. Therefore, it is predicted that the cobalt deposition is possible, and actually, the cobalt deposition is observed on the QCM substrate as shown in Figs. 3.5b and c. The driving force of the cobalt

deposition is higher at 0.50 M than that at 5.0 x 10^{-2} M N_2H_4, which results in the difference in the deposition behavior of cobalt. Namely, the formation of cobalt particles by the homogenous nucleation occurs at a high driving force of 0.50 M N_2H_4. At 5.0 x 10^{-2} M N_2H_4, the driving force of the cobalt deposition is not high enough for the homogenous nucleation but enough for the heterogeneous nucleation, resulting in the electroless plating of cobalt as shown in Fig. 3.5b.

The mixed potential increases with the reaction time due to the consumption of hydrazine for the reduction of hydrogen ions and the cobalt ions. Simultaneously, the redox potential of Co(II)/Co is expected to decrease with time due to the consumption of Co(II) ions for the cobalt deposition. Thus, the driving force of cobalt deposition, which corresponds to the difference of the mixed potential and the redox potential, decreases with time and the rate of cobalt deposition becomes more gentle. In this way, the comparison of the mixed potential and the redox potential evaluated by the EQCM method is effective for the estimation of the driving force of cobalt deposition.

3.4 Effect of the nucleating agent on formation of cobalt nanoparticles

To control the metallic nanoparticle size, silver nitrate ($AgNO_3$), palladium chloride ($PdCl_2$), ruthenium chloride ($RuCl_3$), and chloroplatinic acid (H_2PtCl_6) are often used as a nucleating agent.[12-15] It is considered that the nucleating agent, whose redox potential is much higher than that of the objective metal, provides many heterogeneous nucleation sites, resulting in the formation of abundant and fine particles.[16] The formation of platinum nuclei divides the nucleation and growth stages during the formation of cobalt particles, which gives us a sharper size distribution. Figure 3.9 shows the SEM images and the size distributions of cobalt particles synthesized at various concentrations of H_2PtCl_6. Small particles with a

narrow size distribution were actually obtained by the addition of H_2PtCl_6 under all conditions. In the absence of the nucleating agent, the largest particles of 926 nm in mean diameter were obtained. The mean diameter apparently decreased with increasing the concentrations of the nucleating agent, and the smallest particles of 98 nm in a mean diameter were obtained at the maximum concentration examined ($[H_2PtCl_6]$ = 5.0 mM). As indicated in Fig. 3.9a, the size distribution of cobalt particles was polydispersed and broadened without the addition of the nucleating agent. With increasing the concentration of the nucleating agent, the size distribution becomes sharper, suggesting that the addition of the nucleating agent H_2PtCl_6 separates the nucleaction and growth stages in the formation process of the cobalt nanoparticles.

Figure 3.10 shows the XRD patterns of the precipitates obtained at various concentrations of H_2PtCl_6. All particles obtained were mixtures of fcc and hcp cobalt particles regardless of the absence or presence of the nucleating agents.

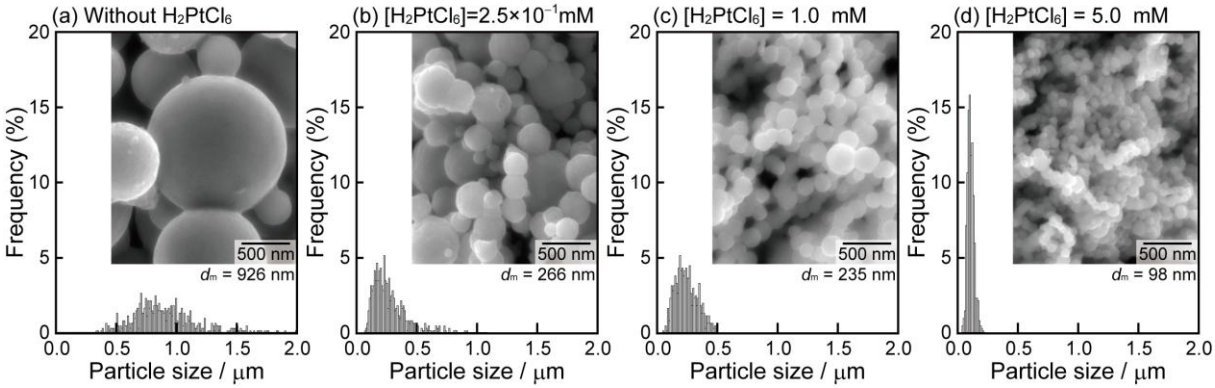

Figure 3.9 SEM images and size distributions of cobalt particles synthesized from solutions containing (a) 0, (b) 2.5 x 10^{-1}, (c) 1.0, and (d) 5.0 mM H_2PtCl_6 nucleating agent. Mean diameter $d_{m.}$ is also indicated.

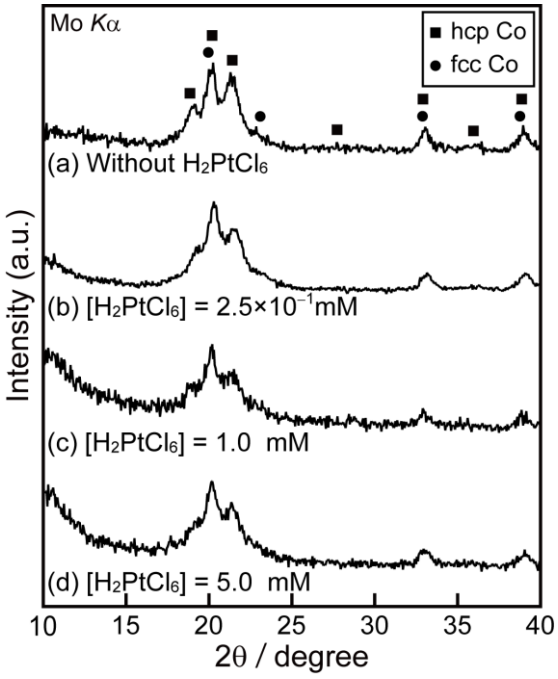

Figure 3.10 XRD patterns of cobalt particles synthesized from solutions containing (a) 0, (b) 2.5 x 10^{-1}, (c) 1.0, and (d) 5.0 mM H_2PtCl_6 nucleating agent.

Figure 3.11 shows the change in the mixed potential measured in the reaction solution. The initial mixed potential is in the range of –1.08 to –0.98 V vs Ag/AgCl, and the mixed potential gradually increases with time. However, the mixed potential is always below the redox potential of the Co(II)/Co redox pair (–0.85 V), indicating that cobalt nanoparticles can be deposited in this reaction condition. The mixed potential also increases with the additive amount of the nucleating agent. This is because minute cobalt particles are formed with the increasing concentration of the nucleating agent, which provides numerous active catalytic sites for hydrazine oxidation, resulting in the extensive consumption of hydrazine. The amount of hydrazine consumed for the reduction of cobalt(II) species is the same when all the cobalt(II) species are reduced. The difference in mixed potential is, therefore, mainly due to the difference in an amount of hydrazine consumed for hydrogen generation.

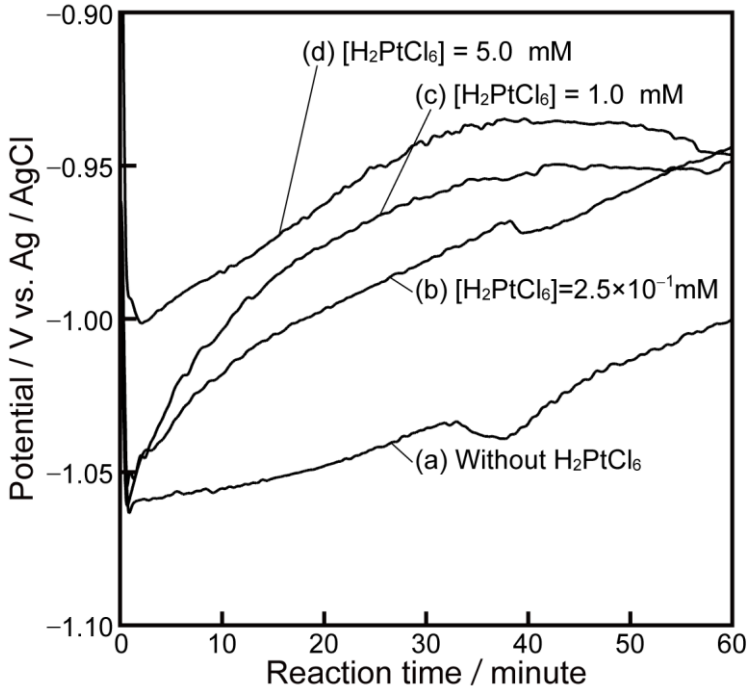

Figure 3.11 Change in mixed potential measured using a gold-sputtered QCM substrate in solutions containing (a) 0, (b) 2.5 x 10^{-1}, (c) 1.0, and (d) 5.0 mM H_2PtCl_6 nucleating agent.

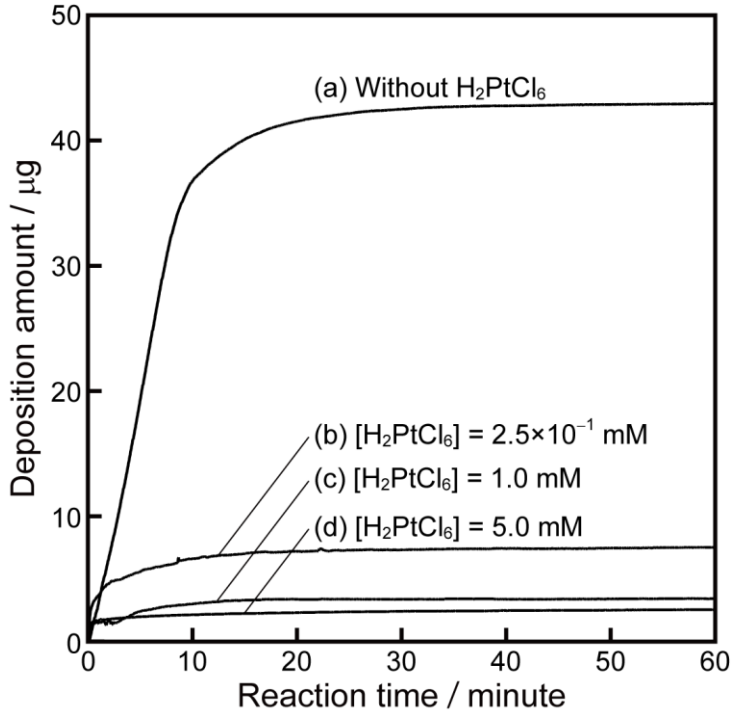

Figure 3.12 Weight change of cobalt deposited on a gold-sputtered QCM substrate from solutions containing (a) 0, (b) 2.5 x 10^{-1}, (c) 1.0, and (d) 5.0 mM H_2PtCl_6 nucleating agent.

Figure 3.12 shows the weight of cobalt deposited on the QCM substrate during the nanoparticle syntheses. The deposition rate and the total amount of cobalt deposited on the QCM substrate at certain times decreased with an increase in the nucleating agent. The total amount of deposition corresponds to the inhomogeneous nucleation on the QCM substrate, which is inversely related to the homogeneous nucleation in the reaction solution. The nucleating agent provides numerous nucleation sites in the reaction solution, which suppresses the heterogeneous nucleation of cobalt on the QCM substrate. Therefore, the homogeneous nucleation rate of metal in solution can be indirectly estimated by the total amount of deposition, which is useful to evaluate a formation mechanism of particles via electroless deposition.

3.5 Conclusions

In this chapter, the formation process of cobalt nanoparticles by electroless deposition in nonaqueous solution (EG) was investigated by the electrochemical in-situ measurements and the EQCM method. Through the present work, we have obtained the following results.

1. The formation of cobalt particles is strongly affected by a concentration of N_2H_4; the cobalt deposition is more favorable at a higher concentration of N_2H_4.
2. The driving force of metal deposition in nonaqueous solution is evaluated by comparing the mixed potential with the redox potential of metal experimentally obtained by the EQCM method.
3. The cobalt particles are formed by the homogenous nucleation at a high concentration of N_2H_4 0.50 M, where the mixed potential is much lower than the redox potential of Co(II)/Co redox pair.

4. The nucleating agent, $H_2PtCl_6 \cdot 6H_2O$, provides nucleation sites for the cobalt deposition, resulting in the formation of small cobalt particles.
5. The terminal point of the deposition reaction is directly determined by the in-situ QCM measurement, and additionally, the nucleation rate is indirectly evaluated by this method.

By using the in-situ mixed potential measurement in conjunction with EQCM method, we have experimentally demonstrated that the driving force of metal deposition can be evaluated even in nonaqueous system. This electrochemical analysis approach is effective even in the reaction systems where thermodynamic data are not insufficient.

References

1. D. Larcher and R. Patrice, *J. Solid State Chem.*, **154**, 405 (2000).
2. S. Yagi, T. Koyanagi, H. Nakanishi, T. Ichitsubo, and E. Matsubara, *J. Electrochem.Soc.*, **155**, D583 (2008).
3. M. D. L. Balela, S. Yagi, Z. Lockman, A. Aziz, A. V. Amorsolo, Jr., and E. Matsubara, *J. Electrochem. Soc.*, **156**, E139 (2009).
4. S. H. Wu and D.-H. Chen, *J. Colloid Interface Sci.*, **259**, 282 (2003).
5. G. Viau, F. Fiévet-Vincent and F. Fiévet, *J. Mater. Chem.*, **6**, 1047 (1996).
6. D. Kodama, K. Shinoda, K. Sato, Y. Konno, R. J. Joseyphus, K. Motomiya, H. Takahashi, T. Matsumoto, Y. Sato, K. Tohji, and B. Jeyadevan, *Adv. Mater*., **18**, 3154 (2006).
7. S. Bruckenstein and M. Shay, *Electrochim. Acta,* **30**, 1295 (1985).
8. K. Kanazawa and J. H. Gordon, II, *Anal. Chem.*, **57,** 1770 (1985).
9. Z. Jusys, H. Massong, and H. Baltruschatb, *J. Electrochem.Soc.*, **146**, 1093 (1999).
10. J. Chivot, L. Mendoza, C. Mansour, T. Pauporté, and M. Cassir, *Corros. Sci.*, **50**, 62

(2008).

11. N. Chakroune, G. Viau, S. Ammar, N. Jouini, P. Gredin, M. J. Vaulay, and F. Fiévet, *New J. Chem.*, **29**, 355 (2005).
12. M. Grzelczak, J. Pérez-Juste, B. Rodríguez-González, M. Spasova, I. Barsukov, M. Farle, and L. M. Liz-Marzán, *Chem. Mater.*, **20**, 5399 (2008).
13. G. Viau, P. Toneguzzo, A. Pierrard, O. Acher, F. Fiévet-Vincent, and F. Fiévet, *Scr. Mater.*, **44**, 2263 (2001).
14. R. J. Joseyphus, K. Shinoda, D. Kodama, B. Jeyadevan, *Materials Chemistry and Physics*, **123**, 487 (2010).
15. Y. Soumare, J.-Y. Piquemal, T. Maurer, F. Ott, G. Chaboussant, A. Falqui, and G. Viau, *J. Mater. Chem.*, **18**, 5659 (2008).
16. T. Sugimoto, *J. Colloid Interface Sci.*, **309**, 106 (2007).

Chapter 4

Formation of Nickel Nanowires via Electroless Deposition under a Magnetic Field

4.1 Introduction

Nanowires of iron group metals (i.e., Fe, Co, and Ni) and their alloys are attractive for applications to catalytic materials as well as magnetic materials with the magnetic shape anisotropy, as discussed in chapter 1.[1,2] Numerous synthesis methods of iron group nanowires have been reported.[3-8] In their methods, nanowires are formed by electrodeposition using templates such as anodized aluminum oxide[3-5] and polycarbonate membrane.[6-8] The methods with templates have notable advantages that highly-ordered and size-controlled nanowires can be obtained. The template methods, however, require several steps including fabrication and removal of templates in order to obtain bare nanowires. On the other hand, a self-assemble electroless deposition of ferromagnetic nanowires under a magnetic field is a relatively simple synthesis method without any templates.[9] In addition, electroless deposition is a powerful fabrication method with a wide variety of compositions and sizes in a large-scale[10,11] and thus, electroless deposition is suitable for a practical application.

In the previous chapters, we have reported some studies of electrochemical approaches with in-situ mixed potential observation for the synthesis processes of cobalt nanoparticles, which is effective in thermodynamic oxidation-state control and analysis of the formation process of nanowires as well as nanoparticles.[12] In the present chapter, the formation process of nickel nanowires via electroless deposition under a magnetic field was

electrochemically investigated. In order to control the morphology of nickel deposits, the deposition behavior of nickel was studied by an in-situ mixed potential measurement. The formation of nickel nanowires was investigated by the in-situ QCM measurement in conjunction with the mixed potential measurement. Furthermore, the reduction rate and the reduction potential of Ni(II) species were investigated by voltammetry combined with QCM as well as the oxidation rate and oxidation potential of hydrazine as a counterpart reaction. These methods are useful for optimization of a preparation condition to obtain nanowires with a smooth surface and a high aspect ratio.

4.2 Experimental

4.2.1 Synthesis method and characterization of nickel nanoparticles and nanowires

The reaction solutions were prepared using nickel chloride hexahydrate ($NiCl_2 \cdot 6H_2O$) as a source of nickel ions, ethylene glycol (EG) as a solvent, and hydrazine monohydrate ($N_2H_4 \cdot H_2O$) as a reducing agent. Sodium hydroxide (NaOH) was used as a source of OH^- ions. Trisodium citrate dihydrate ($Na_3C_6H_5O_7 \cdot 2H_2O$) and chloroplatinic acid hexahydrate ($H_2PtCl_6 \cdot 6H_2O$) were used as a complexing agent and a nucleating agent, respectively. These reagents are all reagent-grade (Nacalai Tesque, Inc.) and used without further purification.

First, 27 cm^3 EG solution containing 0.100 M $NiCl_2$, 0.2 - 1.4 M NaOH, and 0 - 10.0 mM $Na_3C_6H_5O_7$ was prepared, where M corresponds to mol dm^{-3}. For experiments with a nucleating agent, H_2PtCl_6 (0.02 - 2.00 mM) was added as a nucleating agent. The same amount of EG solution (27 cm^3) containing 1.00 M N_2H_4, 0 - 0.6 M NaOH, and 0 - 10.0 mM $Na_3C_6H_5O_7$ was also prepared. The compositions of reaction solutions are summarized in Table 4.1. The temperature of the solutions was kept at 353 K with nitrogen gas bubbling to

remove the dissolved oxygen. The metallic salt solution and the hydrazine solution were mixed at 353 K. After mixing of the metallic salt solution and the hydrazine solution, the concentratios of Ni(II) and N_2H_4 are 0.050 M and 0.50 M, respectively. The reaction solution was agitated at a rate of 500 rpm with a magnetic stirring unit at 353 K during the reaction for the synthesis of nickel particles. For the synthesis of nickel wires, the reaction solution was kept at 353 K in a water bath located inside the two parallel neodymium magnets (100 x 100 mm) separated 100 mm apart, as schematically drawn in Figure 4.1. A magnetic field inside the magnets was about 100 - 200 mT, which is measured by a Tesla meter (KANETEC Co., Ltd., TM-601). After the reaction, nickel particles and wires were washed several times with ethanol.

The morphology of products was observed by a field-emission scanning electron microscope (JEOL Ltd., JSM-6500F). The mean diameter and size distribution of the nickel particles and wires were determined by an image analysis for randomly selected 600 particles and 300 wires in each sample.

Table 4.1 Compositions of the metallic salt solutions and the hydrazine solutions for the synthesis of nickel particles and wires.

	Compositions of metallic salt solutions				Compositions of hydrazine solutions		
	$[NiCl_2]$ (M)	[NaOH] (M)	$[Na_3C_6H_5O_7]$ (mM)	$[H_2PtCl_6]$ (mM)	$[N_2H_4]$ (M)	[NaOH] (M)	$[Na_3C_6H_5O_7]$ (mM)
(a)	0.100	1.4	–	–	1.00	0.6	–
(b)	0.100	0.3	–	–	1.00	0.1	–
(c)	0.100	0.2	–	–	1.00	–	–
(d)	0.100	1.4	5.0	–	1.00	0.6	5.0
(e)	0.100	1.4	7.5	–	1.00	0.6	7.5
(f)	0.100	1.4	10.0	–	1.00	0.6	10.0
(g)	0.100	1.4	10.0	0.02	1.00	0.6	10.0
(h)	0.100	1.4	10.0	0.20	1.00	0.6	10.0
(i)	0.100	1.4	10.0	2.00	1.00	0.6	10.0

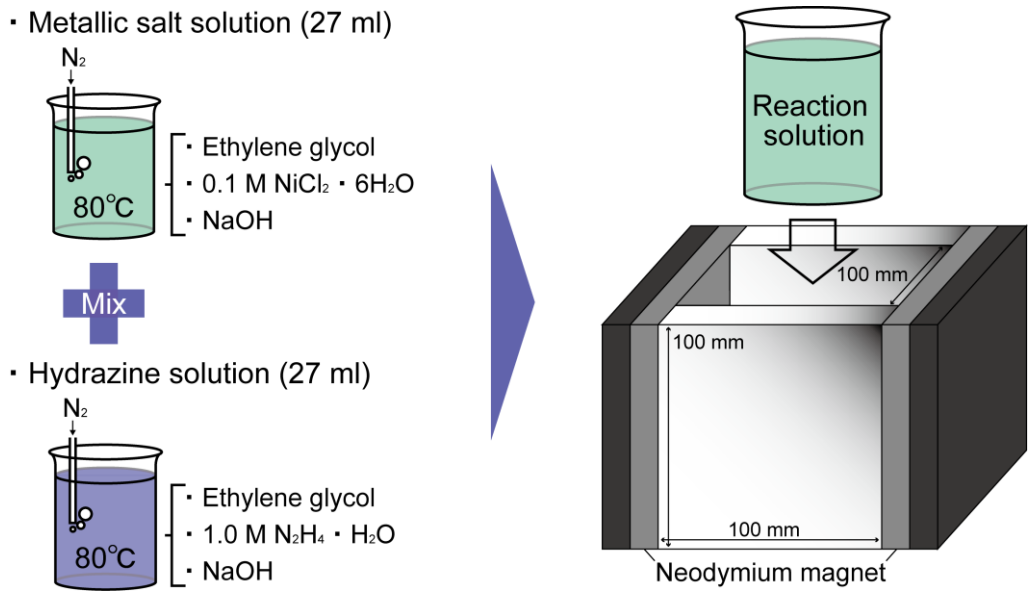

Figure 4.1 Schematic illustration of the set up for the synthesis of nickel nanowires by electroless deposition under a magnetic field.

4.2.2 In-situ electrochemical measurements of nickel deposition

During the synthesis of nickel particles, a gold-sputtered QCM electrode (SEIKO EG&G, QA-A9M-AU) was immersed in the reaction solution and the mixed potential on the QCM electrode was measured by a potentiostat/galvanostat (Hokuto Denko Co., Ltd., HA-151) using a Ag/AgCl (3.33 M KCl) electrode (Horiba, 2565A-10T) as a reference electrode. The weight of nickel deposited on the QCM electrode, Δm, was calculated from the change in resonance frequency of the QCM electrode, Δf, by Sauerbrey's equation.

4.2.3 Measurement of the CV profiles in nickel salt solution by EQCM

The cyclic voltammogram was measured in 120 cm^3 of EG solution containing 0.050 M $NiCl_2$ and 0.1 - 1.0 M NaOH by the potentiostat/galvanostat using a nickel-sputtered QCM electrode (SEIKO EG&G, QA-A9M-AU) as a working electrode, a platinum electrode (20 x

20 mm) as a counter electrode, and a Ag/AgCl electrode as a reference electrode. During the measurement, the temperature of the solution was kept at a reaction temperature of 353 K on a hot plate with nitrogen gas bubbling to remove the dissolved oxygen.

4.2.4 Measurement of anodic polarization curves in hydrazine solution

The anodic polarization curves were measured in 120 cm^3 of EG solution containing 0.50 M N_2H_4 and 0.1 - 1.0 M NaOH by the potentiostat/galvanostat using a nickel substrate (10 x 10 mm) as a working electrode, a platinum electrode (20 x 20 mm) as a counter electrode, and a Ag/AgCl electrode as a reference electrode. During the measurement, the temperature of the solutions was kept at a reaction temperature of 353 K on a hot plate with nitrogen gas bubbling to remove the dissolved oxygen.

4.3 Results

Figure 4.2 shows the size distributions and scanning electron microscopy (SEM) images of nickel particles synthesized without a magnetic field at different concentrations of NaOH. In the absence of a magnetic field, nickel particles were obtained as shown in Figs. 4.2a-c. The size of particles increases with a decrease in a concentration of NaOH. The average particle size is about 240 nm at 1.0 M NaOH and 480 nm at 0.1 M NaOH. The size distribution becomes sharper at a higher concentration of NaOH.

Figure 4.3 shows the SEM images of nickel particles and wires synthesized from the solutions under a magnetic field at different concentrations of NaOH. At 1.0 M NaOH, nickel particles about 250 nm in diameter were obtained. Beads-like nickel wires were obtained at 0.2 M NaOH. Nickel wires approximately 500 nm in diameter with a smooth surface were obtained at 0.1 M NaOH. It should be noted that there is no large change of the

each particle size with and without a magnetic field at the same concentration of NaOH. These results also indicate that a magnetic field strongly affects the morphology of nickel.

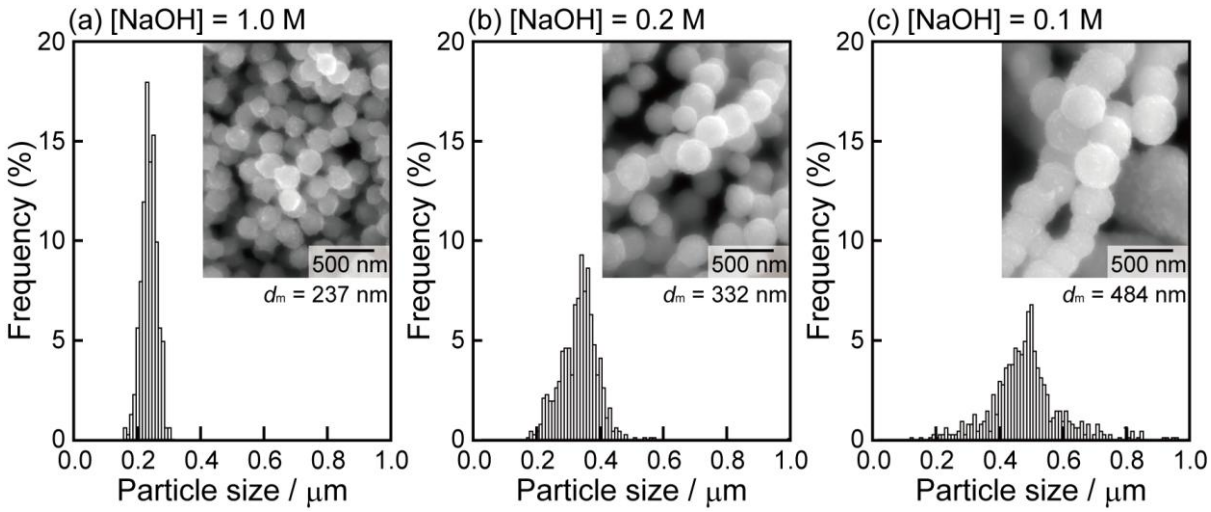

Figure 4.2 Size distributions and SEM images of nickel particles synthesized from solutions containing 0.050 M $NiCl_2$, 0.50 M N_2H_4, (a) 1.0 M, (b) 0.2 M, and (c) 0.1 M NaOH. Mean diameter $d_{m.}$ is also indicated.

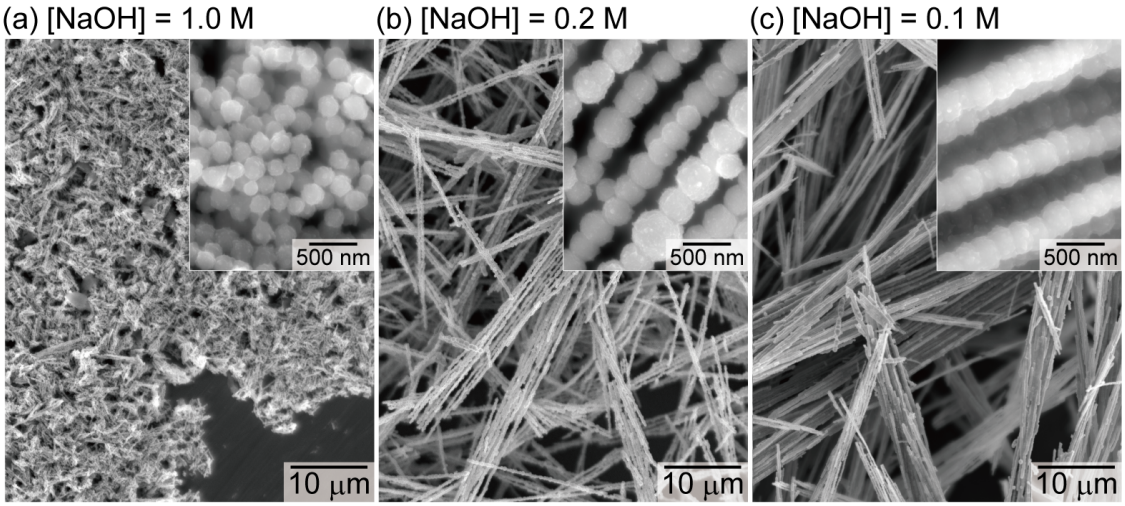

Figure 4.3 SEM images of nickel nanoparticles and nanowires synthesized from solutions containing 0.050 M $NiCl_2$, 0.50 M N_2H_4, (a) 1.0 M, (b) 0.2 M, and (c) 0.1 M NaOH under a magnetic field.

In the present process, the following hydrazine oxidation reactions mainly occur as anodic reactions;

$$N_2H_4 + 4OH^- \rightarrow N_2 + 4H_2O + 4e \quad [4.1]$$

Figure 4.4 shows anodic polarization curves measured on nickel substrates in 120 cm^3 EG containing 0.50 M N_2H_4 and 0.1 - 1.0 M NaOH. The oxidation potential of hydrazine positively shifts from –1.06 to –0.85 V vs Ag/AgCl and the slope of the anodic current density becomes smaller with decrease in a concentration of NaOH. The conductivity of the solution becomes lower with decreasing a concentration of NaOH. The conductivities measured by a conductivity electrode (Horiba, 9382-10D) are 2.12, 1.27, and 0.72 S m^{-1} at 1.0, 0.2, and 0.1 M NaOH, respectively. The large change of anodic current density at different concentrations of NaOH cannot be obviously explained only by the change of the solution resistance. Considering the increased ohmic drop due to the solution resistance, the slope of the I/V curve is still smaller at a lower concentration of NaOH. This indicates that a reduction ability of hydrazine becomes weaker at a lower concentration of NaOH.

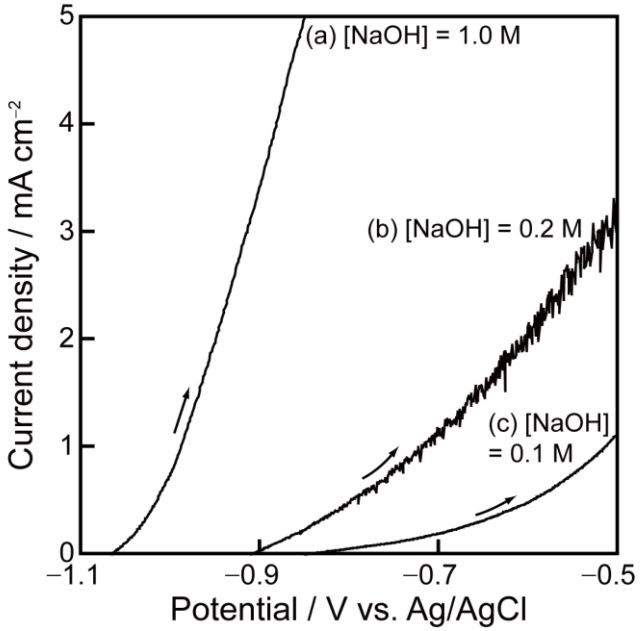

Figure 4.4 Anodic polarization curves measured at 1 mV s^{-1} in EG containing 0.50 M N_2H_4, (a) 1.0 M, (b) 0.2 M, and (c) 0.1 M NaOH.

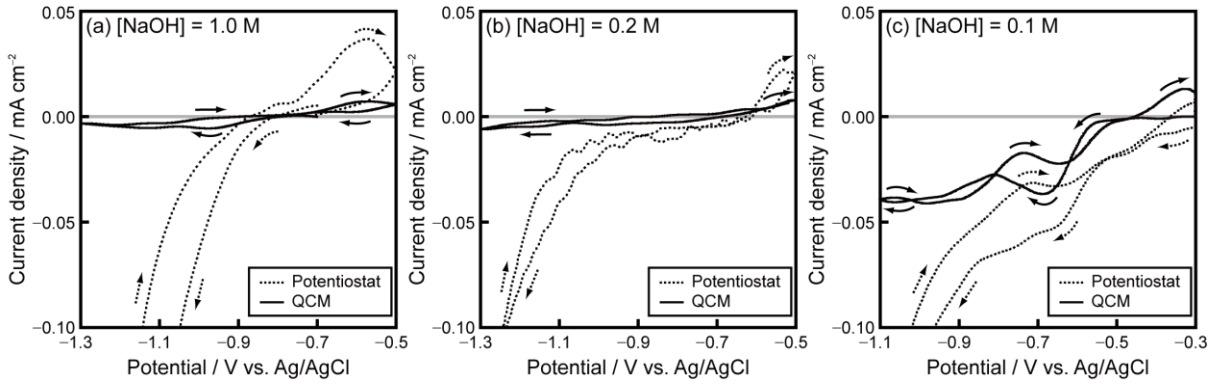

Figure 4.5 Cyclic voltammograms measured by potentiostat (dotted line) and QCM (solid line) at 1 mV s^{-1} in EG containing 0.050 M $NiCl_2$, (a) 1.0 M, (b) 0.2 M, and (c) 0.1 M NaOH.

Both a weight of deposited metal and a total current density are simultaneously measured by the voltammetry with the QCM electrode. The following reduction reaction of Ni(II) species was separately evaluated from the weight change of nickel deposited on the QCM substrate

$$\mathrm{Ni(II)} + 2\mathrm{e} \rightarrow \mathrm{Ni} \qquad [4.2]$$

where Ni(II) represents all the nickel(II) species, e.g. Ni^{2+}, $NiOH^{+}$, $Ni(OH)_2$, $HNiO_2^{-}$, and NiO_2.[2-13] The contribution of the reductive decomposition of the solvent to the total current density is dominant in this process, and the current density due to nickel deposition is hardly observed by a normal voltammetry. Figure 4.5 shows cyclic voltammograms measured in 120 cm^3 EG containing 0.050 M $NiCl_2$ and 0.1 - 1.0 M NaOH. At 1.0 M NaOH (Fig. 4.5a, dotted line), the cathodic current of hydrogen generation is observed below about –0.80 V vs Ag/AgCl during the cathodic sweep, and the oxidization current of hydrogen adsorbed on the QCM substrate is observed above –0.87 V. In a cyclic voltammogram evaluated from the weight change by QCM (solid line), the nickel reduction was observed below about –0.80 V during the cathodic sweep, and the dissolution of nickel was seen above –0.80 V during the

anodic sweep. Therefore, the redox potential of Ni(II)/Ni redox pairs is about −0.80 V vs Ag/AgCl at 1.0 M NaOH. Similarly, the redox potential of Ni(II)/Ni redox couple can be determined to be about −0.70 V and −0.45 V at 0.2 M and 0.1 M NaOH, respectively. Therefore, it is clarified that the redox potential of Ni(II)/Ni redox pairs shifts to the negative direction by increasing the concentration of NaOH. The reduction current density of Ni(II) species is much smaller at 1.0 and 0.2 M compared with that at 0.1 M NaOH. This is because Ni(II) ions in the metallic salt solution were hydroxylated to form green nickel hydroxide and/or nickel alkoxide sol by the addition of NaOH, which results in the low current efficiency of the nickel deposition as shown in Fig. 4.5. An activity of Ni^{2+} ions decreases with an increase of the concentration of NaOH and the redox potential of Ni(II)/Ni shifts to the negative direction according to the Nernst equation.

Figure 4.6 shows the time transition in the mixed potential on the QCM substrate during the synthesis. Just after mixing the metallic salt solution and the hydrazine solution, the mixed potential rapidly dropped below the redox potentials of Ni(II)/Ni in each condition, indicating that nickel deposition is thermodynamically possible. At a lower concentration of NaOH, the mixed potential positively shifts, which corresponds to the result that the current density of hydrazine oxidation declines with decrease in a concentration of NaOH. An increase of potential with time can be mainly attributed to a consumption of hydrazine, because the mixed potential is mainly determined by the balance of hydrazine oxidation reactions and decomposition of large amount of solvent.

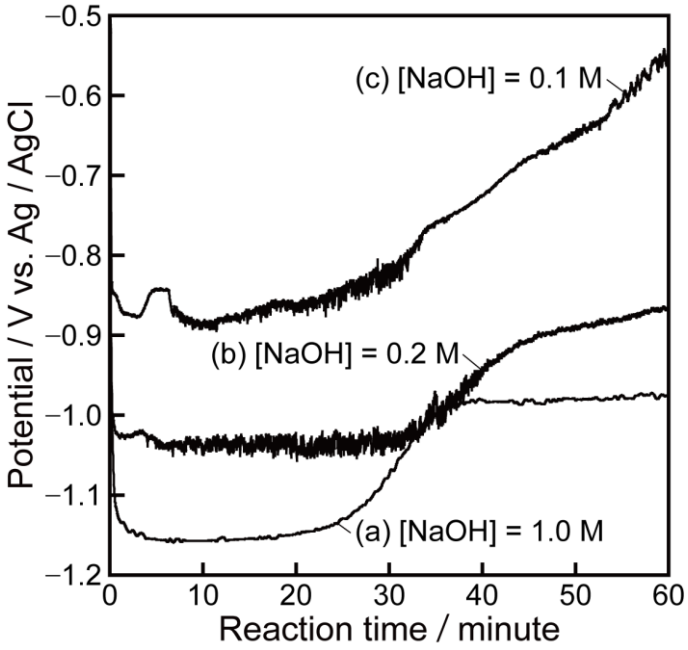

Figure 4.6 Time dependence of mixed potential in solutions containing 0.050 M $NiCl_2$, 0.50 M N_2H_4, (a) 1.0 M, (b) 0.2 M, and (c) 0.1 M NaOH.

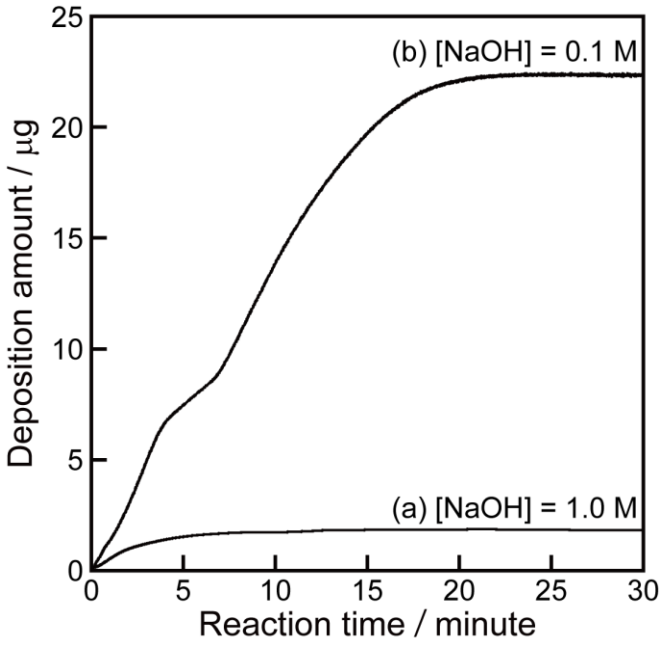

Figure 4.7 Weight of nickel deposited on the gold-sputtered QCM substrate immersed in the solutions containing 0.050 M $NiCl_2$, 0.50 M N_2H_4, (a) 1.0 M and (b) 0.1 M NaOH.

The weight change of nickel deposited on the QCM substrate is shown in Figure 4.7. The weight increases with time and reaches a constant value after a certain reaction time. We defined it as a terminal point of the deposition reaction of nickel. At 1.0 M NaOH, the terminal point of the deposition reaction is about 10 minutes which is shorter than that at 0.1 M NaOH. Additionally, the slope of the curve, which corresponds to the deposition rate, is smaller and the final weight of nickel deposited on a QCM substrate decreases at 1.0 M NaOH in comparison with 0.1 M NaOH. As discussed in chapter 3, the total amount of deposited nickel on the QCM substrate corresponds to the heterogeneous nucleation, which is inversely related to the homogeneous nucleation in the reaction solution. The heterogeneously deposited metal is suppressed by the addition of NaOH due to the enhancement of the homogeneous nucleation in the solution. By referring the SEM images in Figs. 4.3a-c, we noted that the formation of wires becomes easier when the terminal time of the deposition reaction becomes longer.

4.4 Discussion

The concentration of NaOH significantly affects on both the hydrazine oxidation reactions and the nickel deposition reactions. With decreasing the amount of NaOH, the reduction ability of hydrazine becomes weaker, and as a result, the mixed potential becomes higher as shown in Fig. 4.4 and Fig. 4.6. Thus, the driving force of nickel deposition becomes larger and the homogeneous nucleation of nickel is favorable at a higher concentration of NaOH. On the other hand, the deposition current density of nickel is much smaller at 1.0 M NaOH than that at 0.1 M NaOH as shown in Fig. 4.5, which indicates that the particle growth is suppressed at a higher NaOH concentration. Consequently, the finer nickel particles with a narrower size distribution are achieved at 1.0 M NaOH (Fig. 4.2a).

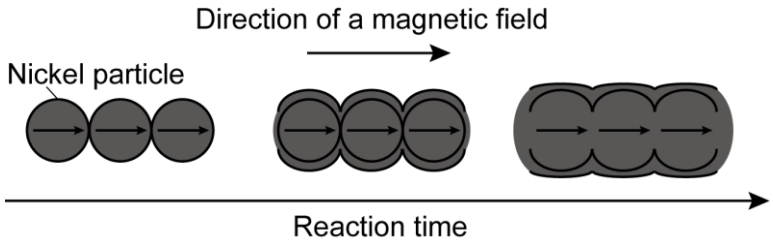

Figure 4.8 Schematic illustration of the formation process of nickel wires by elecrtoless desposition under a magnetic field.

The morphological change in nickel wires is explained by the formation mechanism of nickel wires schematically drawn in Fig. 4.8. First, nickel particles are formed in the reaction solution in the initial reaction stage, and are aligned along a magnetic field due to magnetic interaction. Then, nickel preferentially deposits at the necks between particles to decrease the interfacial energy. The particles are tightly connected and finally form rigid wires with a smooth surface. Therefore, the necessary condition for the formation of nickel wires is that the alignment of particles occurs prior to the completion of the reduction reaction.

At 1.0 M NaOH, the reduction ability of hydrazine is so high that a large amount of nickel nuclei are rapidly formed, and the nickel deposition has finished before the alignment of particles. The nickel particles are not tightly connected under a magnetic field because of their fast reduction rate at 1.0 M NaOH. It is likely that the nickel wires easily broke down during washing in ethanol as shown in Fig. 4.3a. At a lower concentration of NaOH, the reduction ability of hydrazine is not so high that there is enough time for the particles to align along the magnetic field and are connected by preferential deposition at the necks between them. Thus, the nickel wires are obtained at a lower concentration of NaOH as shown in Figs. 4.3b,c. The wires are beads-like shape at 0.2 M NaOH and become smooth at 0.1 M NaOH.

In order to verify this formation mechanism of nickel wires, the nickel wires were fabricated by adding a complexing agent, $Na_3C_6H_5O_7$. Generally, complexing agents such as citrate, whose complex formation constant with Ni(II) ions is high, are used for a control of the activity of Ni(II) ions and the deposition rate.[14,15] Figure 4.9 shows the time transition in the weight change of metals deposited on the QCM substrate without and with trisodium citrate dihydrate, $Na_3C_6H_5O_7$. Actually, the deposition rate of nickel can be controlled by addition of 10.0 mM $Na_3C_6H_5O_7$ and the terminal point becomes longer about 35 minutes. Figure 4.10 shows the SEM images of nickel deposits synthesized from the reaction solutions containing 0.050 $NiCl_2$, 0.50 M N_2H_4, 1.0 M NaOH, and 5.0 - 10.0 mM $Na_3C_6H_5O_7$ under a magnetic field. While nickel particles were obtained without $Na_3C_6H_5O_7$ (Fig. 4.3a), beads-like nickel wires whose diameter is about 320 nm were formed at 5.0 mM $Na_3C_6H_5O_7$ (Fig. 4.10a). The surface of nickel wires becomes smoother at a higher concentration of $Na_3C_6H_5O_7$ (Figs. 4.10b and c). Consequently, the formation of wires becomes easier at a slower reaction rate as it is expected from the discussion above.

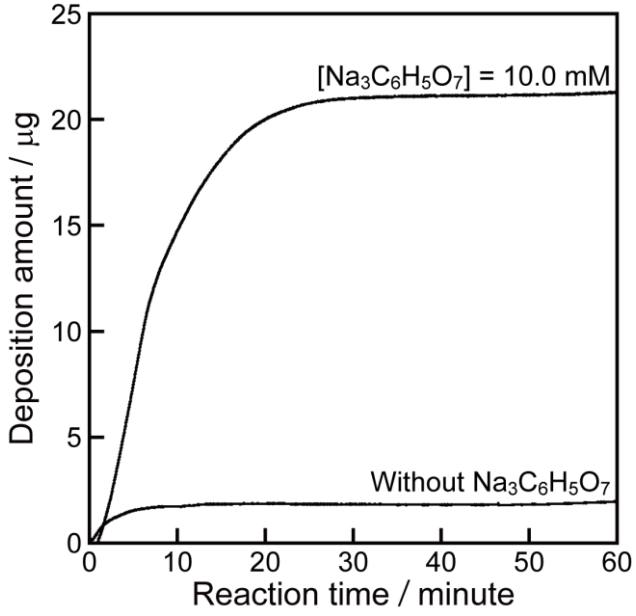

Figure 4.9 Weight of nickel deposited on the gold-sputtered QCM substrate immersed in the solutions containing 0.050 M $NiCl_2$, 0.50 M N_2H_4, 1.0 M NaOH, without $Na_3C_6H_5O_7$ and with 10.0 mM $Na_3C_6H_5O_7$.

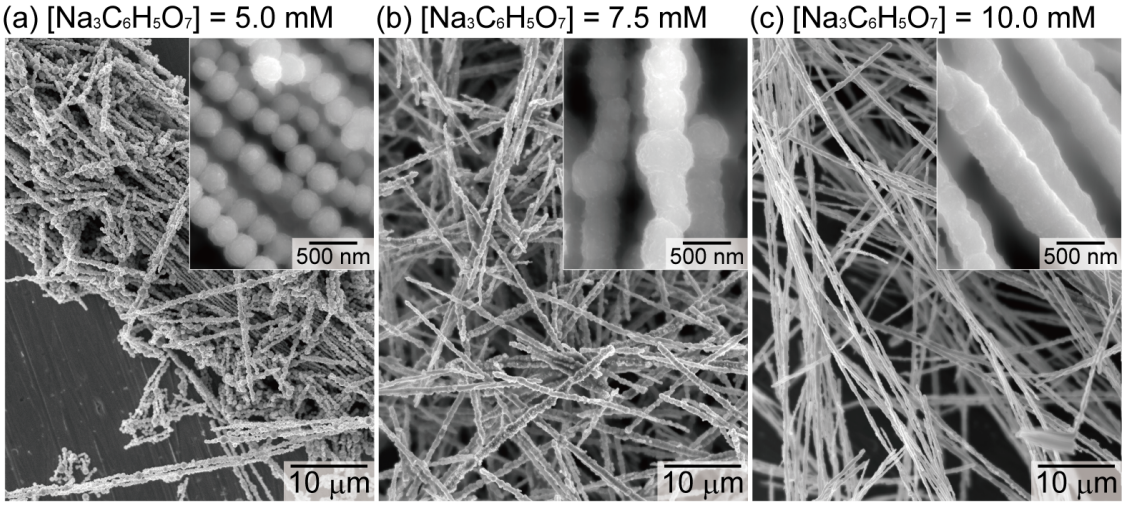

Figure 4.10 SEM images of nickel nanowires synthesized from solutions containing 0.050 M $NiCl_2$, 0.50 M N_2H_4, 1.0 M NaOH, (a) 5.0 mM, (b) 7.5 mM, and (c) 10.0 mM $Na_3C_6H_5O_7$ under a magnetic field.

In the present results, it is important that the nickel wires are formed after the formation of nickel particles. Therefore, we can apply the same size-control method as particles synthesis by electroless deposition for the diameter control of nickel wires. To control the nickel particle size, chloroplatinic acid (H_2PtCl_6) is often used as a nucleating agent.[16,17] It is considered that the nucleating agent, whose redox potential is much higher than that of the objective metal, provides many heterogeneous nucleation sites, resulting in the formation of abundant and fine particles. The formation of platinum nuclei divides the nucleation and growth stages during the formation of nickel particles, which gives us a sharper size distribution. Figure 4.11 shows the SEM images and the size distributions of nickel wires synthesized from the solutions containing 0.050 $NiCl_2$, 0.50 M N_2H_4, 1.0 M NaOH, 10.0 mM $Na_3C_6H_5O_7$, and 0.01 - 1.00 mM H_2PtCl_6. The diameter of nickel wires becomes thinner and the size distribution gets narrower with an increase in a concentration of H_2PtCl_6. The average diameters were 280 nm, 160 nm, and 100 nm at 0.01 mM, 0.10 mM, and 1.00 mM H_2PtCl_6, respectively. In this way, the wire diameter can be easily controlled by the additive amount of nucleating agents.

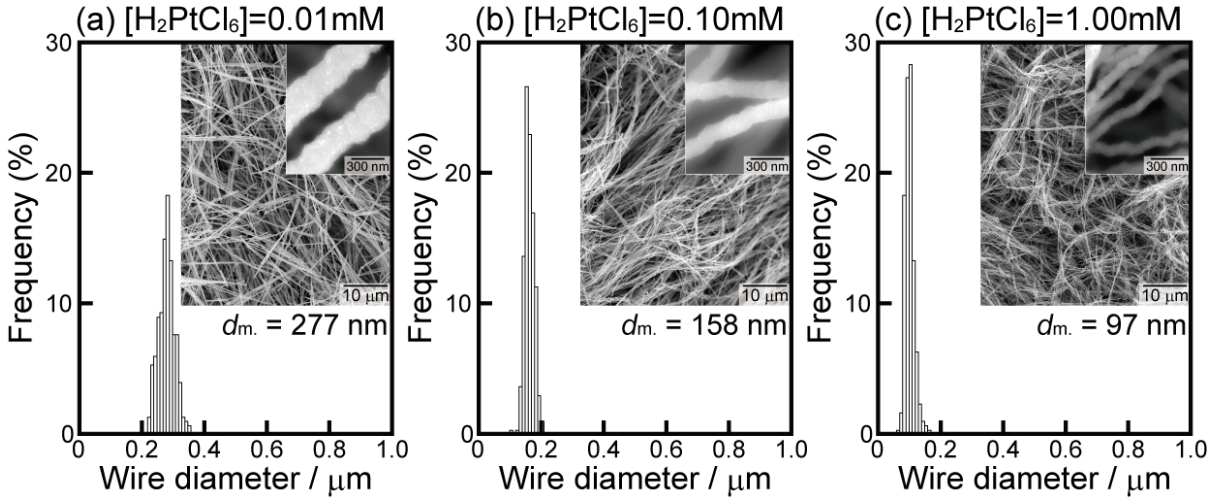

Figure 4.11 SEM images and size distribution of nickel wires synthesized from solutions containing 0.050 M $NiCl_2$, 0.50 M N_2H_4, 1.0 M NaOH, 10.0 mM $Na_3C_6H_5O_7$, (a) 0.01 mM, (b) 0.10 mM, and (c) 1.00 mM H_2PtCl_6. Mean diameter $d_{m.}$ is also indicated.

4.5 Conclusion

In the present work, the formation process of nickel wires by electroless deposition under a magnetic field was electrochemically investigated. The formation mechanism of nickel wires was proposed on the basis of the electrochemical measurements. Through the present experiments, we have obtained the following results.

1. The necessary condition for the formation of nickel wires is that the alignment of particles occurs prior to the completion of the reduction reaction.
2. The reduction ability of hydrazine oxidation reactions becomes lower at a lower concentration of NaOH, resulting in a longer terminal time of the nickel deposition reaction and realizing the formation of smooth nickel wires.
3. The rate of nickel deposition reaction can also be controlled by the addition of a complexing agent, $Na_3C_6H_5O_7$. The nickel wires with a smooth surface and a high-aspect ratio are obtained by adjusting a concentration of $Na_3C_6H_5O_7$.
4. The diameter of nickel wires were controlled from 100 nm to 370 nm by the addition of a nucleating agent, H_2PtCl_6.

References

1. Y. Xia, P. Yang, Y. Sun, Y. Wu, B. Mayers, B. Gates, Y. Yin, F. Kim, and H. Yan, *Adv. Mater.*, **15**, 353 (2003).
2. J. I. Martíına, J. Nogués, K. Liu, J. L. Vicent, I. K. Schuller, *J. Magn. Magn. Mater.*, 256, 449 (2003).
3. K. Nielsch, F. Müller, A.-P. Li, and U. Gösele, *Adv. Mater.*, **12**, 582 (2000).
4. H. Pan, H. San, C. Poh, Y. Feng, and J. Lin, *Nanotechnology*, **16**, 1559 (2005).
5. J.-H. Lim, A. Rotaru, S.-G. Min, L. Malkinski, and J. B. Wiley, *J. Mater. Chem.*, **20**, 9246 (2010).
6. M. Tian, J. Wang, J. Kurtz, T. E. Mallouk, and M. H. W. Chan, *Nano Lett.*, **3**, 919 (2003).
7. Y. Fukunaka, M. Motoyama, Y. Konishi, and R. Ishii, *Electrochem. Solid-State let.*, **9**, C62 (2006).
8. S. Sharma, A. Barman, M. Sharma, L. R. Shelford, V. V. Kruglyak, and R. J. Hicken, *Solid State Communications*, **149**, 1650 (2009).
9. V. V. Sviridov, G. P. Shevchenko, A. S. Susha, and N. A. Diab, *J. Phys. Chem.*, **100**, 19632 (1996).
10. S.-H. Wu and D.-H. Chen, *J. Colloid Interface Sci.*, **259**, 282 (2003).
11. M. Grzelczak, J. Pérez-Juste, B. Rodríguez-Gonzáles, M. Spasova, I. Barsukov, M. Farle, and L. M. Liz-Marzán, *Chem. Mater.*, **20**, 5399 (2008).
12. S. Yagi, M. Kawamori, and E. Matsubara, *Electrochem. Solid-State Lett.*, **13**, E1 (2010).
13. M. Pourbaix, *Atlas of Electrochemical Equilibria in Aqueous Solutions*, p. 330, Cebelcor, Brüssel (1966).
14. S. Yagi, A. Kawakami, K. Murase, and Y. Awakura, *Electrochimica Acta*, **52**, 6041 (2007).

15. O. Younes and E. Gileadi, *J. Electrochem. Soc.*, **149**, C100 (2002).

16. G. Viau, P. Toneguzzo, A. Pierrard, O. Acher, F. Fiévet-Vincent, and F. Fiévet, *Scr. Mater.*, **44**, 2263 (2001).

17. M. D. L. Balela, S. Yagi, Z. Lockman, A. Aziz, A. Jr. Amorsolo, and E. Matsubara, *J. Electrochem. Soc.*, **156**, E139 (2009).

Chapter 5

Nickel Alloying Effect on Formation of Cobalt Nanoparticles and Nanowires

5.1 Introduction

In the previous chapter, we have succeeded in the fabrication of the nickel nanowires by the electroless deposition based on the formation mechanism of the nanowires.[1] In the synthesis of the nanowires under a magnetic field, the magnetic properties of the nanoparticles definitely affect the morphology of the nanowires because the nanoparticles are firstly formed prior to the formation of the nanowires. Thus, in the present chapter, the effect of the magnetic properties on the formation of the nanowires was investigated in the Co-Ni system as an example.

The morphology of the metallic nanowires is also affected by the deposition rate of metal as well as the magnetic properties of the particles. As demonstrated in the previous chapter, the nanowires exhibiting a smooth surfabe and a high-aspect ratio are obtained at a low deposition rate of metal, which can be controlled by adjusting concentrations of NaOH and/or complexing agents. The deposition rate of alloy changes depending on the metal composition, since each metal has an individual catalytic activity in the oxidation reaction of a reducing agent.[2-4] Therefore, it is quite important to understand the catalytic activities of metal in order to control the nanowire morphology.

In the present chapter, first, the electrochemical behavior in the formation of Co-Ni nanoparticles was carefully studied using the in-situ mixed potential measurement and the in-situ quartz crystal microbalance (QCM) measurement. We also investigated the catalytic

activities of cobalt and nickel in the reduction reaction of metallic ions and the oxidation reaction of a reducing agent by using a cyclic voltammetry with a QCM electrode. Then, the effect of the magnetic properties of the Co-Ni alloys on the formation of the Co-Ni nanowires was discussed based on the results of the electrochemical measurements.

5.2 Experimental

The reaction solutions were prepared using cobalt chloride hexahydrate ($CoCl_2 \cdot 6H_2O$) and nickel chloride hexahydrate ($NiCl_2 \cdot 6H_2O$) as a source of cobalt and nickel ions, ethylene glycol (EG) as a solvent, and hydrazine monohydrate ($N_2H_4 \cdot H_2O$) as a reducing agent. Sodium hydroxide (NaOH) was used as a source of OH^- ions. Chloroplatinic acid hexahydrate ($H_2PtCl_6 \cdot 6H_2O$) was used as a nucleating agent. These reagents are all reagent-grade (Nacalai Tesque, Inc.) and used without further purification.

First, 27 cm^3 EG solution containing 0.10 M metallic salts ($[CoCl_2] + [NiCl_2] = 0.10$ M) and 0.3 M NaOH was prepared, where M is mol dm^{-3}. For the experiments with a nucleating agent, 0.20 mM H_2PtCl_6 was added. The same amount of EG solution (27 cm^3) containing 1.00 M N_2H_4 and 0.1 M NaOH was also prepared. The compositions of reaction solutions are summarized in Table 5.1. The temperature of the solutions was kept at 353 K with nitrogen gas bubbling to remove the dissolved oxygen. The metallic salt solution and the hydrazine solution were mixed at 353 K to start the reaction. The reaction solution was agitated at a rate of 500 rpm with a magnetic stirring unit at 353 K during the reaction for the syntheses of Co-Ni particles. For the syntheses of Co-Ni wires, the reaction solution was kept at 353 K in a water bath located inside the two parallel neodymium magnets (100 x 100 mm) separated 100 mm apart. After the reaction, particles and wires were washed several times with ethanol.

The morphology of precipitates was observed using a field-emission-scanning electron microscope (JEOL Ltd., JSM-6500F). The mean diameter and size distribution of the Co-Ni particles were determined by image analysis for randomly selected 600 particles in each sample. The compositions of Co-Ni particles and wires were analyzed with energy-dispersive X-ray (EDX) spectrometry. The crystalline structure of precipitates was investigated by X-ray diffraction (XRD, Rigaku Co., Ltd., RINT-2200) using Cr *K*α radiation. A superconducting quantum interference device (Quantum Design, Inc., MPMS SQUID XL) was used to measure the magnetic hysteresis curves of the particles at room temperature.

During the syntheses of Co-Ni particles, the gold-sputtered QCM electrode (SEIKO EG&G QA-A9M-AU) was immersed in the reaction solution and the mixed potential of the QCM electrode was measured by a potentiostat/galvanostat (Hokuto Denko Co., Ltd., HA-151) using a Ag/AgCl (3.33 M KCl) electrode (Horiba 2565A-10T) as a reference electrode. The weight of deposits on the QCM electrode, Δm, was calculated from the change in resonance frequency of the QCM electrode, Δf, by Sauerbrey's equation. The cyclic voltammograms were also measured by the potentiostat/galvanostat using a gold or nickel-sputtered QCM electrode (SEIKO EG&G QA-A9M-NI) as a working electrode, a platinum electrode (20 x 20 mm) as a counter electrode, and a Ag/AgCl electrode as a reference electrode.

Table 5.1 Compositions of metallic salt solutions and hydrazine solutions for the syntheses of Co-Ni nanoparticles and nanowires.

	Compositions of metallic salt solutions				Compositions of hydrazine solutions	
	[$CoCl_2$] (M)	[$NiCl_2$] (M)	[NaOH] (M)	[H_2PtCl_6] (mM)	[N_2H_4] (M)	[NaOH] (M)
(a)	0.100	–	0.3	–	1.00	0.1
(b)	0.070	0.030	0.3	–	1.00	0.1
(c)	0.050	0.050	0.3	–	1.00	0.1
(d)	0.030	0.070	0.3	–	1.00	0.1
(e)	–	0.100	0.3	–	1.00	0.1
(f)	0.100	–	0.3	0.20	1.00	0.1
(g)	0.070	0.030	0.3	0.20	1.00	0.1
(h)	0.050	0.050	0.3	0.20	1.00	0.1
(i)	0.030	0.070	0.3	0.20	1.00	0.1
(j)	–	0.100	0.3	0.20	1.00	0.1

5.3 Results

Figure 5.1 shows scanning electron microscopy (SEM) images and size distributions of particles synthesized in the different concentration ratios of Co(II) to Ni(II). The mean diameter of the particles is also indicated. In the absence of H_2PtCl_6, the mean particle diameters are 1300 nm and 330 nm at [Co(II)] : [Ni(II)] = 100 : 0 and 0 : 100, respectively (Figs. 5.1a and e). The particle size decreases and the size distribution becomes sharper with an increase in a concentration of Ni(II) (Figs. 5.1b-d). By the addition of H_2PtCl_6, the particle size largely decreased in all samples (Figs. 5.1f-j). The nucleating agent such as H_2PtCl_6, whose redox potential is much higher than that of the objective metal, provides many heterogeneous nucleation sites, resulting in the formation of abundant and fine particles.[5,6] The provided platinum nuclei separates the nucleation and growth stages during the formation of Co-Ni particles, which gives us a sharper size distribution. On the other hand, size

reduction of Co-Ni particles by addition of Ni(II) is observed with and without H_2PtCl_6. The standard electrode potential of Ni(II)/Ni redox pair ($E_{Ni(II)/Ni}$ = −0.250 V vs. SHE) is close to that of Co(II)/Co pair ($E_{Co(II)/Co}$ = −0.277 V vs. SHE).[7] Thus, the formation of smaller particles by the addition of Ni(II) is not explained like the case of the nucleating agent of H_2PtCl_6. The atomic ratios of cobalt to nickel in the particles are almost equal to the ratios of Co(II) to Ni(II) ions in solution as it is seen in Table 5.2.

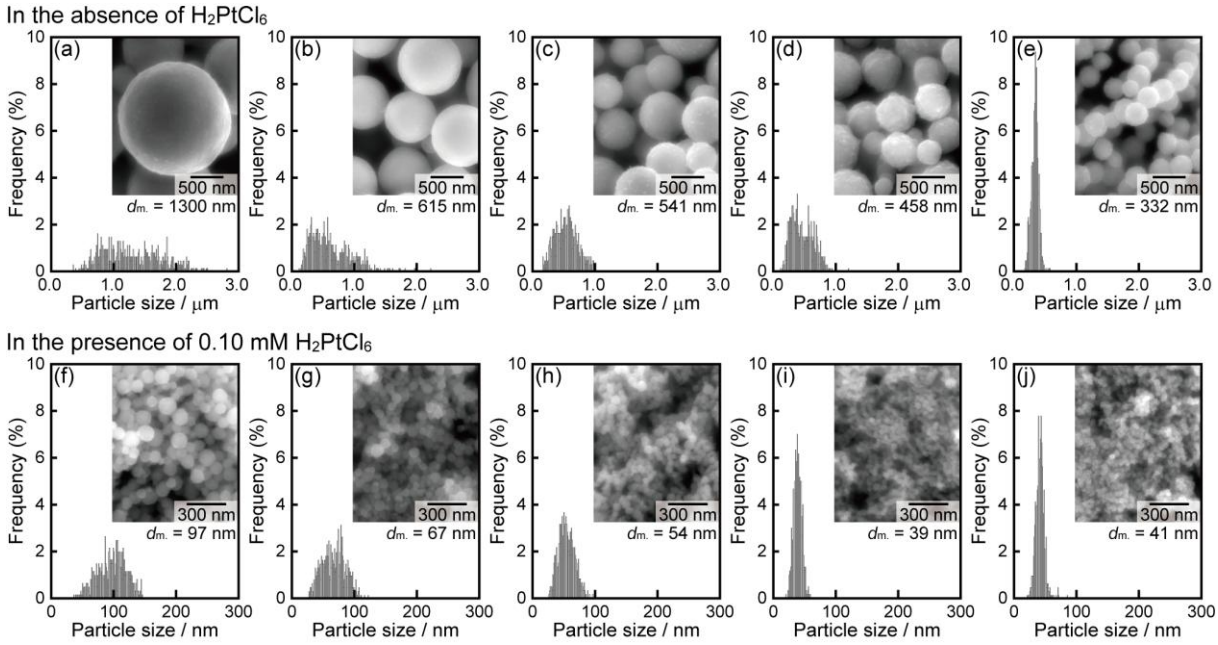

Figure 5.1 SEM images and size distribution of the particles synthesized from the solutions containing (a) 0.050 M Co(II), (b) 0.035 M Co(II) - 0.015 M Ni(II), (c) 0.025 M Co(II) - 0.025 M Ni(II), (d) 0.015 M Co(II) - 0.035 M Ni(II), and (e) 0.050 M Ni(II) in the absence H_2PtCl_6, and (f) 0.050 M Co(II), (g) 0.035 M Co(II) - 0.015 M Ni(II), (h) 0.025 M Co(II) - 0.025 M Ni(II), (i) 0.015 M Co(II) - 0.035 M Ni(II), and (j) 0.050 M Ni(II) in the presence of 0.10 mM H_2PtCl_6. Mean diameter $d_{m.}$ is also indicated.

Table 5.2 Atomic ratios of metal in the particles synthesized by changing the concentration ratio of Co(II) to Ni(II) in the reaction solution.

Concentration ratio of metallic species in the reaction solution [Co(II)] : [Ni(II)]	With or without of H_2PtCl_6	Atomic ratio of metal (atom%) Co	Ni
(a) 100 : 0	–	100.0	0.0
(b) 70 : 30	–	70.3	29.7
(c) 50 : 50	–	50.4	49.6
(d) 30 : 70	–	29.9	70.1
(e) 0 : 100	–	0.0	100.0
(f) 100 : 0	x	100.0	0.0
(g) 70 : 30	x	69.8	30.2
(h) 50 : 50	x	49.4	50.6
(i) 30 : 70	x	30.3	69.7
(j) 0 : 100	x	0.0	100.0

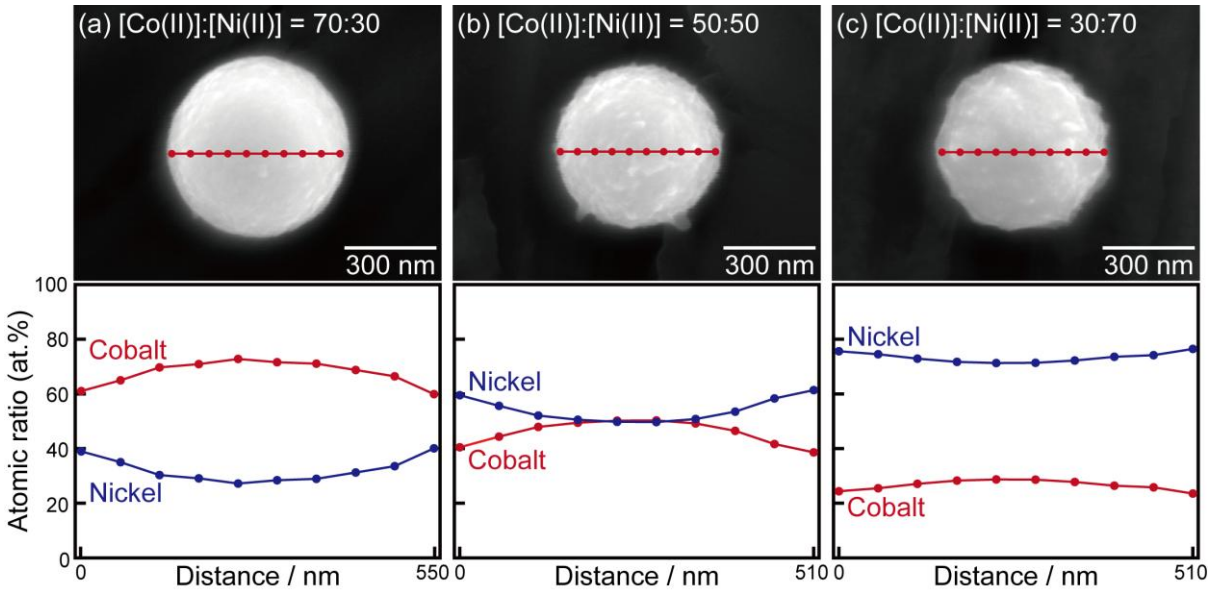

Figure 5.2 SEM images and atomic ratios of cobalt and nickel of particles synthesized from the solutions containing (a) 0.035 M Co(II) - 0.015 M Ni(II), (b) 0.025 M Co(II) - 0.025 M Ni(II), and (c) 0.015 M Co(II) - 0.035 M Ni(II).

Figure 5.2 shows the atomic ratios of cobalt and nickel at the points indicated in the SEM images of Co-Ni alloy particles. A small composition gradient is observed in the particles at all concentration ratios. The atomic fraction of cobalt is slightly higher at the core of the particles than at the edge. In contrast, that of nickel is lower at the core than at the edge. Consequently, although atomic concentrations of the particles are equal to the nominal concentration in a macro-scopic scale, the concentration fluctuations exist within the particles.

Figure 5.3 shows XRD patterns of the particles. The hexagonal close-packed (hcp) peaks of cobalt and the face-centered cubic (fcc) peaks of nickel are observed at [Co(II)] : [Ni(II)] = 100 : 0 and 0 : 100, respectively. In the XRD patterns of Co-Ni alloy particles, both fcc and hcp peaks are observed. The intensity of (100) hcp cobalt peak around 63.8° decreases with increasing a concentration of Ni(II). Additionally, a symmetry of the largest peak around 68.5° improves at a higher concentration of Ni(II), indicating that the contribution of peaks due to fcc structure becomes dominant. By the addition of H_2PtCl_6, the peak width slightly becomes broader in each concentration ratio (Figs. 5.3f-j), which is due to a decrease in the crystallite size. In pure cobalt, a hcp structure is stable at the room temperature and transforms to the fcc phase at 695 K according to the Co-Ni phase diagram as shown in Figure 5.4.[8] This allotropic transformation temperature decreases by alloying with nickel. At present reaction temperature of 353 K, the hcp and fcc phases are stable below about 25 atom%Ni and above 35 atom%Ni, respectively. Both phases coexist between these nickel concentrations. Thus, both the fcc and hcp phases are the equilibrium phase at Co : Ni = 70 : 30 (atom%) and the fcc phase at Co : Ni = 50 : 50 and 30 : 70 (atom%) at 353 K.

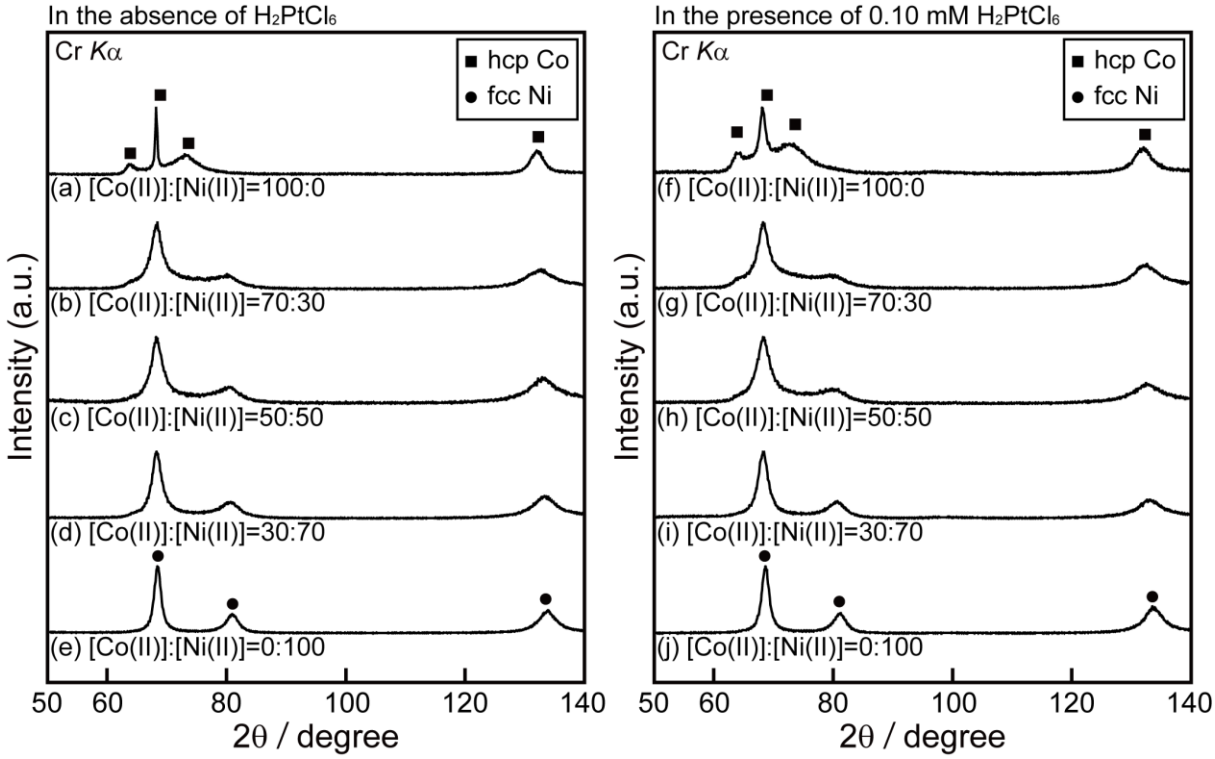

Figure 5.3 XRD patterns of the particles synthesized from the solutions containing (a) 0.050 M Co(II), (b) 0.035 M Co(II) - 0.015 M Ni(II), (c) 0.025 M Co(II) - 0.025 M Ni(II), (d) 0.015 M Co(II) - 0.035 M Ni(II), (e) 0.050 M Ni(II) in the absence of H_2PtCl_6, and (f) 0.050 M Co(II), (g) 0.035 M Co(II) - 0.015 M Ni(II), (h) 0.025 M Co(II) - 0.025 M Ni(II), (i) 0.015 M Co(II) - 0.035 M Ni(II), (j) 0.050 M Ni(II) in the presence of 0.10 mM H_2PtCl_6.

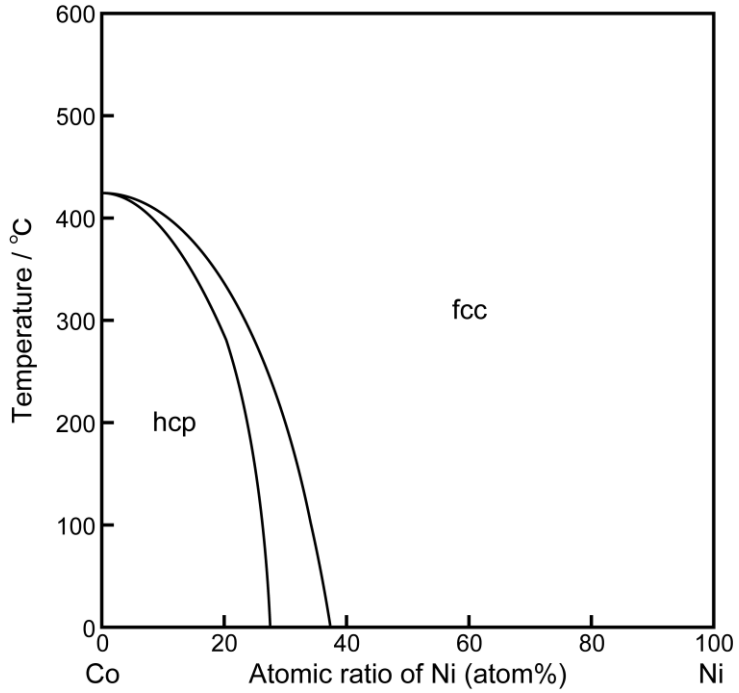

Figure 5.4 Phase diagram of the Co-Ni binary system.[8]

It is not presently understood whether these particles involve independent hcp and fcc particles or whether one particle includes both the hcp and fcc phases at [Co(II)] : [Ni(II)] = 50:50 and 30:70. This can be confirmed by annealing; when one particle includes both the hcp and fcc phases, hcp grains must disappear by annealing. Figure 5.5 shows the SEM images of the particles annealed at 623 K in Ar atmosphere for 16 hours. Neither sintering nor agglomeration among the particles is observed. Additionally, the surface of the annealed particles is relatively smoother than that of the as-prepared particles. The XRD patterns of annealed particles and the lattice parameters calculated by the position of the fcc 200 peak at around 80° are shown in Figure 5.6. The peaks in the XRD patterns of annealed particles become sharper because of the grain growth by annealing. The small diffuse peaks due to 100 hcp peak at 63.8° observed in the as-prepared particles at [Co(II)] : [Ni(II)] = 50 : 50 and 30 : 70 (Figs. 5.3c,d) completely disappeared after annealing, which is consistent with the phase expected in the phase diagram. This shows that hcp and fcc phases originally coexisted in one particle. As shown in Fig. 5.6B, the lattice parameters change approximately with the linear function of the composition of Ni(II) between the two lattice parameters of metastable fcc cobalt and fcc nickel, obeying the Vegard's law.[8,9] This indicates that Co-Ni solid solutions were formed in the particles after annealing.

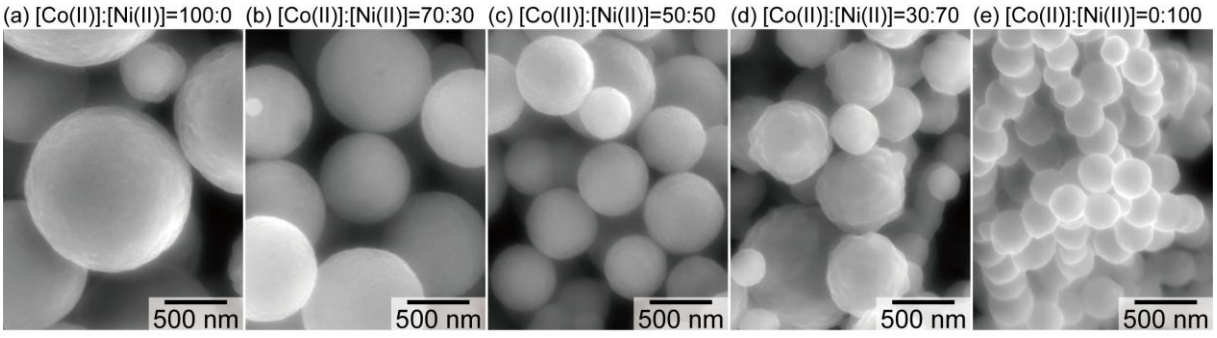

Figure 5.5 SEM images of the particles of (a) to (e) in Figure 5.1 annealed at 623 K for 16 hours.

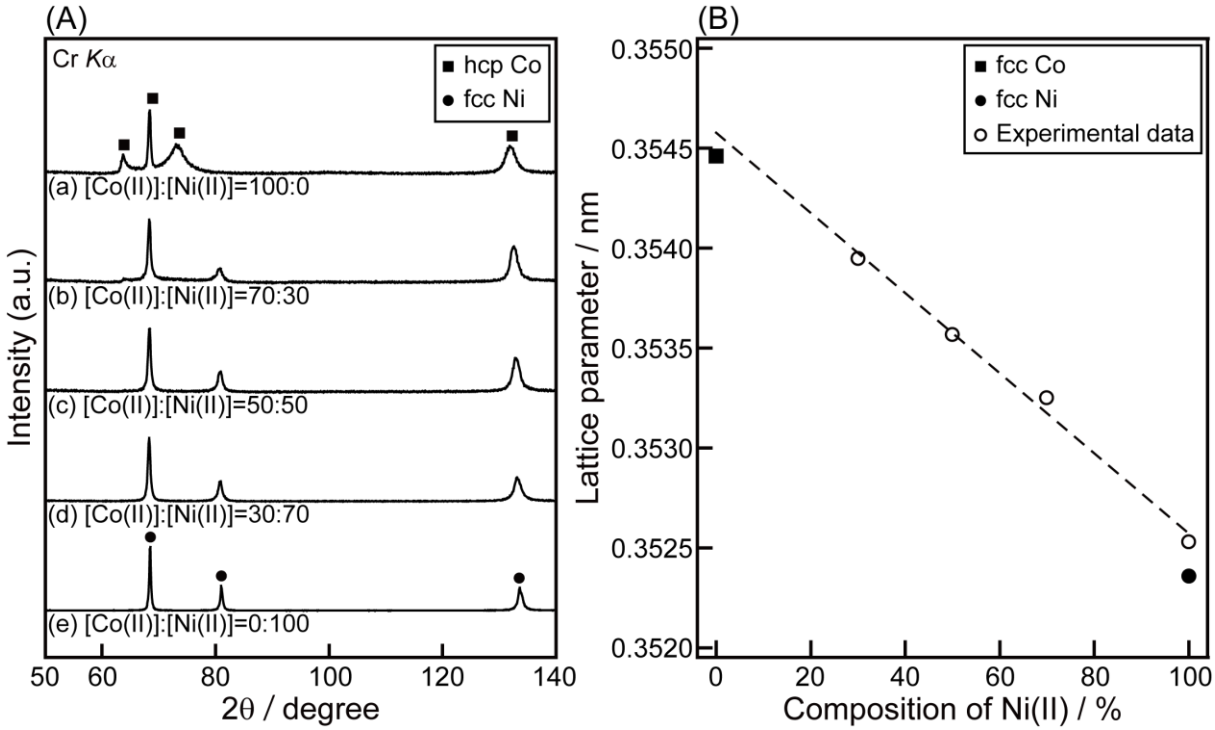

Figure 5.6 (A) XRD patterns of the particles of (a) to (e) in Figure 1 annealed at 623 K for 16 hours and (B) change in lattice parameters of annealed particles with composition of Ni(II).

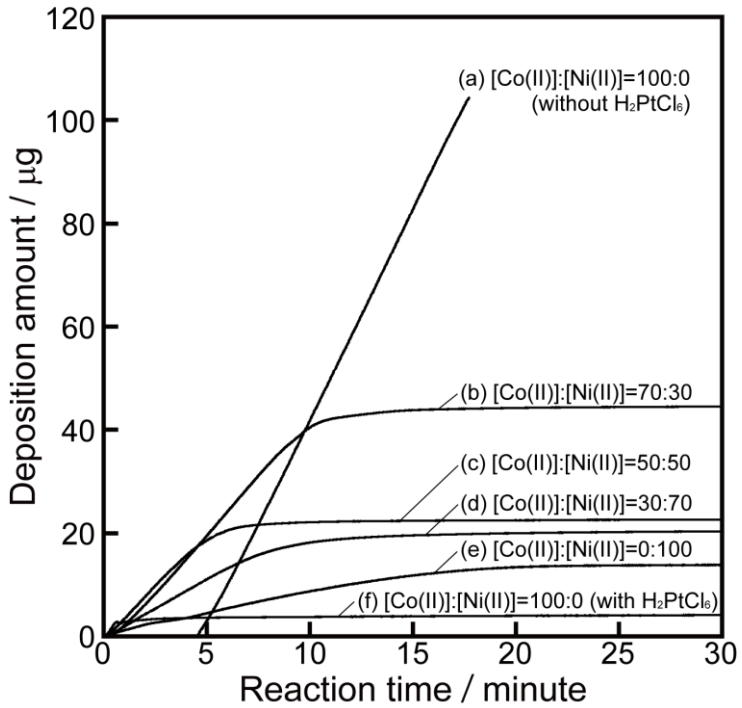

Figure 5.7 Weight of metal deposited on the gold-sputtered QCM substrate from the solutions containing (a) 0.050 M Co(II), (b) 0.035 M Co(II) - 0.015 M Ni(II), (c) 0.025 M Co(II) - 0.025 M Ni(II), (d) 0.015 M Co(II) - 0.035 M Ni(II), (e) 0.050 M Ni(II), and (f) 0.050 M Co(II). H_2PtCl_6 is added only in the solution (f).

Figure 5.7 shows the weight change of metals deposited on the QCM substrate during the syntheses of nanoparticles with different concentration ratios of Co(II) to Ni(II). At [Co(II)] : [Ni(II)] = 100 : 0 in the absence of H_2PtCl_6 (Fig. 5.7a), the cobalt deposition is observed at about 4 minutes after mixing the solutions containing Co(II) and hydrazine. The weight of cobalt reaches 105 μg in 17 minutes, which is the maximum value observable in the present system. The slope of the curve, which is the deposition rate, becomes smaller and the final weight of metal deposited on a QCM substrate decreases with an increase in a concentration of Ni(II). Also, the amounts of cobalt in the presence of H_2PtCl_6 (Fig. 5.7f) is about 4 μg which is much smaller than that in the absence of H_2PtCl_6 (Fig. 5.7a). Considering that the same amount of Co(II) dissolves in the reaction solution in the both cases and the formation of platinum particles provides nucleation sites of cobalt which suppresses the heterogeneous nucleation on the QCM substrate, we conclude that the decrease in the amounts deposited on the QCM substrate by the addition of Ni(II) is due to the enhancement of the homogeneous nucleation in the solution.

Figure 5.8 shows SEM images of wires synthesized from the solutions under a magnetic field at the different concentration ratios of Co(II) to Ni(II). While the surface of cobalt wires is relatively smooth (Fig. 5.8a), the surface of Co-Ni wires becomes rougher at a higher concentration of Ni(II) (Figs. 5.8b-d) and beads-like wires were obtained at [Co(II)] : [Ni(II)] = 0:100 (Fig. 5.8e). The diameter of wires decreases with an increase in a concentration of Ni(II). Cobalt and Co-Ni nanowires whose diameter is smaller than 100 nm were obtained by the addition of 0.10 mM H_2PtCl_6. Beads-like nickel nanowires of 40 nm in diameter were formed from the solution containing 0.050 M Ni(II). It is likely that the formation of wire becomes more difficult at a higher Ni(II) concentration. It is also noted that the diameter of the nanoparticles without a magnetic field is close to that of the nanowires

with a magnetic field at the same concentration ratio of Co(II) to Ni(II) (see Fig. 5.1 and Fig. 5.8).

Table 5.3 shows the atomic ratios of metals in the nanowires. The alloy compositions are close to the ratios of Co(II) to Ni(II) ions in solution as it is seen in the particles of Table I. Figure 5.9 shows XRD patterns of the wires. The peak positions and peak widths are almost the same as those of the particles in Fig. 5.3. Thus, the basic formation processes are similar in both nanoparticles and nanowires.

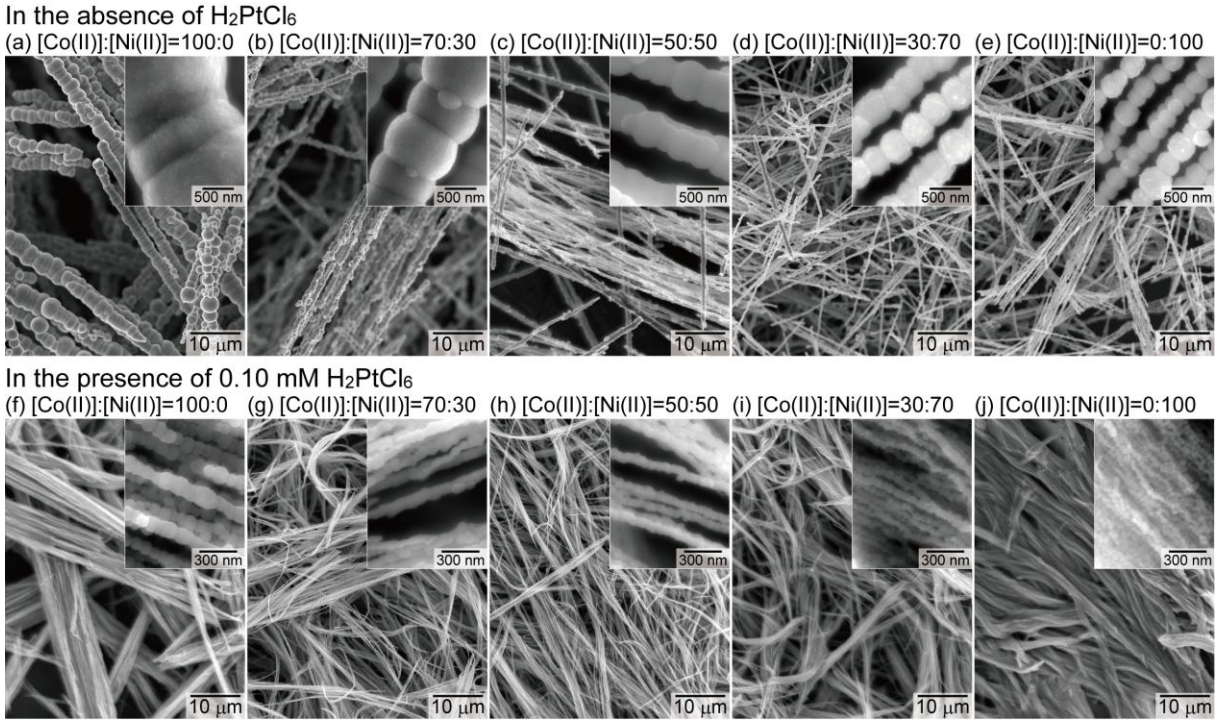

Figure 5.8 SEM images of the wires synthesized from the solutions containing (a) 0.050 M Co(II), (b) 0.035 M Co(II) - 0.015 M Ni(II), (c) 0.025 M Co(II) - 0.025 M Ni(II), (d) 0.015 M Co(II) - 0.035 M Ni(II), and (e) 0.050 M Ni(II) in the absence H_2PtCl_6, and (f) 0.050 M Co(II), (g) 0.035 M Co(II) - 0.015 M Ni(II), (h) 0.025 M Co(II) - 0.025 M Ni(II), (i) 0.015 M Co(II) - 0.035 M Ni(II), and (j) 0.050 M Ni(II) in the presence of 0.10 mM H_2PtCl_6.

Table 5.3 Atomic ratio of metal in the wires synthesized by changing the concentration ratio of Co(II) to Ni(II) in the reaction solution.

Concentration ratio of metallic species in the reaction solution [Co(II)] : [Ni(II)]	With or without of H_2PtCl_6	Atomic ratio of metal (atom%) Co	Ni
(a) 100 : 0	–	100.0	0.0
(b) 70 : 30	–	70.5	29.5
(c) 50 : 50	–	50.3	49.7
(d) 30 : 70	–	30.4	69.6
(e) 0 : 100	–	0.0	100.0
(f) 100 : 0	x	100.0	0.0
(g) 70 : 30	x	71.2	28.8
(h) 50 : 50	x	51.4	48.6
(i) 30 : 70	x	29.1	70.9
(j) 0 : 100	x	0.0	100.0

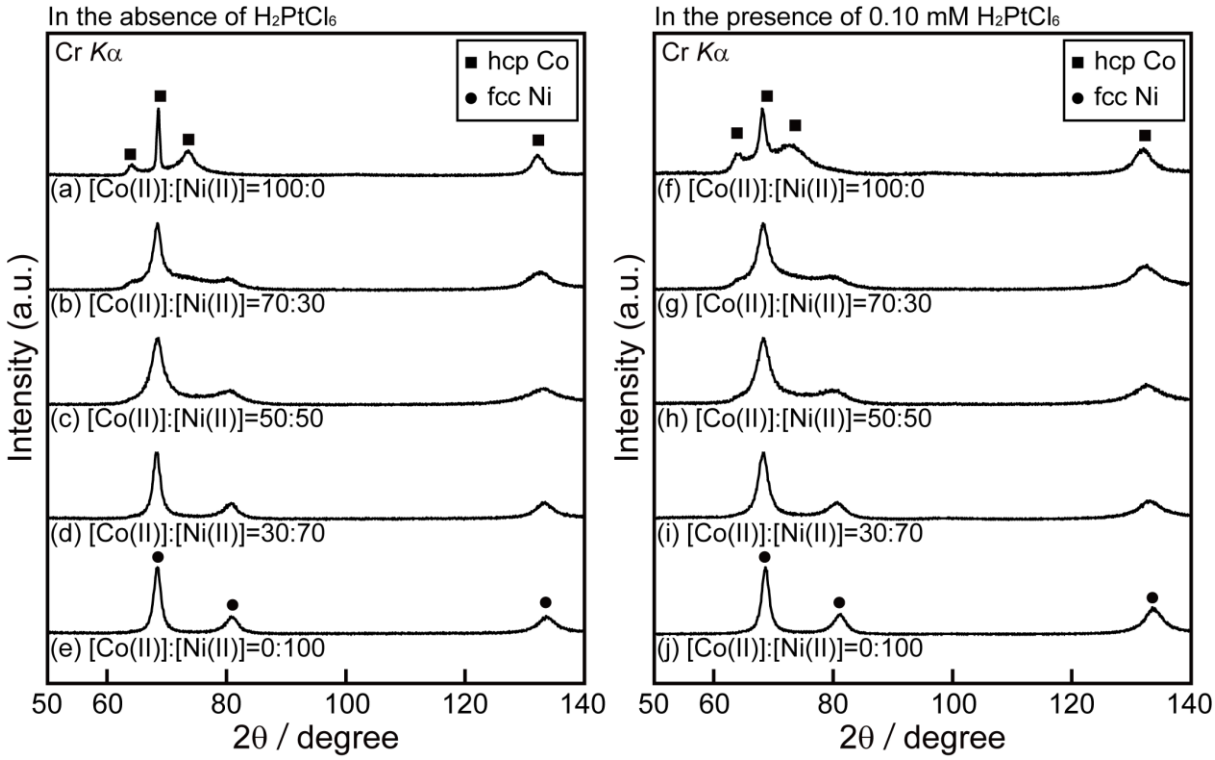

Figure 5.9 XRD patterns of the wires synthesized from the solutions containing (a) 0.050 M Co(II), (b) 0.035 M Co(II) - 0.015 M Ni(II), (c) 0.025 M Co(II) - 0.025 M Ni(II), (d) 0.015 M Co(II) - 0.035 M Ni(II), and (e) 0.050 M Ni(II) in the absence H_2PtCl_6, and (f) 0.050 M Co(II), (g) 0.035 M Co(II) - 0.015 M Ni(II), (h) 0.025 M Co(II) - 0.025 M Ni(II), (i) 0.015 M Co(II) - 0.035 M Ni(II), and (j) 0.050 M Ni(II) in the presence of 0.10 mM H_2PtCl_6.

5.4 Discussion

5.4.1 Formation of Co-Ni nanoparticles via electroless deposition

In the formation process of nanoparticles by electroless deposition, the particle growth proceeds in the simultaneous oxidation reactions of the reducing agent and reduction reactions of metallic ions. Therefore, the polarization curves enable us to evaluate the particle growth rate. In the present process, the following hydrazine oxidation reaction mainly occurs as an anodic reaction;

$$N_2H_4 + 4OH^- \rightarrow N_2 + 4H_2O + 4e \quad [5.1]$$

Figure 5.10 shows anodic polarization curves measured in EG containing 0.2 M NaOH and 0.50 M N_2H_4 using cobalt and nickel substrates as a working electrode. The anodic current due to the oxidation of hydrazine is observed above −0.94 and −0.90 V vs. Ag/AgCl on the cobalt and nickel substrates, respectively. This indicates that excess potential for the hydrazine oxidation is higher on the nickel substrate than on the cobalt substrate. The exchange current density of the hydrazine oxidation reaction is much smaller on the nickel substrate than on the cobalt substrate. Namely, nickel has a lower catalytic activity than cobalt in the oxidation reaction of hydrazine.

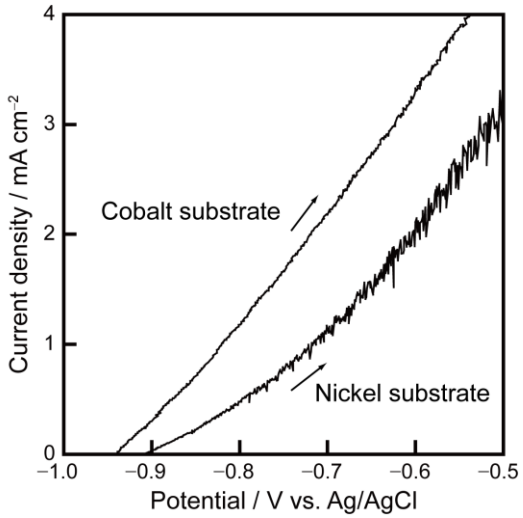

Figure 5.10 Anodic polarization curves measured on cobalt and nickel substrates in EG containing 0.2 M NaOH and 0.50 M N_2H_4. Sweep rate is 1 mV s^{-1}.

Figure 5.11 shows the cyclic voltammograms measured in 120 cm^3 EG containing 0.050 M $CoCl_2$ and 0.2 M NaOH (Fig. 5.11a), and 0.050 M $NiCl_2$ and 0.2 M NaOH (Fig. 5.11b) using the gold-sputtered and nickel-sputtered QCM substrates as a working electrode, respectively. As shown in Fig. 5.11a (dotted line), the cathodic current due to the decomposition of the solvent is observed below about −0.90 V vs. Ag/AgCl during the cathodic sweep. The contribution of this reductive decomposition of the solvent to the total current density is dominant in this process, and the current density due to the cobalt deposition is hardly observed by a normal voltammetry. In a cyclic voltammogram evaluated from the weight change observed by QCM (Fig. 5.11a, solid line), the cathodic current due to the cobalt deposition is observed below about −0.80 V during the cathodic sweep. After the gold-sputtered QCM substrate was completely covered with deposited cobalt, the deposition current of cobalt is observed below −0.77 V during the anodic sweep. The dissolution of cobalt was seen above −0.77 V. Thus, the redox potential of Co(II)/Co can be determined about −0.77 V. Similarly, the redox potential of Ni(II)/Ni is about −0.70 V, which is slightly more positive value than that of Co(II)/Co. The reduction current density of Ni(II) species is much smaller than that of Co(II) species.

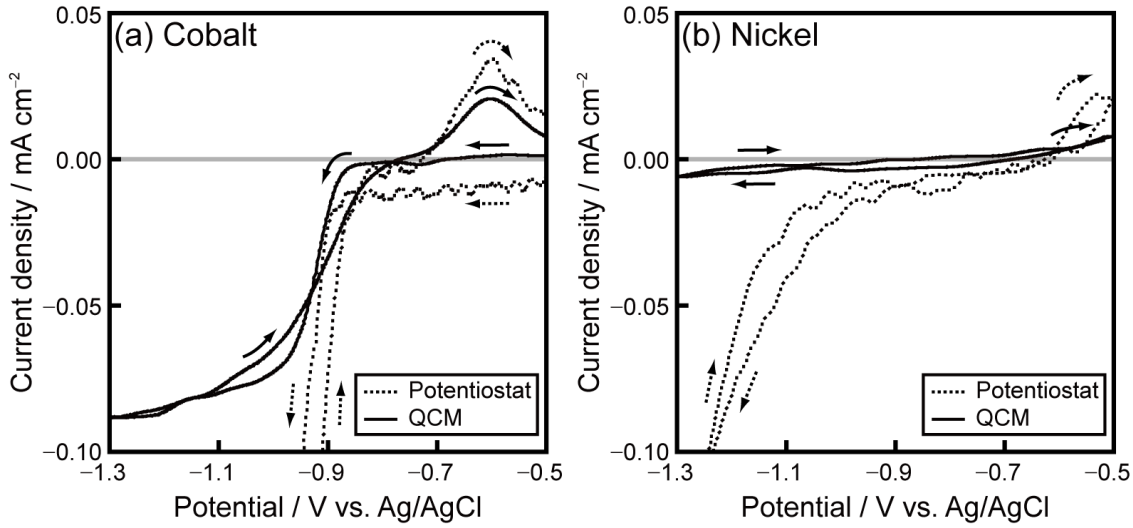

Figure 5.11 Cyclic voltammograms measured by potentiostat (dotted line) and QCM (solid line) at 1 mV s^{-1} in EG containing (a) 0.050 M $CoCl_2$, 0.2 M NaOH, and (b) 0.050 M $NiCl_2$, 0.2 M NaOH.

Consequently, both the anodic current density of hydrazine oxidation and the cathodic current density of metal deposition are smaller on nickel than on cobalt. Thus, it would appear that the growth rate of nickel particles is slower than that of cobalt particles. Once nickel deposits on the surface of particles in the formation process of Co-Ni alloy particles, both the oxidation reaction of hydrazine and the deposition of metal are suppressed. Therefore, nickel has an inhibiting effect on the Co-Ni particle growth and the increase in the concentration of Ni(II) results in the decrease of growth rate of Co-Ni particles.

A small composition gradient in the Co-Ni alloy particles as shown in Fig. 5.2 can be explained by these different electrode behaviors between cobalt and nickel in the reduction reactions of metallic ions and the oxidation reactions of hydrazine. The atomic ratio of cobalt is higher at the core of Co-Ni alloy particles than at the edge because the deposition of cobalt is preferentially occurred in the growth process. According to the Co-Ni alloy phase diagrams, the hcp phase is stable at a higher concentration of cobalt. It is likely that cobalt-rich core of particles mainly has the hcp phase and the edge of particles has the fcc phase. In the result, the mixture of hcp and fcc phases are observed in the XRD patterns of the as-prepared Co-Ni alloy particles and wires in Figs. 5.3b-d and g-i. During the annealing at 623 K for 16 hours, a composition gradient in the Co-Ni alloy particles is reduced by atomic diffusion, which results in the disappearance of the hcp phase and the grain growth of the fcc phase in the particles containing more than 25 atom% Ni.

Figure 5.12 shows the time-dependence of mixed potential during the syntheses of cobalt and nickel particles in the solution containing 0.50 N_2H_4, 0.2 M NaOH, and (a) 0.050 M $CoCl_2$ or (b) 0.050 M $NiCl_2$. The redox potentials of Co(II)/Co and Ni(II)/Ni are also indicated. At 0.050 M $CoCl_2$ (Fig. 5.12a), the mixed potential gradually dropped below the redox potential of Co(II)/Co at about 4 minutes after mixing the metallic salt solution and the

hydrazine solution. This indicates that the cobalt deposition is thermodynamically possible at 4 minutes after the start of the reaction. Actually, the cobalt deposition is observed after 4 minutes by the in-situ QCM measurement as shown in Fig. 5.7a. At 0.050 M $NiCl_2$ (Fig. 5.12b), the mixed potential quickly dropped to around −1.04 V vs. Ag/AgCl just after mixing the reaction solutions.

The difference between the redox potential and the mixed potential corresponds to the driving force of the metal deposition. Thus, the driving force of nickel metal deposition is higher than that of cobalt and the homogeneous nucleation is more favorable during the formation of nickel particles than that of cobalt particles. Furthermore, the growth rate of nickel is suppressed significantly, which results in smaller particles with a sharper size distribution as shown in Figs. 5.1e,j. An inhibiting effect on the Co-Ni particle growth by the addition of Ni(II) becomes stronger with increasing a concentration of Ni(II) and, on the other hand, the nucleation is enhanced by addition of Ni(II). This is the formation mechanism of smaller particles by the addition of Ni(II).

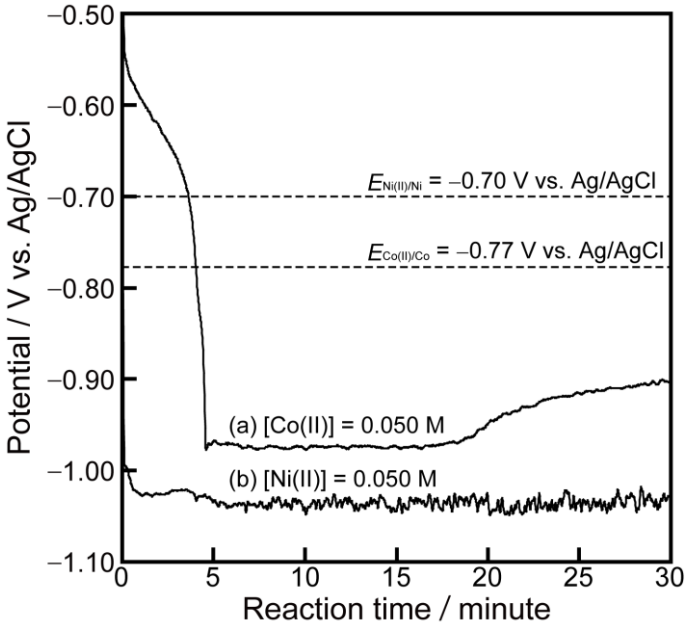

Figure 5.12 Time dependence of mixed potential in the solution containing 0.50 N_2H_4, 0.2 M NaOH, and (a) 0.050 M Co(II) or (b) 0.050 M Ni(II).

5.4.2 Origin of the different electrode behavior in Co and Ni electrodes

In the previous section, we only presented the case of the reaction solution containing 0.20 M NaOH and 0.50 M N_2H_4, however, the nickel alloying effect was also observed in the formation of Co-Ni particles and wires synthesized in the reaction solutions at different concentration of NaOH and N_2H_4. The compositions of reaction solutions for syntheses of Co-Ni particle and wires are summarized in Table 5.4. Figure 5.13 shows the SEM images and size distributions of Co-Ni particles. The atomic ratios and the mean diameters of Co-Ni particles are summarized in Table 5.5 and Figure 5.14, respectively. At each concentration of NaOH, the particle size decreases and the size distribution becomes sharper with an increase in a concentration of Ni(II). Similarly, the Co-Ni wires synthesized in the presence of a magnetic field becomes thinner at a higher concentration of Ni(II) as shown in Figure 5.15.

Table 5.4 Compositions of metallic salt solutions and hydrazine solutions for the synthesis of Co-Ni nanopartcles and nanowires.

	Compositions of metallic salt solutions			Compositions of hydrazine solutions	
	$[CoCl_2]$ (M)	$[NiCl_2]$ (M)	[NaOH] (M)	$[N_2H_4]$ (M)	[NaOH] (M)
(a)	0.100	0.000	1.4	1.00	0.6
(b)	0.070	0.030	1.4	1.00	0.6
(c)	0.050	0.050	1.4	1.00	0.6
(d)	0.030	0.070	1.4	1.00	0.6
(e)	0.000	0.100	1.4	1.00	0.6
(f)	0.100	0.000	4.0	5.00	4.0
(g)	0.070	0.030	4.0	5.00	4.0
(h)	0.050	0.050	4.0	5.00	4.0
(i)	0.030	0.070	4.0	5.00	4.0
(j)	0.000	0.100	4.0	5.00	4.0

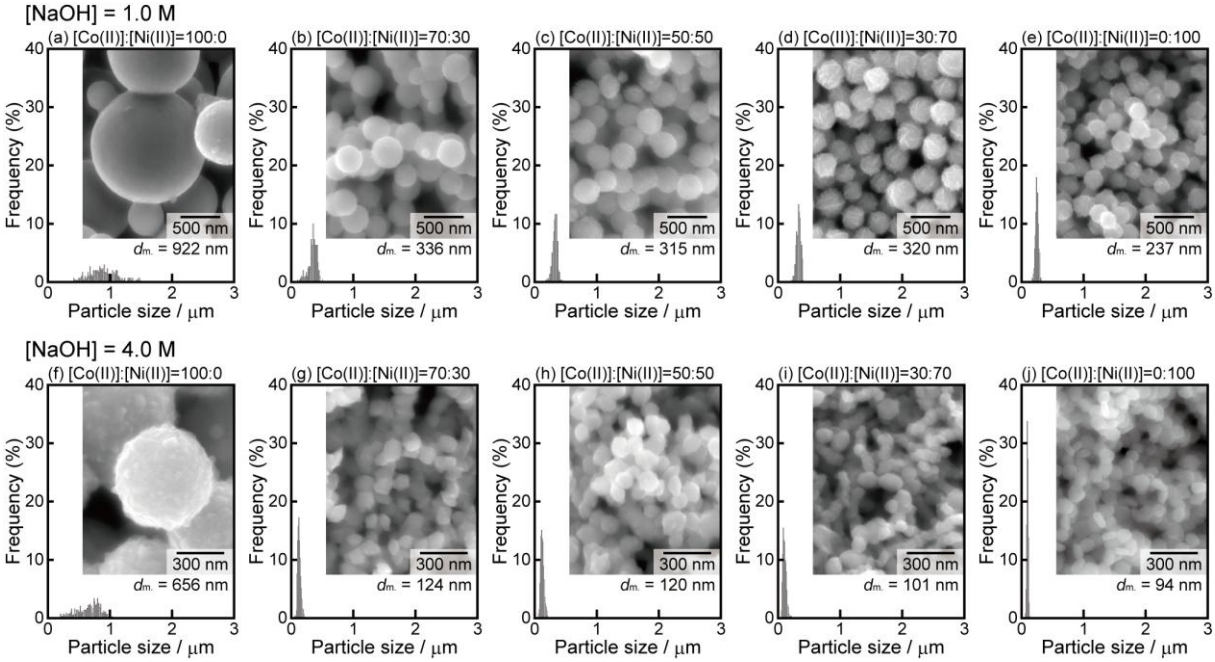

Figure 5.13 SEM images and size distribution of the particles synthesized from the solutions containing (a) 0.050 M Co(II), (b) 0.035 M Co(II) - 0.015 M Ni(II), (c) 0.025 M Co(II) - 0.025 M Ni(II), (d) 0.015 M Co(II) - 0.035 M Ni(II), and (e) 0.050 M Ni(II) at 1.0 M NaOH, and (f) 0.050 M Co(II), (g) 0.035 M Co(II) - 0.015 M Ni(II), (h) 0.025 M Co(II) - 0.025 M Ni(II), (i) 0.015 M Co(II) - 0.035 M Ni(II), and (j) 0.050 M Ni(II) at 4.0 M NaOH. Mean diameter $d_{m.}$ is also indicated.

Table 5.5 Atomic ratio of metal in the particles synthesized by changing the concentration ratio of Co(II) to Ni(II) in the reaction solution.

Concentration ratio of metallic species in the reaction solution [Co(II)] : [Ni(II)]	Concentration of NaOH (M) [NaOH]	Atomic ratio of metal (atom%) Co	Ni
(a) 100 : 0	1.0	100.0	0.0
(b) 70 : 30	1.0	69.3	30.7
(c) 50 : 50	1.0	49.5	50.5
(d) 30 : 70	1.0	29.9	70.1
(e) 0 : 100	1.0	0.0	100.0
(f) 100 : 0	4.0	100.0	0.0
(g) 70 : 30	4.0	70.3	29.7
(h) 50 : 50	4.0	50.2	49.8
(i) 30 : 70	4.0	29.7	70.3
(j) 0 : 100	4.0	0.0	100.0

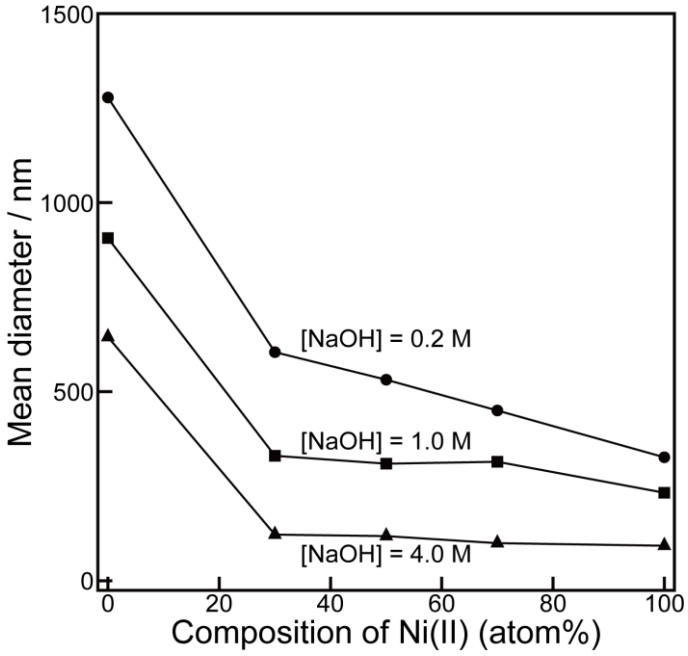

Figure 5.14 Change in mean diameter of Co-Ni particles synthesized at 0.2, 1.0, and 4.0 M NaOH.

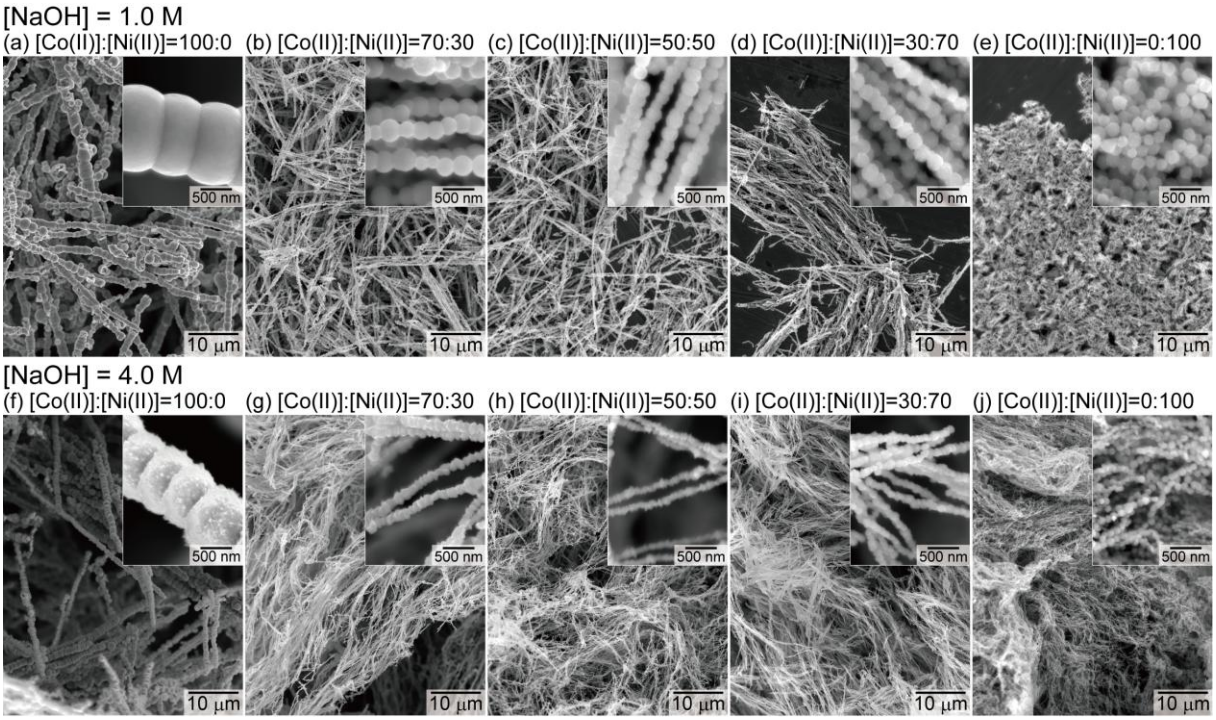

Figure 5.15 SEM images of the wires synthesized from the solutions containing (a) 0.050 M Co(II), (b) 0.035 M Co(II) - 0.015 M Ni(II), (c) 0.025 M Co(II) - 0.025 M Ni(II), (d) 0.015 M Co(II) - 0.035 M Ni(II), and (e) 0.050 M Ni(II) at 1.0 M NaOH, and (f) 0.050 M Co(II), (g) 0.035 M Co(II) - 0.015 M Ni(II), (h) 0.025 M Co(II) - 0.025 M Ni(II), (i) 0.015 M Co(II) - 0.035 M Ni(II), and (j) 0.050 M Ni(II) at 4.0 M NaOH.

Table 5.6 Atomic ratio of metal in the wires synthesized by changing the concentration ratio of Co(II) to Ni(II) in the reaction solution.

Concentration ratio of metallic species in the reaction solution [Co(II)] : [Ni(II)]	Concentration of NaOH (M) [NaOH]	Atomic ratio of metal (atom%) Co	Ni
(a) 100 : 0	1.0	100.0	0.0
(b) 70 : 30	1.0	69.5	30.5
(c) 50 : 50	1.0	50.4	49.6
(d) 30 : 70	1.0	31.2	68.8
(e) 0 : 100	1.0	0.0	100.0
(f) 100 : 0	4.0	100.0	0.0
(g) 70 : 30	4.0	71.2	28.8
(h) 50 : 50	4.0	52.3	47.7
(i) 30 : 70	4.0	30.6	69.4
(j) 0 : 100	4.0	0.0	100.0

Figure 5.16 shows the XRD patterns of Co-Ni particles of (a) to (j) in Figure 5.13. For the particles synthesized at [Co(II)]:[Ni(II)]=50:50 and 30:70, a mixture of the hcp and fcc phase is observed in each concentration of NaOH, which is not consistent with the Co-Ni phase diagram. It would appear that the hcp phase results from a small composition gradient, as discussed above. These nickel alloying effects have been explained by the different electrode behaviors of cobalt and nickel in the oxidation reaction of hydrazine and the reduction reaction of metallic ions. Thus, it is important to evaluate the electrode reaction on the metals in order to understand the formation mechanism of the nanoparticles and nanowires by electroless deposoition.

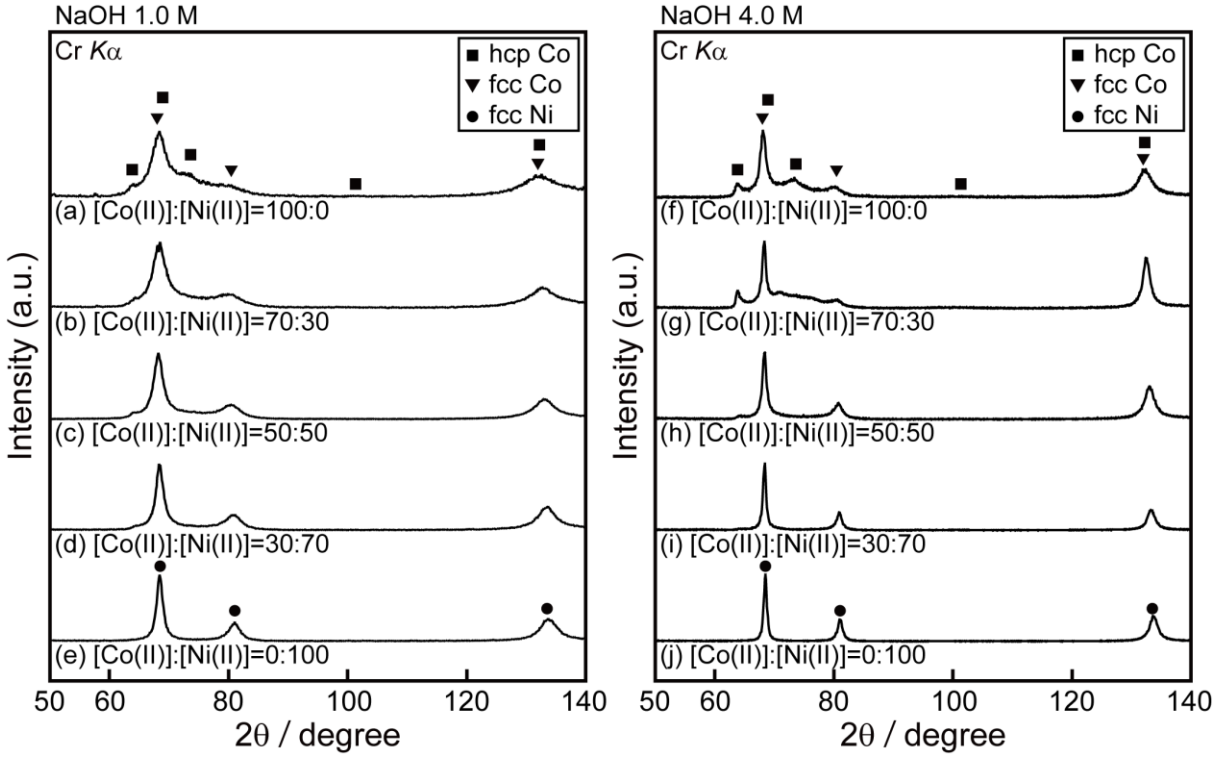

Figure 5.16 XRD patterns of the particles synthesized from the solutions containing (a) 0.050 M Co(II), (b) 0.035 M Co(II) - 0.015 M Ni(II), (c) 0.025 M Co(II) - 0.025 M Ni(II), (d) 0.015 M Co(II) - 0.035 M Ni(II), and (e) 0.050 M Ni(II) at 1.0 M NaOH, and (f) 0.050 M Co(II), (g) 0.035 M Co(II) - 0.015 M Ni(II), (h) 0.025 M Co(II) - 0.025 M Ni(II), (i) 0.015 M Co(II) - 0.035 M Ni(II), and (j) 0.050 M Ni(II) at 4.0 M NaOH.

The catalytic activities of the metals for the anodic oxidation of hydrazine have been evaluated in various reports.[10-12] It was experimentally demonstrated that nickel has a lower catalytic activity than cobalt in the oxidation reaction of hydrazine.[10-12] Figure 5.17 shows anodic polarization curves measured in EG containing 0.50 M N_2H_4 using cobalt and nickel substrates as a working electrode. Actually, the exchange current density of the hydrazine oxidation reaction is much smaller on the nickel substrate than on the cobalt substrate at each concentration of NaOH. Since there are various intermediates in the hydrazine oxidation reaction,[13] it is difficult to detect the reaction mechanism by experimental approaches. Recently, the oxidation mechanisms of the reducing agent have been analyzed using

theoretical calculations,[13,14] such as *ab initio* molecular orbital calculation, however, the oxidation mechanism of hydrazine on the cobalt and nickel surface has not been investigated by computational method. Therefore, the origin of the different catalytic activities between cobalt and nickel has not been resolved fundamentally, and it must be concluded that the oxidation reaction of hydrazine is intrinsically slower on nickel surface than on cobalt surface.

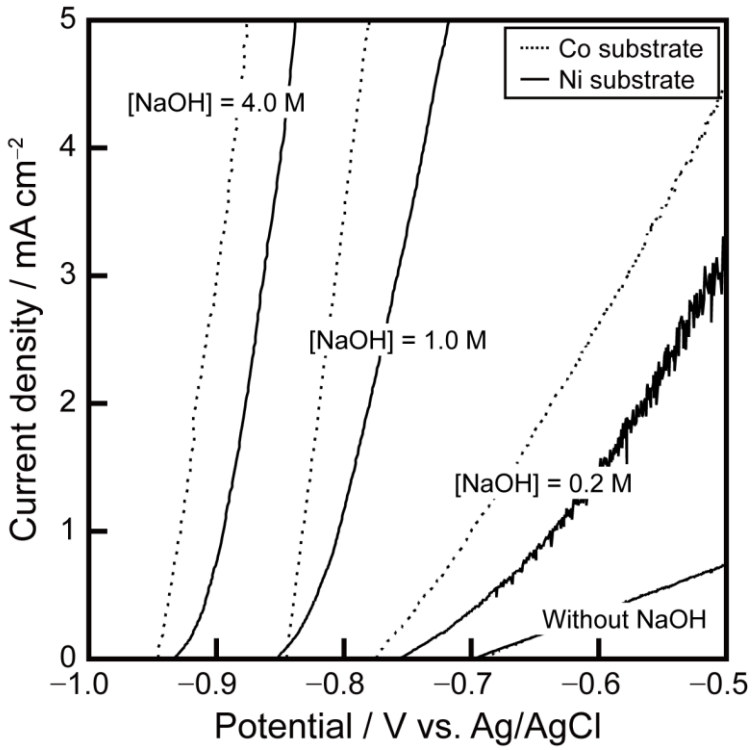

Figure 5.17 Anodic polarization curves measured on cobalt and nickel substrates in EG containing 0.50 M N_2H_4 at various concentrations of NaOH. Sweep rate is 1 mV s^{-1}. The supporting electrolyte, 0.1 M $LiClO_4$, was added in the solutions without NaOH. During the measurement, the temperature of the solutions was kept at a reaction temperature of 353 K on a hot plate with nitrogen gas bubbling to remove the dissolved oxygen.

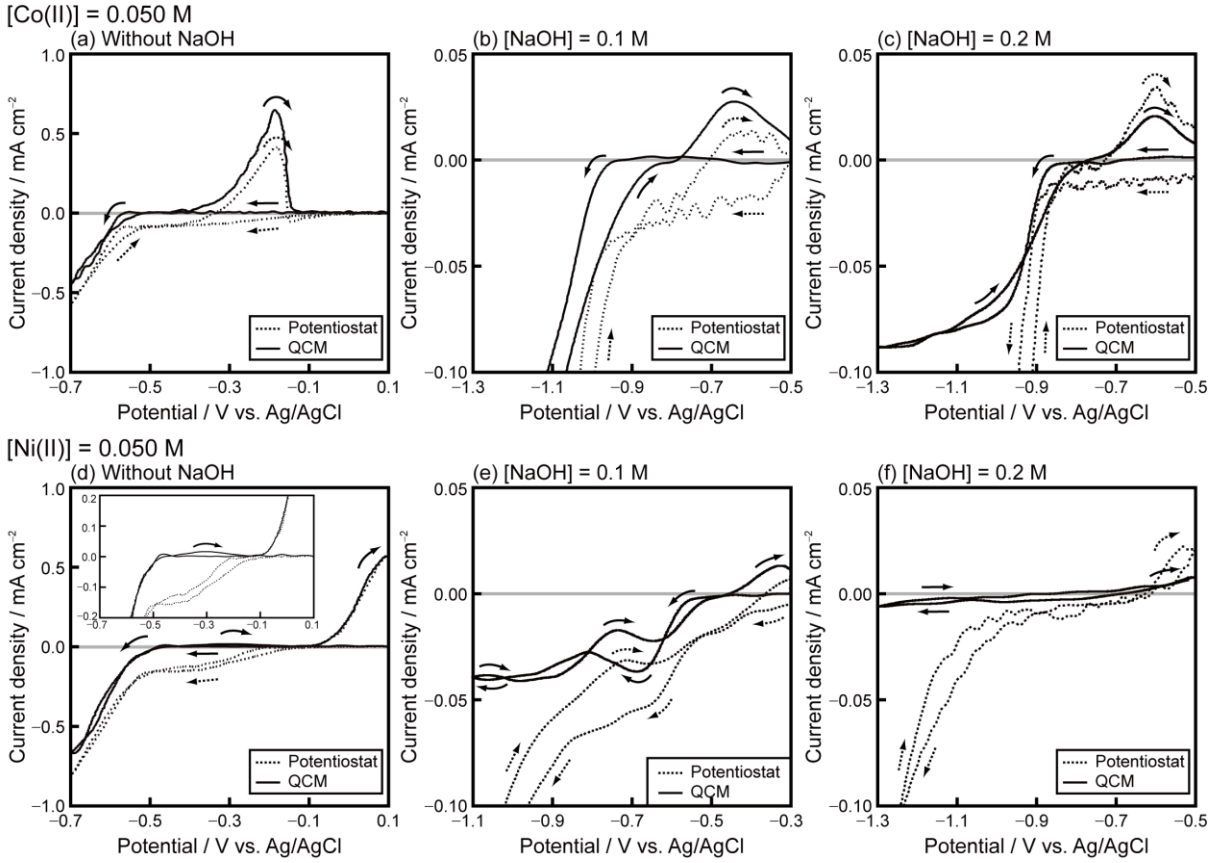

Figure 5.18 Cyclic voltammograms measured by potentiostat (dotted line) and QCM (solid line) at 1 mV s^{-1} in EG containing (a) 0.050 M $CoCl_2$, (b) 0.050 M $CoCl_2$, 0.1 M NaOH, (c) 0.050 M $CoCl_2$, 0.2 M NaOH and (d) 0.050 M $NiCl_2$, (e) 0.050 M $CoCl_2$, 0.1 M NaOH, (f) 0.050 M $CoCl_2$, 0.2 M NaOH. The supporting electrolyte, 0.1 M $LiClO_4$, was added in the solutions (a) and (d).

As shown in Fig. 5.11, it should be noted that the reduction reaction of Ni(II) is much slower than that of Co(II) because the nickel is thermodynamically more noble than cobalt. Figure 5.18 shows that cyclic voltammograms measured in 120 cm^3 EG containing 0.050 M $CoCl_2$ and 0.050 M $NiCl_2$ at various concentrations of NaOH. In the absence of NaOH (Figs. 5.18 a,d), the cobalt and nickel deposition is observed below −0.50 V and −0.45 V vs. Ag/AgCl. The reduction current of cobalt deposition is smaller than that of nickel deposition in the absence of NaOH, which is opposite result in the presence of NaOH. The addition of NaOH strongly affects the deposition behavior of cobalt and nickel in EG solution. The redox potentials of cobalt and nickel shift to the negative value and the reduction currents

of cobalt and nickel deposition become smaller at a higher concentration of NaOH. The decrease in the reduction current of metal deposition by addition of NaOH is more noticeable in nickel system than in cobalt system.

Figure 5.19 shows the mass concentrations of cobalt and nickel evaluated by inductively-coupled plasma mass spectrometry (ICP-MS) in the supernatant EG solution containing 0.050 M $CoCl_2$ and 0.050 M $NiCl_2$ at various concentrations of NaOH. The photos of the solutions are also indicated. For ICP-MS, the supernatant of EG solution were separated from the precipitates by the centrifugation for 1 hour. The EG solutions without NaOH are transparent as shown in Figs. 5.19a,d. By addition of NaOH, the Ni(II) ions in EG solutions were hydroxylated to form green nickel hydroxide and/or nickel alkoxide sol, which slowly precipitate at the bottom (see Figs. 5.19e and f). The mass concentration of nickel in the supernatant EG solution decreases with an increase in the concentration of NaOH. By contrast, the precipitates were hardly observed in EG solution containing Co(II) and 0.1 M NaOH (Fig. 5.19b). The little green Co(II) hydroxide sol was formed at 0.2 M NaOH. The mass concentration of cobalt is higher than that of nickel at each concentration of NaOH. It is likely that the difference in the stability of Co(II) and Ni(II) ions with OH^- is related to the different deposition behavior of cobalt and nickel as shown in Fig. 5.18. Namely, the reduction current of Ni(II) ions were much smaller than that of Co(II) because a lot of Ni(II) ions are stabilized by the addition of NaOH, which results in the lower growth rate of nickel in the formation of Co-Ni particles. Consequently, the origin of the different deposition behavior between cobalt and nickel is the difference in the stability of Co(II) and Ni(II) ions with OH^- in EG solution. The stability of metallic ions with OH^- is the key factor to control the activity of metallic ions and the deposition rate of the metallic nanoparticles.

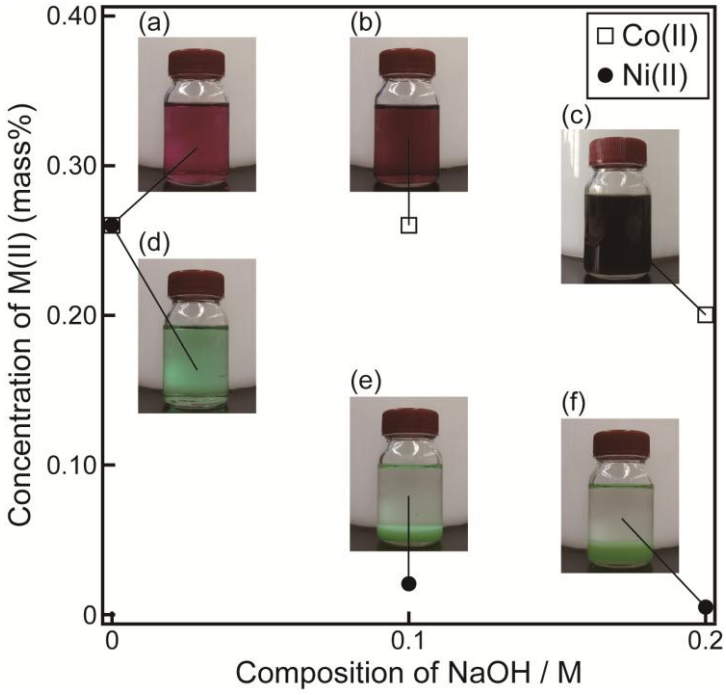

Figure 5.19 Mass concentration of cobalt and nickel evaluated by ICP in the supernatant EG solution containing (a) 0.050 M $CoCl_2$, (b) 0.050 M $CoCl_2$, 0.1 M NaOH, (c) 0.050 M $CoCl_2$, 0.2 M NaOH and (d) 0.050 M $NiCl_2$, (e) 0.050 M $NiCl_2$, 0.1 M NaOH, (f) 0.050 M $NiCl_2$, 0.2 M NaOH. The photos of the solutions are also indicated.

5.4.3 Formation of Co-Ni nanowires under a magnetic field

In the previous chapter, we discussed the following formation mechanism of nanowires via electroless deposition under a magnetic field. First, particles are formed in the reaction solution, and are aligned along a magnetic field due to the magnetic interaction among the particles. Then, the necks between particles are preferentially covered with deposited metal to decrease the interfacial energy. Finally, the particles are tightly connected and form rigid wires. Therefore, the necessary condition for the formation of wires is that the alignment of particles occurs prior to the terminal point of the deposition reaction. According to this mechanism, the magnetic interaction and the deposition rate of particles strongly affect the formation of wires. Namely, the formation of wires becomes easier at a

stronger magnetic interaction and a slower deposition rate of particles.

Figures 5.20 shows the magnetization-magnetic field (M-H) curves for the particles synthesized by changing the concentration ratio of Co(II) to Ni(II) in solution without H_2PtCl_6. The hysteresis is observed in each curve and it would appear that the particles behave as magnetic multidomain particles.[15] The magnetic properties of the particles are summarized in Table 5.7. The saturation magnetization of cobalt and nickel particles is 145.5 and 47.5 emu g^{-1} which is lower than that of the bulk metal (161 and 54 emu g^{-1} at 293 K, respectively).[16] The saturation magnetization of Co-Ni alloy particles decreases with increasing a concentration ratio of Ni(II). The decrease of the observed saturation magnetization of cobalt and nickel particles with respect to the bulk values is possibly due to the impurities such as carbon, oxygen, and hydrogen.[15,17] Actually, the mass losses about 2 % were observed in cobalt particles (Fig. 5.1a) after the thermal treatment at 623 K in H_2 atmosphere for 16 hours, indicating that the particles contain the organic species, organometallic phases or unreacted hydroxides which are thermally unstable.

At 1.0 - 2.0 kOe, which corresponds to the magnetic field in the syntheses of wires, the magnetization of nickel particles is much lower than that of cobalt and Co-Ni alloy particles as shown in the inset of Fig. 5.20. In the formation of cobalt wires, it takes less time for the particles to align along a magnetic field due to the stronger magnetic interaction between cobalt particles. Thus, the particles align prior to the end of the reduction reaction and the relatively-smooth wires were formed as shown in Figs. 5.8a,f despite the higher growth rate of particles. On the contrary, the weak magnetic interaction between nickel particles results in the formation of beads-like wires as shown in Fig. 5.8 while the growth rate of nickel particles is lower than that of cobalt. In order to fabricate the nickel wires with a smooth surface, it is necessary to decrease the deposition rate of nickel particles, which is

achieved by adjusting a concentration of NaOH and adding a complexing agent such as trisodium citrate dihydrate ($Na_3C_6H_5O_7 \cdot 2H_2O$).[1] Consequently, by carefully controlling both the deposition rate and the magnetization of the particles, one can successfully prepare nanowires with various diameter and surface morphology.

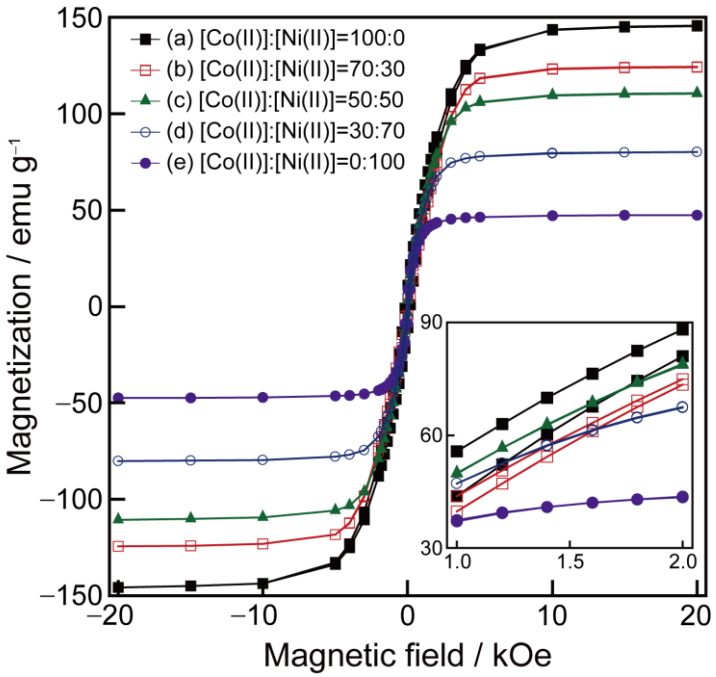

Figure 5.20 The magnetization-magnetic field (M-H) curves obtained at room temperature for the particles synthesized from the solutions containing (a) 0.050 M Co(II), (b) 0.035 M Co(II) - 0.015 M Ni(II), (c) 0.025 M Co(II) - 0.025 M Ni(II), (d) 0.015 M Co(II) - 0.035 M Ni(II), (e) 0.050 M Ni(II) in the absence of H_2PtCl_6.

Table 5.7 Magnetic properties of particles synthesized by changing the concentration ratio of Co(II) and Ni(II) in the reaction solution.

Concentration ratio of metallic species in the reaction solution [Co(II)] : [Ni(II)]	Saturation magnetization, M_s (emu g^{-1})	Coercivity, H_c (Oe)
(a) 100 : 0	145.5	186
(b) 70 : 30	124.1	92
(c) 50 : 50	110.3	41
(d) 30 : 70	80.1	61
(e) 0 : 100	47.5	102

5.5 Conclusion

In the present work, the formation of Co-Ni particles and wires via electroless deposition was electrochemically investigated. Through the present experiments, we have obtained the following results.

1. The current density in both the oxidation reactions of hydrazine and the reduction reactions of metallic ions is much smaller on nickel than that on cobalt, indicating that the growth rate of nickel particles is lower than cobalt.
2. Deposited nickel suppresses the growth rate of Co-Ni particles, namely, nickel works as an inhibitor of the growth of Co-Ni particles. An inhibiting effect on the Co-Ni particle growth by the addition of Ni(II) becomes stronger with increasing a concentration of Ni(II) and the nucleation is prompted in comparison. This is the formation mechanism of smaller particles and thinner wires by the addition of Ni(II).
3. The difference in the deposition rate of cobalt and nickel results in a small composition gradient observed in Co-Ni alloys, which affects the crystal structure of Co-Ni alloy particles and wires.
4. The different deposition behavior between cobalt and nickel results from the difference in the stability of Co(II) and Ni(II) ions with OH^- in EG solution.
5. The magnetization of particles as well as the deposition rate strongly affects the morphology of wires formed under a magnetic field. For example, a lower deposition rate is required in fabrication of smooth wires whose magnetization is relatively weak, such as nickel.

References

1. M. Kawamori, S. Yagi, and E. Matsubara, *J. Electrochem. Soc*., **158**, E79 (2011).

2. C. D. Iacovangelo and K. P. Zarnoch, *J. Electrochem. Soc.*, **138**, 976 (1991).
3. S. S. Djokic, *J. Electrochem. Soc*., **144**, 2358 (1997).
4. G. Stremsdoerfer, H. Perrot, J. R. Martin, and P. Cléchet, *J. Electrochem. Soc*., **135**, 2881 (1988).
5. G. Viau, P. Toneguzzo, A. Pierrard, O. Acher, F. Fiévet-Vincent, and F. Fiévet, *Scr. Mater.*, **44**, 2263 (2001).
6. M. D. L. Balela, S. Yagi, Z. Lockman, A. Aziz, A. Jr. Amorsolo, and E. Matsubara, *J. Electrochem. Soc*., **156**, E139 (2009).
7. M. Pourbaix: *Atlas of Electrochemical Equilibria in Aqueous Solutions*, p. 322, Cebelcor, Brüssel (1966).
8. T. Nishizawa and K. Ishida, *Bull. Alloy Phase Diagram*, **4**, 390 (1983).
9. P. Villars and L.D. Calvert, *Pearson's Handbook of Crystallographic Data for Intermetallic Phases*, American Society of Metals, Materials Park, Ohio, (1985).
10. I. Ohno, O. Wakabayashi, and S. Haruyama, *J. Electrochem. Soc*., **132**, 2323 (1985).
11. K. Asazawa, T. Sakamoto, S. Yamaguchi, K. Yamada, H. Fujikawa, H. Tanaka, and K。Oguro, *J. Electrochem. Soc*., **156**, B509 (2009).
12. S. K. Singh, X.-B. Zhang, and Q. Xu, *J. Am. Chem. Soc.*, **131**, 9894 (2009).
13. T. Shimada, A. Tamaki, H. Nakai, and T. Homma, *Electrochemistry*, **75**, 45 (2007).
14. A. Kaczmarek, M. Shiga, and D. Marx, *J. Phys. Chem. A*, **113**, 1985 (2009).
15. C. Luna, M. Morales, C. J. Serna, and M. Vazquez, *Nanotechnology*, **14**, 268 (2003).
16. B. D. Cullity and C. D. Graham, *Introduction to Magnetic Materials, Second Edition*, p. 531, The Institute of Electrical and Electronics Enginners, Inc. (2009).
17. G. Viau, F. Fiévet-Vincent, and F. Fiévet, *J. Mater. Chem.*, **6**, 1047 (1996).

Chapter 6

Iron Alloying Effect on Formation of Cobalt Nanoparticles and Nanowires

6.1 Introduction

In the previous chapter, taking Co-Ni system as an example, we have experimentally demonstrated that the formation of nanoparticles and nanowires is strongly affected by the electrode behavior of metal in the reduction reaction of metallic ions and the oxidation reaction of reducing agents.[1] The formation process of iron-based particles is more complex compared to that of Co-Ni particles owing to the presence of trivalent iron ions, Fe(III). In the potential window of both aqueous solutions and EG solutions, the divalent species are more stable than the trivalent species for cobalt and nickel systems, in contrast, the trivalent species are stable as well as divalent species for iron system.[2] Although there have been various reports attempting the synthesis of iron and Fe-Co alloy particles by liquid phase reduction using polyol process and hydrazine reduction, there are several theories as to the formation mechanism of iron nanoparticles.[3-7] For example, Jeyadevan *et al.* reported that the formation of iron particles in EG solution is due to the polyol reduction,[5,6] on the other hand, Viau *et al.* proposed the disproportionation reaction of Fe(II) to Fe(III) and iron particles (as discussed later in detail).[7] The formation mechanism of iron particles remains controversial, as a reason for this, there has been little discussion from the viewpoint of electrochemistry.

In the present chapter, we applied the electrochemical in-situ measurements to the synthesis process of particles in Fe-Co system. First, the formation mechanism of iron

particles in EG solution was investigated by using an in-situ mixed potential measurement and the cyclic voltammetry combined with the QCM measurement. Then, the iron alloying effect of cobalt nanoparticles and nanowires was discussed based on the electrochemical measurements. The comparison between nickel and iron alloying effect on formation of cobalt nanoparticles and nanowires provide us the concept to design metallic nanowires with desired morphologies, composition ratios, and crystal structures.

6.2 Experimental

The reaction solutions were prepared using cobalt chloride hexahydrate ($CoCl_2 \cdot 6H_2O$) and iron chloride tetrahydrate ($FeCl_2 \cdot 4H_2O$) as a source of iron and cobalt ions, ethylene glycol (EG) as a solvent, and hydrazine monohydrate ($N_2H_4 \cdot H_2O$) as a reducing agent. Sodium hydroxide (NaOH) was used as a source of OH^- ions. Chloroplatinic acid hexahydrate ($H_2PtCl_6 \cdot 6H_2O$) was used as a nucleating agent. These reagents are all reagent-grade (Nacalai Tesque, Inc.) and used without further purification.

First, $CoCl_2 \cdot 6H_2O$ and $FeCl_2 \cdot 4H_2O$ were completely dissolved in EG with argon gas bubbling to remove the dissolved oxygen. After that, NaOH pellet was dissolved for 4 hours at 353 K and 40 cm^3 EG solution containing 0.10 M metallic salts ($[CoCl_2] + [FeCl_2] = 0.10$ M) and 4.0 M NaOH was prepared, where M is mol dm^{-3}. For the experiments with a nucleating agent, 2.0 mM H_2PtCl_6 was added. The same amount of EG solution (40 cm^3) containing 5.00 M N_2H_4 and 4.0 M NaOH was also prepared. The temperature of the solutions was kept at 353 K with argon gas bubbling to remove the dissolved oxygen. The metallic salt solution and the hydrazine solution were mixed at 353 K to start the reaction. The reaction solution was agitated at a rate of 500 rpm with a magnetic stirring unit at 353 K

during the reaction for the syntheses of Fe-Co particles. For the syntheses of Fe-Co wires, the reaction solution was kept at 353 K in a water bath located inside the two parallel neodymium magnets (100 x 100 mm) separated 100 mm apart. After the reaction for 3 hours, the synthesized particles and wires were magnetically separated from the solution and washed several times with ethanol.

The morphology of precipitates was observed using a field-emission-scanning electron microscope (JEOL Ltd., JSM-6500F). The mean diameter and size distribution of the Fe-Co particles were determined by image analysis for randomly selected 300 particles in each sample. The compositions of Fe-Co particles and wires were analyzed with energy-dispersive X-ray (EDX) spectrometry. The crystalline structure of precipitates was investigated by X-ray diffraction (XRD, Rigaku Co., Ltd., RINT-2200) using Cr *K*α radiation. The degree of order in Fe-Co alloy particles was evaluated by Synchrotron XRD at the BL28XU beamline of the SPring-8.

During the syntheses of Fe-Co particles, cobalt or iron substrate was immersed in the reaction solution and a mixed potential was measured by a potentiostat/galvanostat (Hokuto Denko Co., Ltd., HA-151) using a Ag/AgCl (3.33 M KCl) electrode (Horiba 2565A-10T) as a reference electrode. Additionally, the gold-sputtered QCM electrode (SEIKO EG&G QA-A9M-AU) was immersed in the reaction solution. The weight of deposits on the QCM electrode, Δm, was calculated from the change in resonance frequency of the QCM electrode, Δf, by Sauerbrey's equation.

The cyclic voltammograms were also measured by the potentiostat/galvanostat using a gold-sputtered QCM electrode as a working electrode, a platinum electrode (20 x 20 mm) as a counter electrode, and a Ag/AgCl electrode as a reference electrode.

6.3 Results

6.3.1 Characterization of Fe-Co particles formed in the metallic salt solution

Before mixing with hydrazine solution, the Fe-Co particles were formed in the metallic salt solutions containing Fe(II), while the formation of Co particles were not observed in 100% Co(II) solution. Figure 6.1 shows scanning electron microscopy (SEM) images and particle size distributions of Fe-Co particles synthesized in the different concentration ratios of Co(II) to Fe(II) in the reaction solutions. The mean diameter of particles is also indicated. The relatively-spherical particles were obtained at [Co(II)]:[Fe(II)]=70:30, and the surface asperity of particles becomes more noticeable at a higher concentration of Fe(II). The cubic iron particles were formed in solution of [Co(II)]:[Fe(II)]= 0:100. Table I shows the atomic ratios and yields of Fe-Co particles, which are evaluated with EDX and the mass calculation of the particles, respectively. It is noted that the atomic ratios of iron to cobalt in the particles are higher than the concentration ratios of Fe(II) to Co(II) ions in solution. This result is anomalous since cobalt is more noble metal compared to iron, and it is expected that the reduction of cobalt is easier than that of iron. This anomalous deposition of Fe-Co alloy particles is discussed later in detail. In each concentration ratio, the yields of metal are low below 10%.

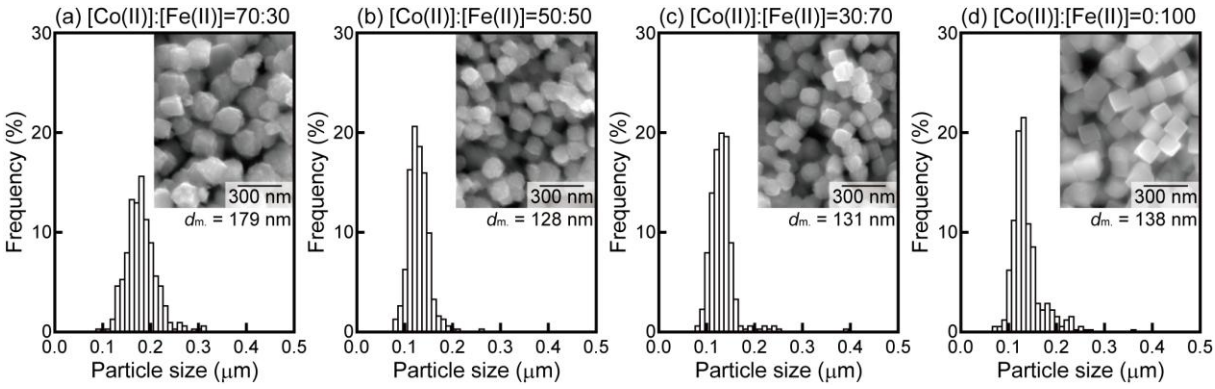

Figure 6.1 SEM images and size distribution of the particles synthesized from the solutions containing (a) 0.070 M Co(II) - 0.030 M Fe(II), (b) 0.050 M Co(II) - 0.050 M Fe(II), (c) 0.030 M Co(II) - 0.070 M Fe(II), and (d) 0.100 M Fe(II). Mean diameter $d_{m.}$ is also indicated.

Table 6.1 Atomic ratio and yields of the particles synthesized changing the concentration ratio of Co(II) to Fe(II) in the reaction solution.

Concentration ratio of metallic species in the reaction solution	Atomic ratio of metal (atom%)		Yield of metal (%)		
[Co(II)] : [Fe(II)]	Co	Fe	Total	Co	Fe
(a) 100 : 0	–	–	0.0	0.0	–
(b) 70 : 30	57.8	42.2	6.2	5.1	8.7
(c) 50 : 50	32.8	67.2	8.4	5.5	11.4
(d) 30 : 70	19.3	80.7	7.6	4.9	8.8
(e) 0 : 100	0.0	100.0	5.5	–	5.5

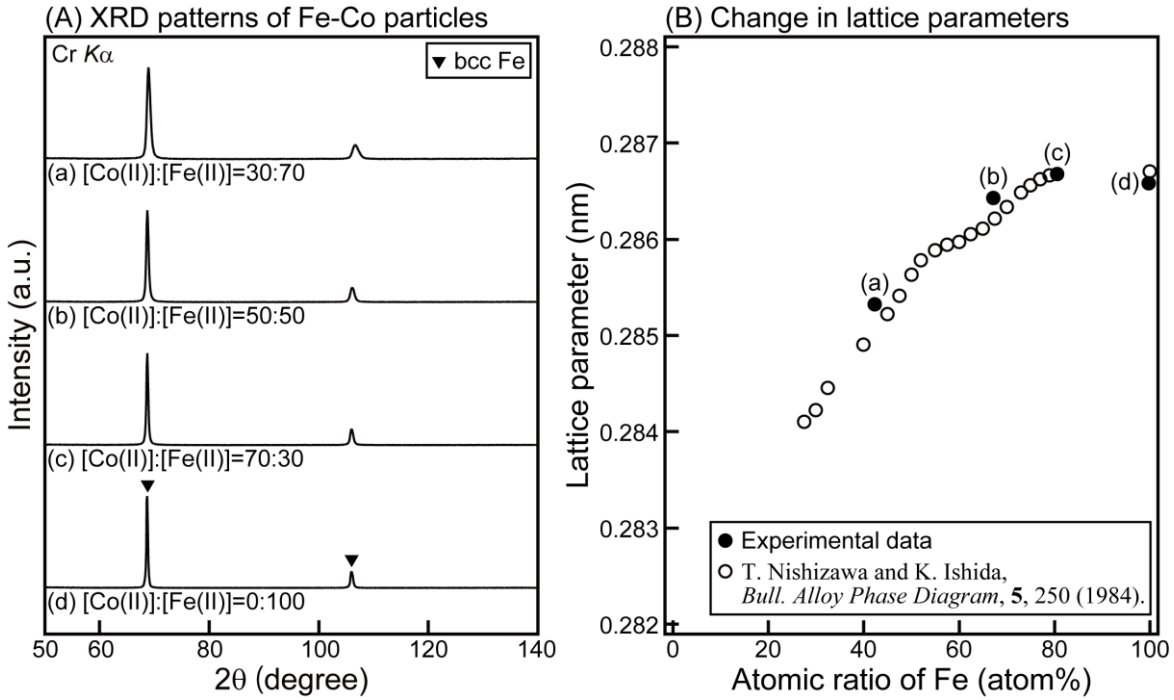

Figure 6.2 (A) XRD patterns and (B) change in lattice parameters of the particles synthesized from the solutions containing (a) 0.070 M Co(II) - 0.030 M Fe(II), (b) 0.050 M Co(II) - 0.050 M Fe(II), (c) 0.030 M Co(II) - 0.070 M Fe(II), and (d) 0.100 M Fe(II).

Figure 6.2A shows XRD patterns of the particles. The body-centered cubic (bcc) peaks are observed in each pattern, which is consistent with the phase expected in the phase diagram as shown in Fig. 6.3.[8] The peak position shifts to lower angle and the peak width becomes sharper at a higher concentration of Fe(II). As shown in Fig. 6.2B, the lattice parameters change according to the literature data,[9] indicating that the Fe-Co solid solutions were formed.

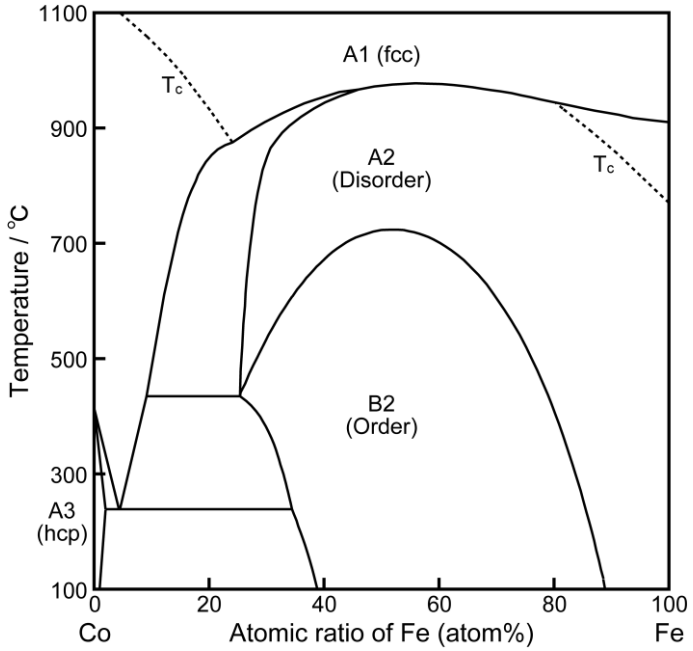

Figure 6.3 Calculated phase diagram of the Fe-Co binary system.[8]

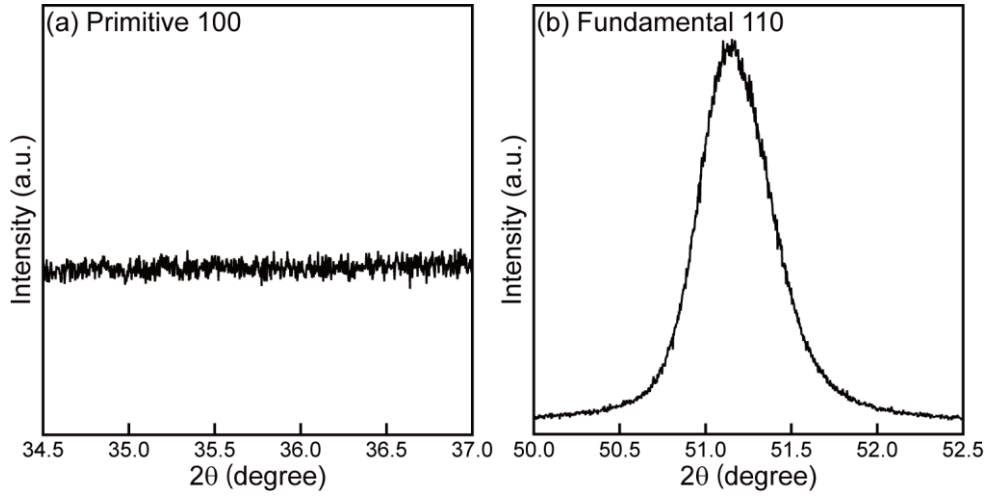

Figure 6.4 Synchrotron XRD patterns of the $Fe_{42}Co_{58}$ particles synthesized from the solutions containing 0.070 M Co(II) - 0.030 M Fe(II) for selected regions; (a) primitive 100 and (b) fundamental 110 reflections. The X-ray wavelength was chosen to be 1.7434 Å near the Fe K edge.

Fe-Co alloys exhibit the α(A2)/ α'(B2) order-disorder transformation at about 1000 K around 50 atom% Fe.[8] The order-disorder transformation of Fe-Co alloys has been extensively investigated because of its practical importance especially in magnetic materials.[10,11] A superlattice diffraction peak is useful to evaluate the degree of ordering,

however, it is hardly detected by conventional XRD measurements because of the very similar values of atomic scattering factors f_{Co} and f_{Fe}. The diffraction peak intensities of the superlattice peak lines, which is proportional to the square of structure factor $|F|^2 = (f_{Co} - f_{Fe})^2$, will be very small even if they were perfectly ordered. However, the superlattice lines can be detected with high enough intensity to analyze quantitatively by application of the anomalous X-ray dispersion phenomenon.[12] Thus, the anomalous synchrotron XRD was conducted at the selected wavelength of 1.7434 Å near Fe *K* edge using a Si(111) channel-cut monochromator. Figure 6.4 shows the synchrotron XRD profiles of $Fe_{42}Co_{58}$ particles (Fig. 1d) for selected regions. The diffraction peak of 100 superlattice line around 35.6° was hardly observed as shown in Fig. 6.4a, indicating that as-synthesized Fe-Co particles have a disordered structure. It is difficult to obtain the Fe-Co particles with an order structure by electroless deposition due to the relatively high deposition rate of the particles, and the adequate heat treatment is necessary for the ordering process.[10-12]

Figure 6.5a shows the transmission electron microscopy (TEM) images and the corresponding selected-area electron diffraction (SAED) patterns of the cubic iron particle with the [001] incidences. The iron nanocube is single crystal and its crystal face can be indexed to the {100} planes. The weak spots are indexed to SAED patterns of Fe_3O_4 spinel. The (001) planes of Fe_3O_4 are parallel to the (001) plane of the Fe and the [110] directions of Fe_3O_4 are parallel to the [100] of Fe. Namely, the oxide films on Fe nanocube were formed with a following epitaxial relationship to Fe.

$$Fe_3O_4\ (001)\ [110]\ //\ Fe\ (001)\ [100] \qquad [6.1]$$

The similar epitaxial relationship has been observed in the surface-oxidized single crystals of iron.[13-15] The multifaceted Fe-Co particle is also single crystal, and the crystal face is indexed to the {100} planes as shown in Fig. 6.5b.

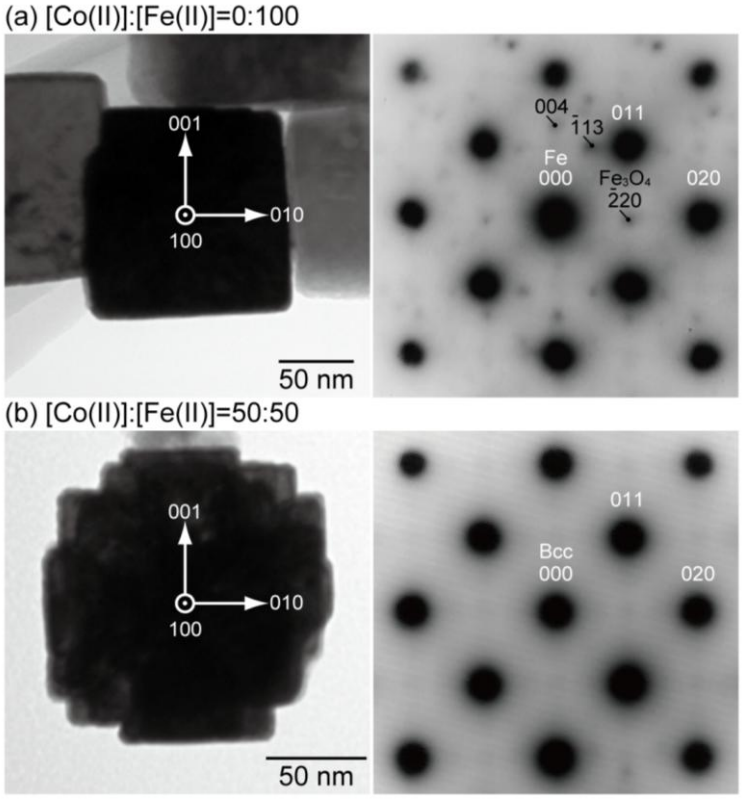

Figure 6.5 TEM images and SAED of the particles synthesized from the solutions containing (a) 0.100 M Fe(II) and (b) 0.050 M Co(II) - 0.050 M Fe(II).

The morphology of a nanocrystal is usually discussed in terms of either the thermodynamically-determined equilibrium form or the kinetically-determined growth form. The equilibrium form of a nanocrystal is determined by the surface energy of the crystal planes; a crystal is enclosed by crystallographic facets with the lowest surface energy according to the surface free energy minimization principle. On the other hand, the growth form of a nanocrystal is mainly determined by the ratio of the growth rates in the crystal direction. In the present system, the shape of the particles is considered to be far from the equilibrium form, because the growth rate of particles is relatively high. Wang *et al.* reported that the growth form of a cubic nanocrystal changes depending on the ratio (R) of the growth rates in the [100] to that in the [111] direction, and the perfect cubes bounded by the {100} planes is formed at R below 0.58.[16] It is qualitatively understood that the growth rate

of iron particles in the [100] direction is lower than that in the [111] direction since the surface energy of (100) planes is higher than that of (111) planes, leading to the formation of iron particles with cubic structures. The formation mechanism for the multifaceted Fe-Co particles is discussed later based on the results of electrochemical in-situ measurements.

6.3.2 Characterization of Fe-Co particles and wires formed by hydrazine reduction

By mixing the metallic salt solution and the hydrazine solution for 3 hours, the Fe-Co particles were formed as shown in Figure 6.6. The size distributions and mean diameter of the particles are also indicated. The particles about 660 nm in diameter were formed in Co(II) 100% solution. At [Co(II)]:[Fe(II)]=100:0 to 40:60, the size of particles increase and the size distribution becomes broader with an increase in a concentration of Fe(II). In solution containing more than 60% Fe(II), the particle size drastically decreases at a higher concentration of Fe(II).

Figure 6.7 shows the atomic ratios and yields of the particles synthesized from the solutions before and after adding N_2H_4. The atomic ratios of iron to cobalt in the Fe-Co particles synthesized in the solutions containing N_2H_4 are almost equal to the ratios of Fe(II) to Co(II) ions in solutions, which are lower values than that of the particles formed in the solution before adding N_2H_4. Figure 6.7b shows that the yields of metal increase by addition of N_2H_4 in each concentration ratio except the solution only containing Fe(II). The yield is high above 90% at [Co(II)]:[Fe(II)]=100:0 to 40:60 and suddenly drops low below 15% at [Co(II)]:[Fe(II)]=30:70. Regardless of an addition of N_2H_4, the yield of iron particles remains about 6%.

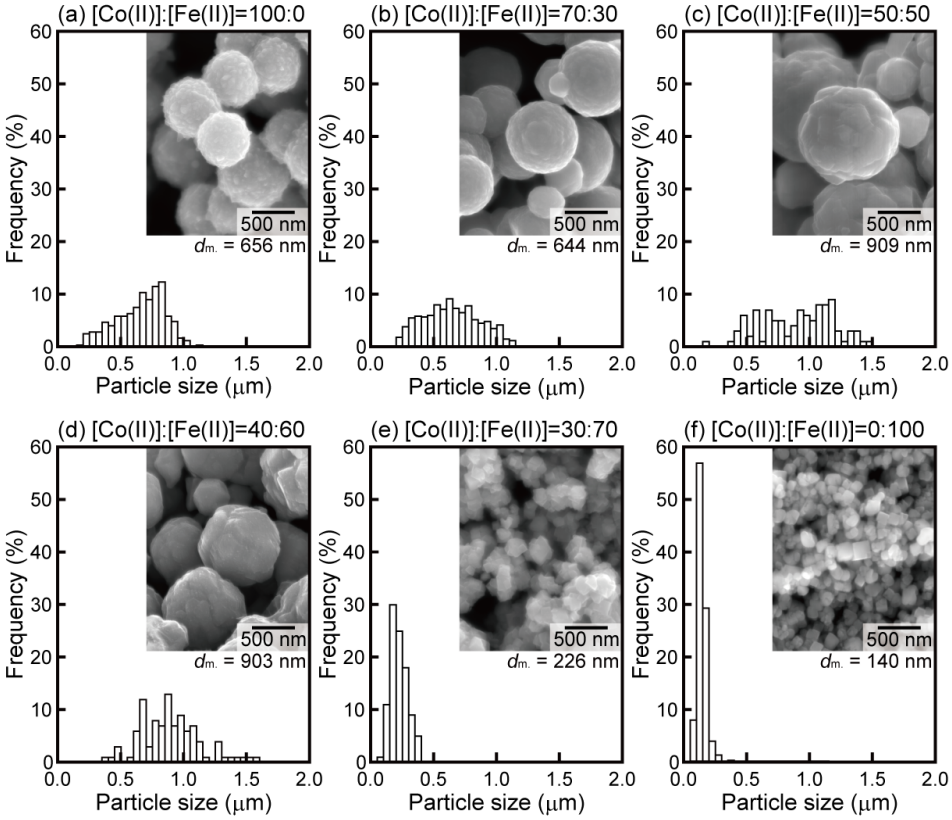

Figure 6.6 SEM images and size distributions of the particles synthesized from the solutions containing (a) 0.050 M Co(II), (b) 0.035 M Co(II) - 0.015 M Fe(II), (c) 0.025 M Co(II) - 0.025 M Fe(II), (d) 0.020 M Co(II) - 0.030 M Fe(II), (e) 0.015 M Co(II) - 0.035 M Fe(II), and (f) 0.050 M Fe(II).

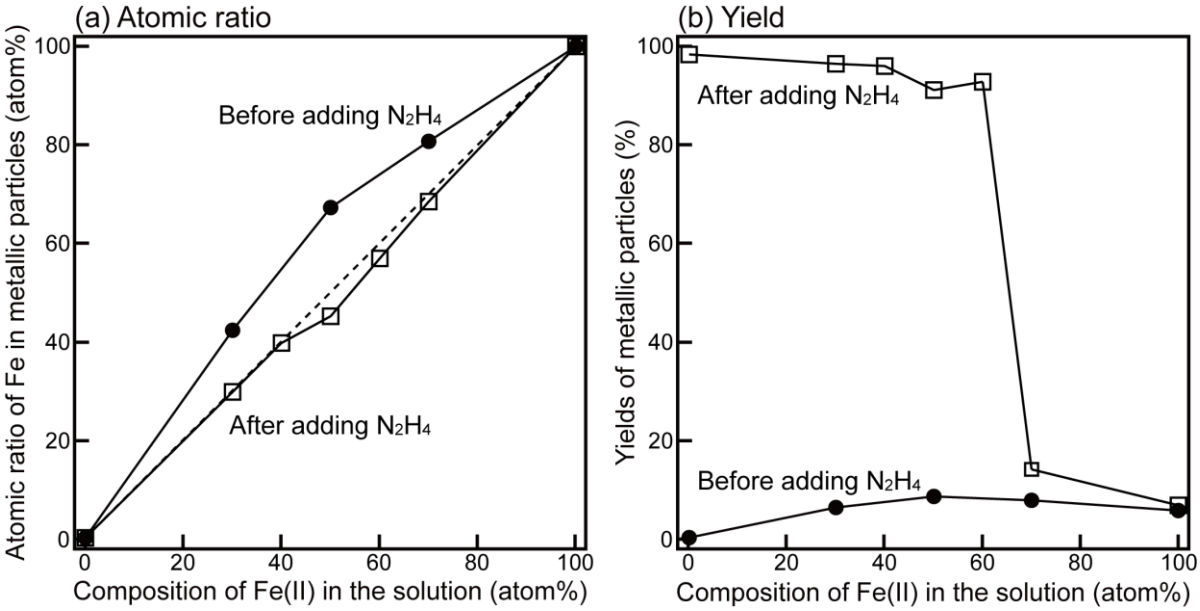

Figure 6.7 (a) Atomic ratios of iron and (b) yields of the Fe-Co particles synthesized from the solutions before and after adding the hydrazine solution.

The XRD patterns of the particles synthesized in the solutions containing N_2H_4 are shown in Figure 6.8. The hexagonal close-packed (hcp) and the face-centered cubic (fcc) peaks of cobalt are observed at [Co(II)] : [Fe(II)] = 100 : 0 (Fig. 6.8a). In the XRD patterns of Fe-Co alloy (Figs. 6.8b-d) and iron particles (Fig. 6.8e), bcc peaks are observed and the peaks shift to lower angle with an increase in a concentration of Fe(II) due to the change of lattice parameters of Fe-Co alloy. The peak positions in the XRD patterns of Fe-Co particles synthesized from the solution containing N_2H_4 are higher angle than that of Fe-Co particles obtained in the solution before adding N_2H_4. This also indicates that the atomic ratios of iron to cobalt in the Fe-Co particles synthesized in the solutions containing N_2H_4 are lower than that in the particles obtained in the solutions before adding N_2H_4.

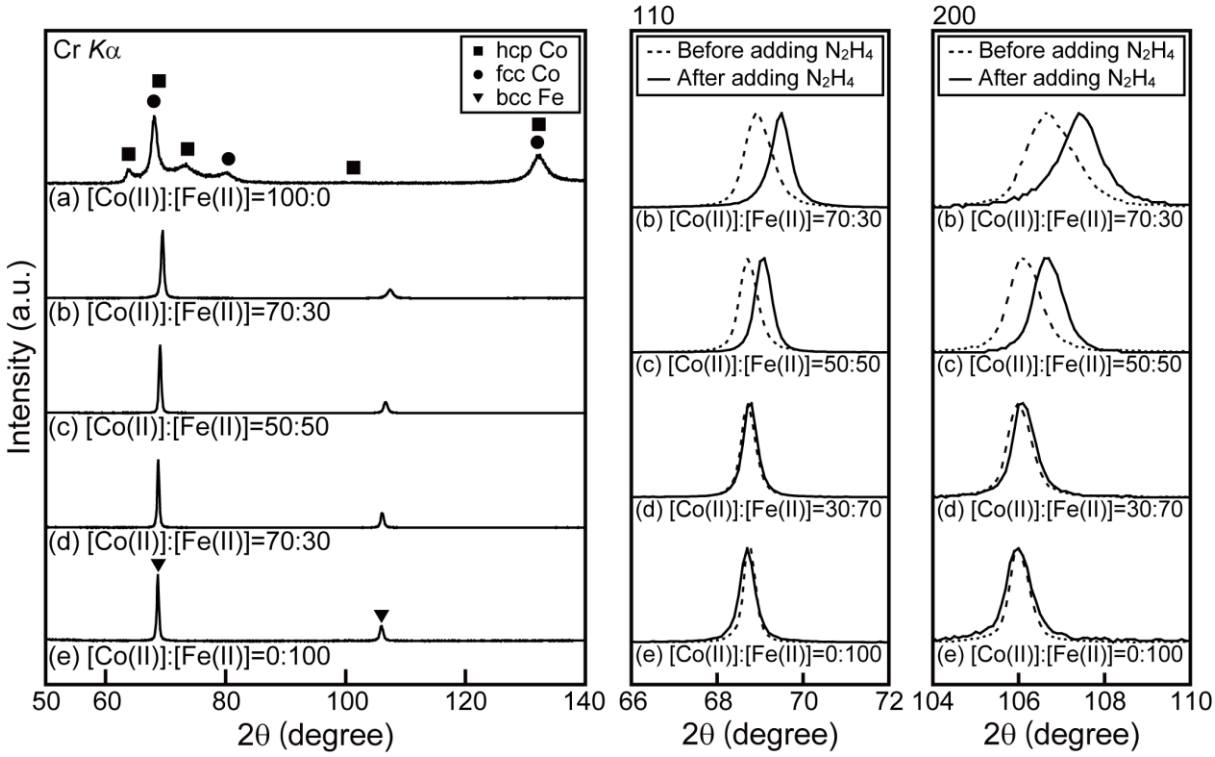

Figure 6.8 XRD patterns of the particles synthesized from the solutions containing (a) 0.050 M Co(II), (b) 0.035 M Co(II) - 0.015 M Fe(II), (c) 0.025 M Co(II) - 0.025 M Fe(II), (d) 0.015 M Co(II) - 0.035 M Fe(II), and (e) 0.050 M Fe(II).

Figure 6.9 shows the weight change of metals deposited on the QCM substrate immerged in the reaction solution. The slope of the curve, corresponding to the deposition rate, becomes smaller with an increase in a concentration of Fe(II). The weight increases with time and reaches a constant value after a certain reaction time at conditions of [Co(II)]:[Fe(II)]=100:0 to 40:60 (Figs. 6.9a-c). By contrast, the metal deposition still proceeds in the solutions of [Co(II)]:[Fe(II)]=30:70 at 3 hours (Fig. 6.9d) and the deposition of iron is hardly observed in 100% Fe(II) solution (Fig. 6.9e). Thus, the metal deposition is not completely finished at 3 hours at [Co(II)]:[Fe(II)]=30:70 and 0:100, and actually, the yields of particles are low values below 15% as shown in Table 6.1. The total amount of metal deposited on a QCM substrate increases with increasing a concentration of Fe(II) at [Co(II)]:[Fe(II)]=100:0 to 40:60. In the previous chapters, we showed that the total deposition amount corresponds to the inhomogeneous nucleation on the QCM substrate, which is inversely related to the nucleation in the reaction solution. Namely, the formation of nuclei in solution suppresses the heterogeneous nucleation on the QCM substrate. Thus, the increase in the amounts deposited on a QCM substrate by addition of Fe(II) is due to the suppression of the homogeneous nucleation in the solutions.

Figure 6.10 shows the SEM images of Fe-Co wires synthesized under a magnetic field changing the concentration ratios of Co(II) to Fe(II). The alloy compositions of the wires are shown in Table 6.2. In the absence of a nucleating agent, the diameter of the cobalt wires is thick about 700 nm as shown in Figure 6.10a. The wire diameter can be controlled by addition of H_2PtCl_6; in the presence of 1.00 mM H_2PtCl_6, while wavy cobalt nanowires of 150 nm in diameter were formed from 100% Co(II) solution (Fig. 6.10b), straight Fe-Co alloy wires were obtained in solution containing Co(II) and Fe(II) (Figs. 6.10c-e). From 100% Fe(II) solution, however, iron particles were formed as shown in Fig. 6.10f.

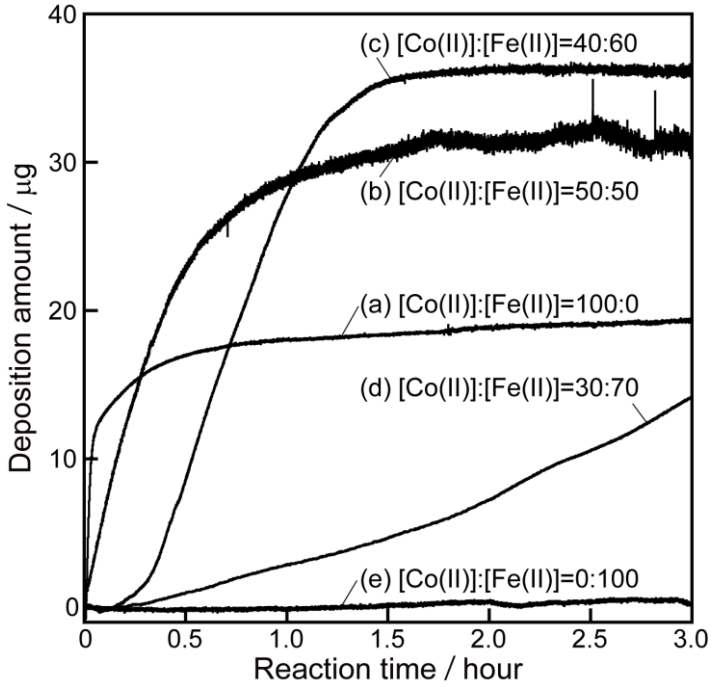

Figure 6.9 Weight of metal deposited on the gold-sputtered QCM substrate from the solutions containing (a) 0.050 M Co(II), (b) 0.025 M Co(II) - 0.025 M Fe(II), (c) 0.020 M Co(II) - 0.030 M Fe(II), (d) 0.015 M Co(II) - 0.035 M Fe(II), and (e) 0.050 M Fe(II).

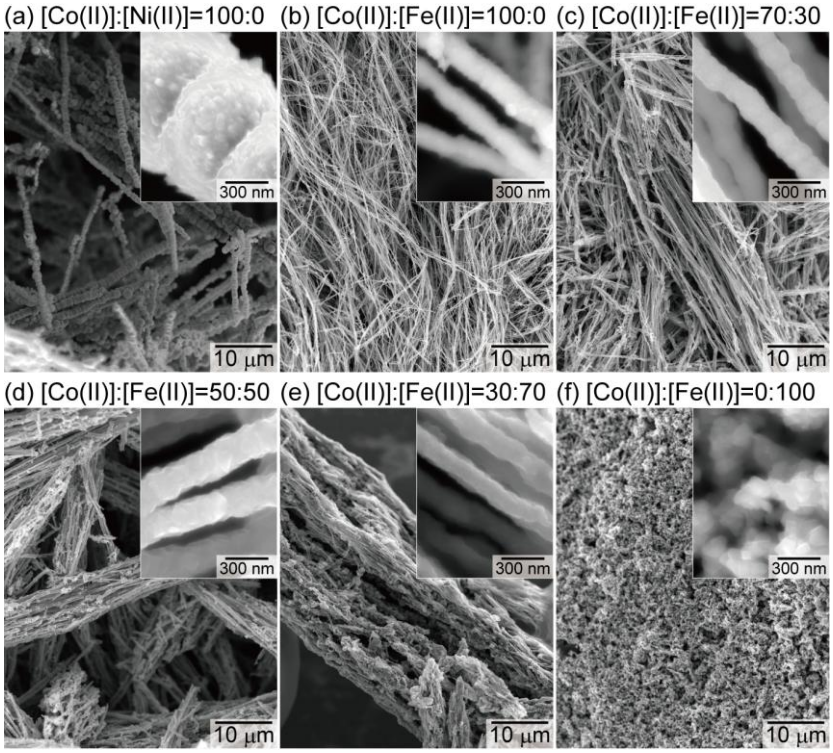

Figure 6.10 SEM images of the wires synthesized from the solutions containing (a) 0.050 M Co(II), (b) 0.050 M Co(II), (c) 0.035 M Co(II) - 0.015 M Fe(II), (d) 0.025 M Co(II) - 0.025 M Fe(II), (e) 0.015 M Co(II) - 0.035 M Fe(II), and (f) 0.050 M Fe(II). The nucleating agent, 1.0 mM H_2PtCl_6, is added in the solution (b) to (f).

Table 6.2 Atomic ratio of the wires synthesized changing the concentration ratio of Co(II) to Fe(II) in the reaction solution.

Concentration ratio of metallic species in the reaction solution	Atomic ratio of metal (atom%)	
[Co(II)] : [Fe(II)]	Co	Fe
(a) 100 : 0	100.0	0.0
(b) 70 : 30	70.5	29.5
(c) 50 : 50	50.6	49.4
(d) 30 : 70	37.2	62.8
(e) 0 : 100	0.0	100.0

6.4 Discussion

6.4.1 Formation of iron particles in the metallic salt solution

The formation mechanism of iron particles in EG with a high concentration of NaOH has been discussed in various reports. According to Viau *et al.*, the iron particles are formed by the following disproportional reaction of Fe(II), and polyols are too weak to reduce Fe(II) ions.[7] It has already been reported that the following disproportionation reaction of Fe(II) occurs in an aqueous solution[17]

$$4Fe(OH)_2 \rightarrow Fe + Fe_3O_4 + 4H_2O \quad [6.2]$$

in parallel with the following competitive reaction called the Schikorr reaction[18]

$$3Fe(OH)_2 \rightarrow H_2 + Fe_3O_4 + 2H_2O \quad [6.3]$$

According to the calculation using the thermodynamic data, the disproportionation reaction takes place at a temperature above about 353 K.[17] Due to the less thermodynamic data of iron species in EG solution, it is difficult to predict whether the disproportionation reaction occurs in this system.

Recently, Jeyadevan *et al*. reported that the polyol (EG) do have the potential to reduce Fe(II).[5,6] The reduction reaction of Fe(II) to Fe by polyol process is written as

$$2CH_2OH\text{-}CH_2OH \rightarrow 2CH_3CHO + 2H_2O \quad [6.4]$$

$$2CH_3CHO + Fe(OH)_2 \rightarrow CH_3COCOCH_3 + 2H_2O + Fe \quad [6.5]$$

They claimed that if iron is synthesized through disproportionation reaction, the equal quantities of metallic iron and magnetite particles should be obtained, and that the less magnetite proved the formation of iron particles in polyol is not due to the disproportionation reaction. However, Viau *et al.* also reported that the crystallization of magnetite is prevented in EG under certain conditions; (i) the initial concentration of Fe(II) must be limited to about 0.2 M; (ii) NaOH must be used in large excess with respect to Fe(II) hydroxide stoichiometry; (iii) water must be removed.[7] The formation process of iron particles in EG solution is highly controversial issue, since there has been no definite experiment to determine what works as a reducing agent in the formation of iron particles so far. Therefore, we applied the electrochemical measurements such as a mixed potential and a cyclic voltammetry to the formation process of iron particles in order to know the main redox reactions proceeding on the particles surface.

For further discussion, the following reduction current of Fe(II) ions was separately evaluated from the contribution of the reductive decomposition of EG by measuring the weight change of metal deposited on the QCM substrate

$$Fe(II) + 2e \rightarrow Fe \quad [6.6]$$

where Fe(II) represents all the metallic species, e.g. Fe^{2+}, $FeOH^{+}$, $Fe(OH)_2$, $HFeO_2^{-}$, FeO_2^{2-}, and the iron alkoxide.[17] Figure 6.11 shows cyclic voltammograms measured in EG containing 4.0 M NaOH and (a) 0.100 M $FeCl_2$ and (b) 0.100 M $CoCl_2$ using a gold-sputtered QCM substrate as a working electrode. The temperature of the solution was kept at 353 K with argon gas bubbling to remove the dissolved oxygen. Moreover, to prevent the oxidation reaction of Fe(II) to Fe(III) on a counter electrode, the dual cell system was adopted

for the measurement of the redox potential of Fe(II)/Fe redox pair as shown in Figure 6.12.[19] The counter electrode was immerged in a cell containing EG with 0.10 M $LiClO_4$ as a supporting electrolyte, which was separated from another cell by an ion-exchange membrane (ASTON Ltd., NEOSEPTA CMX).

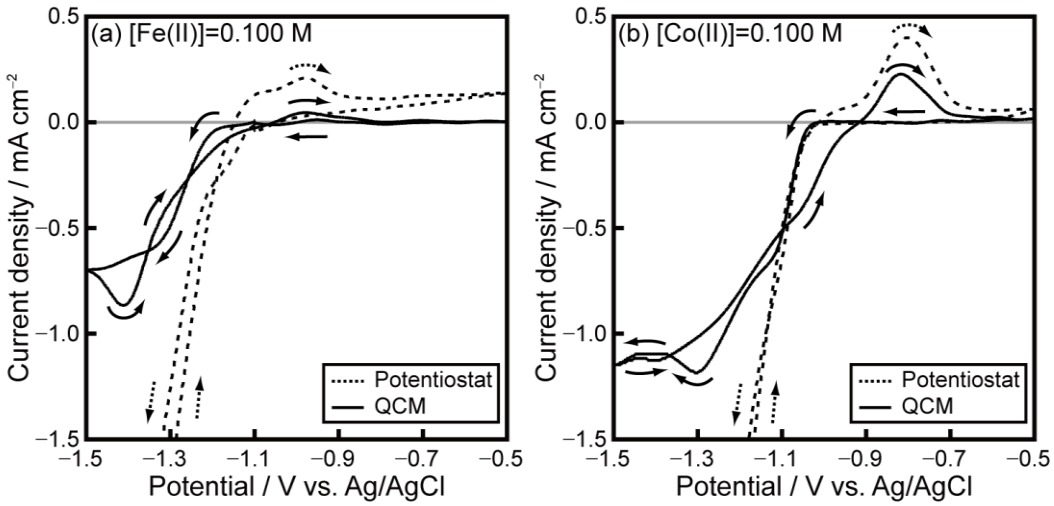

Figure 6.11 Cyclic voltammograms measured by potentiostat (dotted line) and QCM (solid line) at 1 mV s^{-1} in EG containing 4.0 M NaOH (a) 0.100 M $FeCl_2$ and (b) 0.100 M $CoCl_2$.

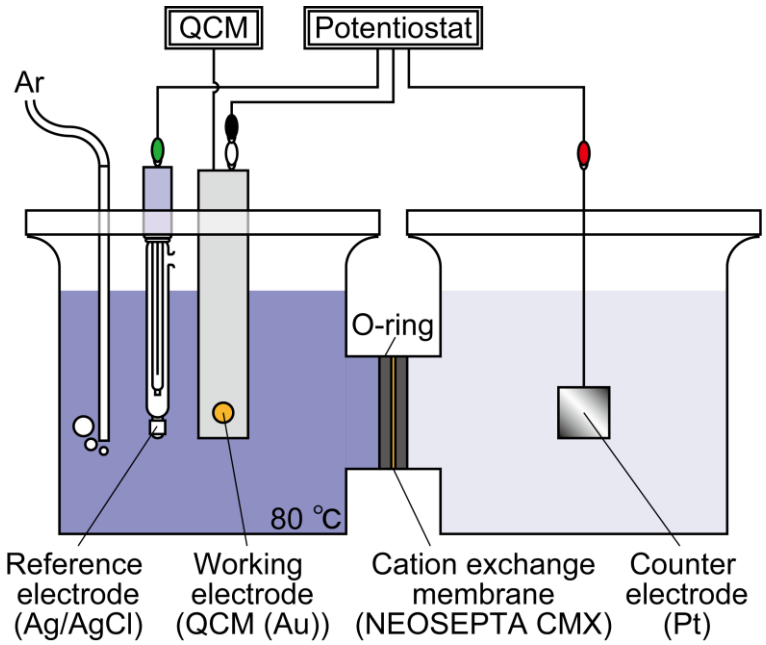

Figure 6.12 Schematic illustration of the dual cell system for the cyclic voltammetry in EG containing Fe(II).

In a cyclic voltammogram evaluated from the potentiostat (Fig. 6.11a, dotted line), the large cathodic current due to the decomposition of the solvent is observed below about −1.05 V during the cathodic sweep. The oxidation current of hydrogen adsorbed on the substrate is seen above −1.15 V only in the anodic sweep. The anodic current due to the oxidation of Fe(II) to Fe(III) is also observed above −1.05 V. In a cyclic voltammogram evaluated from a weight change observed by QCM (Fig. 6.11a, solid line), the cathodic current due to the iron deposition is observed below about −1.1 V vs. Ag/AgCl during the cathodic sweep. During the anodic sweep, the iron deposition and dissolution are seen below and above −1.05 V, respectively. Thus, the redox potential of Fe(II)/Fe redox pair can be determined approximately −1.05 V. The dissolution of iron is hardly observed above −0.85 V owing to the formation of passivation film. The anodic current due to the oxidation of Fe(II) to Fe(III) is also observed above −1.05 V. Similarly, the redox potential of Co(II)/Co is about −0.92 V which is more positive value than that of Fe(II)/Fe, and the reduction current density of Co(II)/Co is larger than that of Fe(II)/Fe.

Figure 6.13a shows the time-dependence of mixed potential measured on the iron substrate during the synthesis of iron particles, where EG contains 4.0 M NaOH and 0.100 M $FeCl_2$. For comparison, the mixed potential in EG only containing 4.0 M NaOH was also indicated. By addition of NaOH pellets, the mixed potential in solution with Fe(II) gradually dropped below the redox potential of Fe(II)/Fe (−1.05 V) and reached about −1.17 V. The difference between the redox potential and the mixed potential corresponds to the driving force of the metal deposition, indicating that the iron deposition is thermodynamically possible. Actually, the iron particles were obtained as shown in Fig. 6.1d. A mixed potential in solution with Fe(II) is always lower than that in solution without Fe(II). On the contrary, Fig. 6.13b shows that the mixed potential in solution containing 4.0 M NaOH and

0.100 M Co(II) is higher than that in solution without Co(II). Similar tendency was seen in a mixed potential in solutions with and without Ni(II) (Fig. 6.13c).

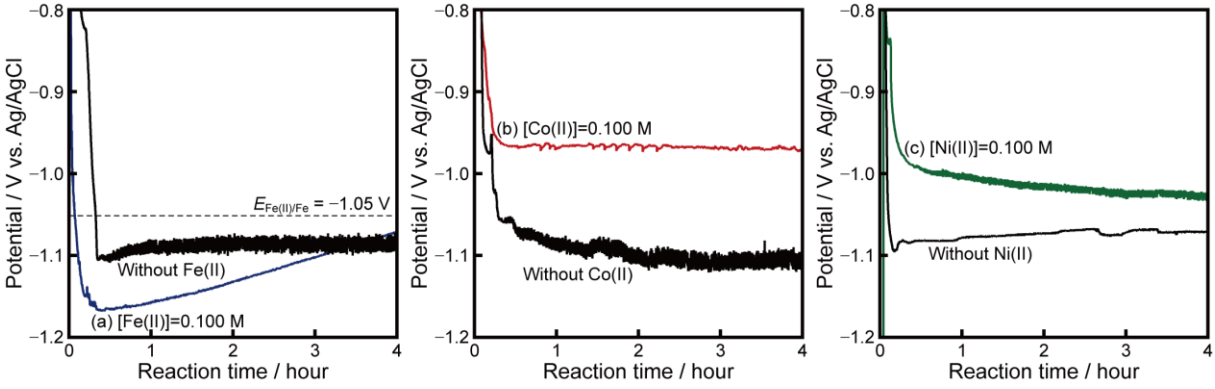

Figure 6.13 Time dependence of mixed potential measured in EG containing 4.0 M NaOH, (a) 0.100 M $FeCl_2$, (b) 0.100 M $CoCl_2$, and (c) 0.100 M $NiCl_2$ using iron, cobalt, nickel substrates as working electrodes, respectively. For comparison, time dependence of mixed potential measured in EG only containing 4.0 M NaOH is also indicated.

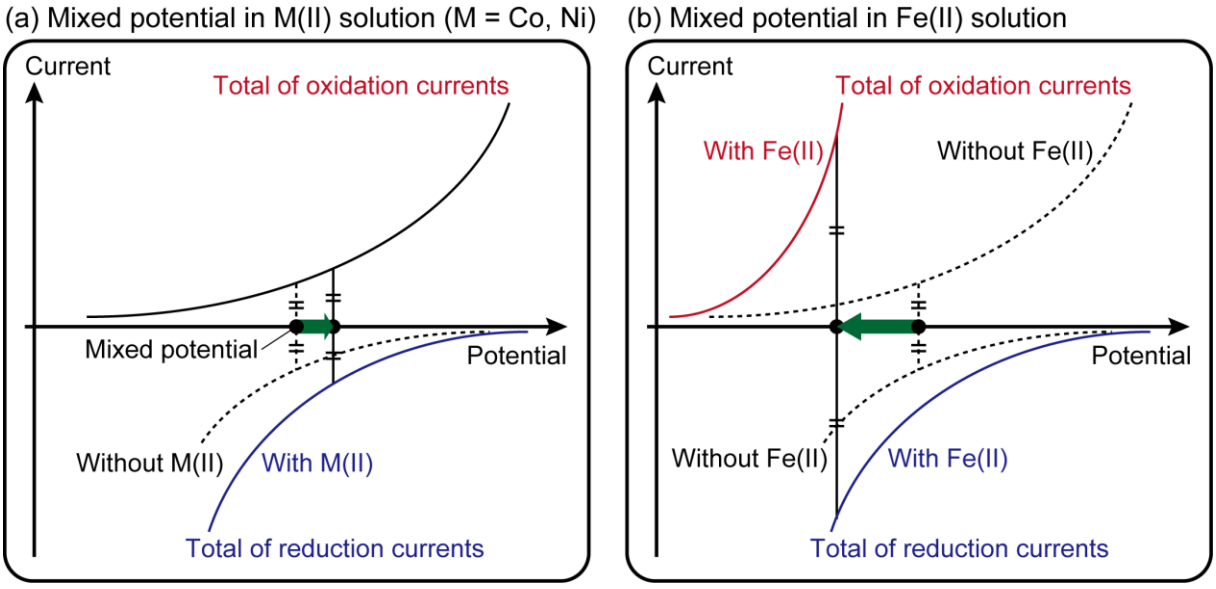

Figure 6.14 Schematic illustrations of potential-current curves and mixed potential during the reaction in Figure 6.13.

The shift of the mixed potential is explained by the balance of the cathodic currents and the anodic currents schematically shown in Figure 6.14. In EG only containing NaOH, a mixed potential is mainly determined by the balance of EG oxidation reactions and a reductive decomposition of large amount of EG. By addition of Co(II) or Ni(II), the cathodic currents increases due to the contribution of reduction currents of Co(II) of Ni(II) and a mixed potential is expected to positively shift (Fig. 6.14a). On the other hand, the decrease of mixed potential by addition of Fe(II) cannot be explained without considering the following oxidation reaction of Fe(II) to Fe(III)

$$\mathrm{Fe(II)} \rightarrow \mathrm{Fe(III)} + \mathrm{e} \qquad [6.7]$$

The addition of Fe(II) contributes not only to the reduction currents but also to the oxidation currents as schematically drawn in Fig. 6.14b. A mixed potential negatively shifts due to a large anodic current density of the Fe(II) oxidation, indicating that the Fe(II) works as a strong reducing agent in the present system. Additionally, it is noted that a mixed potential in solution with Fe(II) gradually increases with time while a mixed potential is almost stable in solution with Co(II) and Ni(II). The increase of potential in solution with Fe(II) is due to the consumption of Fe(II) associated with the disproportionation reaction of Fe(II) to Fe(III) and iron particles. The CV profile (Fig. 6.11) shows that the reductive decomposition of EG occurs when a mixed potential is below the redox potential of Fe(II)/Fe about −1.05 V, and thus, Fe(II) is consumed in both the reduction of EG and the formation of iron particles. Consequently, the iron particles were partially formed by disproportionation reaction, and the competitive oxidation reaction of Fe(II) to reduce EG results in the low yield of the particles about 5%.

6.4.2 Formation of Fe-Co particles in the metallic salt solution

To discuss the morphological changes and anomalous deposition behaviors of Fe-Co particles in EG solution, the electrochemical measurements were applied to the formation process of Fe-Co particles. Figure 6.15 shows the time-dependence of mixed potential in the solution by changing the concentration ratios of Co(II) to Fe(II). A mixed potential in 100% Co(II) solution gradually dropped below the redox potential of Co(II)/Co and reached a constant value about −0.97 V, indicating that the cobalt deposition is thermodynamically possible. Actually, the cobalt deposition was observed on a cobalt-deposited QCM substrate immerged in the solution (Figure 6.16), while no cobalt particles were formed in solution as shown above. Thus, this solution is a condition for the electroless plating of cobalt by polyol (EG) reduction.

In the solution containing Fe(II), the mixed potential shifts lower at a higher concentration ratio of Fe(II), also indicating that Fe(II) works as a strong reducing agent in the formation of Fe-Co and iron particles. As found from Figs. 6.15a and c, the driving force of iron deposition, which can be evaluated by the difference between the redox potential and the mixed potential, is higher than that of cobalt, indicating the homogeneous nucleation is more favorable during the formation of iron particles than that of cobalt particles. This results in the different behaviors of cobalt and iron deposition; the iron particles were formed in the solution by homogeneous nucleation due to the strong reduction ability, on the other hand, the electroless plating of cobalt occurred by heterogeneous nucleation owing to the relatively lower reduction ability of EG.

In the formation of Fe-Co alloy particles, it is expected that the homogeneous nucleation of cobalt is more favorable than that of iron, since the redox potential of Co(II)/Co is much higher than that of Fe(II)/Fe. By addition of Co(II), the nucleation, including

two-dimensional nucleation on the surface of particles, is prompted, which results in the formation of multifaceted Fe-Co particles as schematically depicted in Figure 6.17.

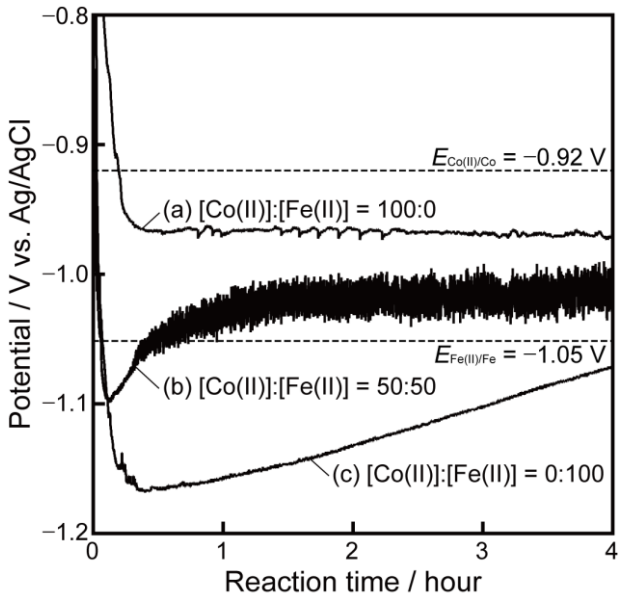

Figure 6.15 Time dependence of mixed potential measured in EG containing 4.0 M NaOH, (a) 0.100 M Co(II), (b) 0.050 M Co(II) - 0.050 M Fe(II), and (c) 0.050 M Fe(II). The redox potentials of Fe(II)/Fe and Co(II)/Co redox pairs are also indicated.

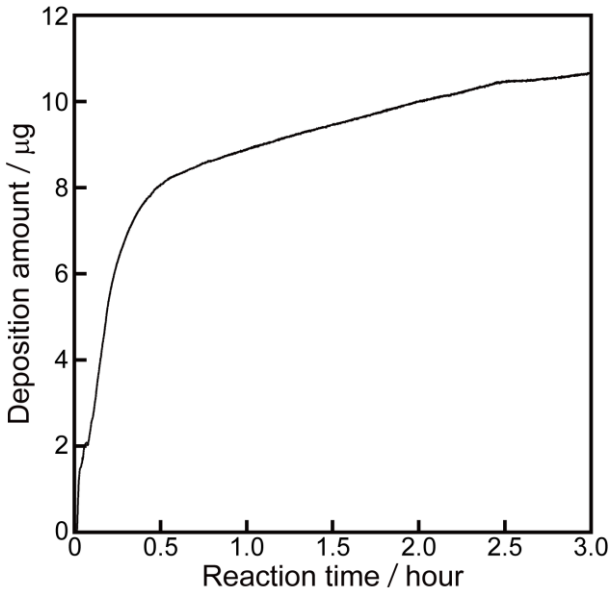

Figure 6.16 Weight of metal deposited on the cobalt-deposited QCM substrate from the solutions containing 4.0 M NaOH and 0.100 M Co(II).

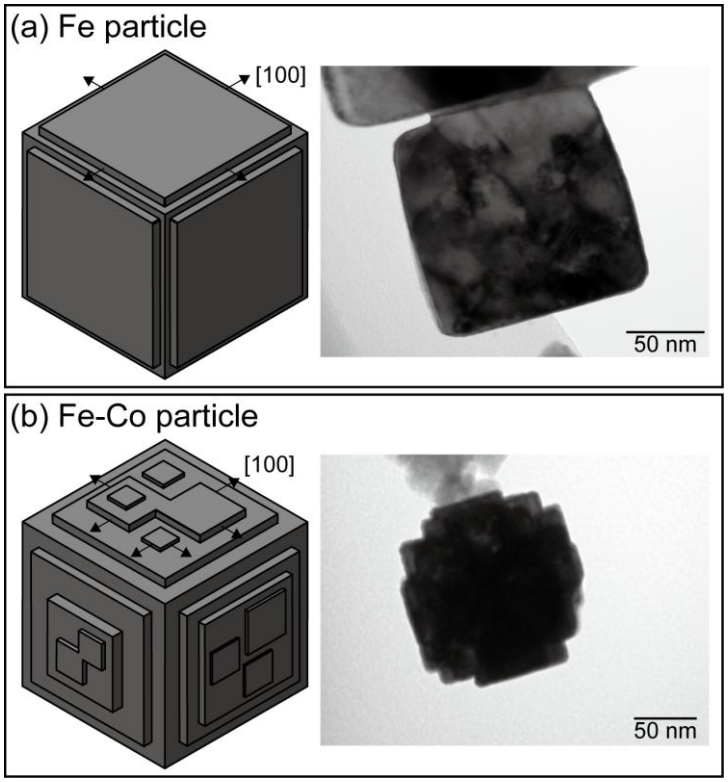

Figure 6.17 Schematic illustration of the formation of (a) cubic iron particles and (b) multifaceted Fe-Co particles.

It should be noted that the atomic ratios of iron to cobalt is higher than the concentration ratios of Fe(II) to Co(II) ions in solution as shown in Table 6.1, since iron is thermodynamically less noble than cobalt and it is expected that the deposition rate of iron is lower than that of cobalt. Actually, the reduction current density of Fe(II) species is smaller than that of Co(II) species as shown in Fig. 6.11. According to Brenner's definition, the codeposition of iron-group metals is widely recognized as an "anomalous electroplating type" since the less noble metal is deposited preferentially.[20] The electrodeposition of Fe-Co alloys, whether from simple or complex baths, occurs in an anomalous type in which the less noble metal (Fe) is preferentially reduced.[21-23] The reaction mechanism of anomalous codeposition in aqueous solution is generally proposed as following;[24-29]

$$2H_2O + 2e \rightarrow H_2 + 2OH^- \quad [6.8]$$

$$M^{2+} + OH^- \rightarrow M(OH)^+ \quad [6.9]$$

$$M(OH)^+ \rightarrow M(OH)_{ads}^+ \quad [6.10]$$

$$M(OH)_{ads}^+ + 2e \rightarrow M + OH^- \quad [6.11]$$

where M indicates iron, cobalt, and nickel atoms. In general, the anomalous deposition in aqueous solution was attributed to hydrogen evolution because of the side reaction of metal reduction at the cathode surface. The increase in the concentration of hydroxyl ions leaded to the formation and adsorption of metal hydroxide ions on cathode surface. Due to the sequence of metal hydroxide ions with respect to increase the adsorption ability is $Ni(OH)^+$ < $Co(OH)^+$ < $Fe(OH)^+$,[30] the deposition of iron is promoted by the surface enrichment of their corresponding adsorbed metal hydroxide ions. In contrast, the cobalt deposition is suppressed because of the few adsorption sites of $Co(OH)^+$. Although many attempts have been made to explain the anomalous codeposition of alloys, there is still no universally accepted theory. This reaction mechanism above cannot be adopted directly to the present system, because the solvent for the syntheses of Fe-Co particles is not water but EG and the concentration of NaOH is high enough for metallic ions to form hydroxide and/or alkoxide sol, however, it is likely that the similar mechanism leads to the anomalous deposition behaviors of Fe-Co particles in EG solutions.

6.4.3 Formation of Fe-Co particles by hydrazine reduction

In the formation process of nanoparticles and nanowires by electroless deposition using N_2H_4, the catalytic activities of metal in the oxidation reaction of N_2H_4 strongly affects the deposition behaviours of metal, as discussed in the previous chapter. Therefore, the catalytic activities of Fe-Co alloys were evaluated by the anodic polarization curves to discuss

the iron alloying effect of cobalt particles and wires. Figure 6.18 shows anodic polarization curves measured in EG containing 4.0 M NaOH and 2.50 M N_2H_4 using cobalt, iron, and Fe-Co alloy substrates as working electrodes. The anodic current due to the oxidation of N_2H_4 is observed above −1.21 and −1.16 V vs. Ag/AgCl on the cobalt and iron substrates, respectively. The excess potential for the N_2H_4 oxidation is higher and the anodic current density becomes smaller on a substrate with a higher composition ratio of iron. At the redox potential of N_2H_4, there is a relationship $i_a = -i_c = i_0$, and the exchange current density, i_0, can be determined by Tafel extrapolation. The exchange current density becomes smaller on a substrate with a higher composition ratio of iron, as it is seen in Table 6.3. Namely, a catalytic activity in the oxidation reaction of N_2H_4 becomes lower on the Fe-Co substrate with a higher iron composition ratio. This results in the lower growth rate of metal by addition of Fe(II) as shown in the in-situ QCM measurement (Fig. 6.9).

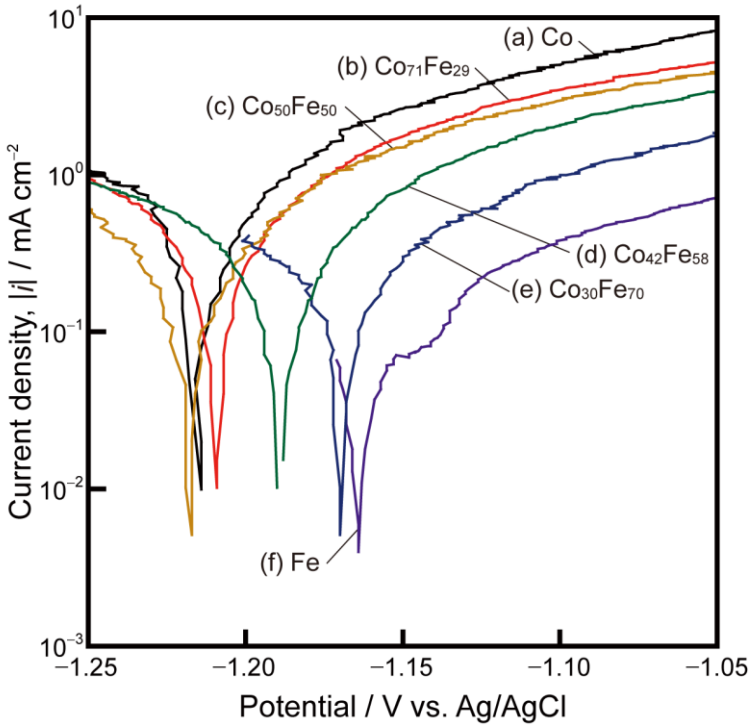

Figure 6.18 Polarization curves measured on (a) Co, (b) $Co_{71}Fe_{29}$, (c) $Co_{50}Fe_{50}$, (d) $Co_{42}Fe_{58}$, (e) $Co_{30}Fe_{70}$, and (f) Fe substrates in EG containing 4.0 M NaOH and 2.50 M N_2H_4. Sweep rate is 1 mV s^{-1}.

Table 6.3 Exchange current densities of the hydrazine oxidation reaction determined by Tafel extrapolation from the polarization curves of Fig. 6.18.

Working electrode	Exchange current density, i_0 / mA cm^{-2}
(a) Co	1.7
(b) $Co_{71}Fe_{29}$	1.4
(c) $Co_{50}Fe_{50}$	1.0
(d) $Co_{42}Fe_{58}$	0.9
(e) $Co_{30}Fe_{70}$	0.4
(f) Fe	0.2

Figure 6.19 shows the time-dependence of mixed potential in the solution containing 2.50 N_2H_4, 4.0 M NaOH, and (a) 0.050 M $CoCl_2$ or (b) 0.050 M $FeCl_2$. The redox potentials of Co(II)/Co and Fe(II)/Fe are also indicated. In solution containing Co(II), the mixed potential drops below the −1.2 V and gradually increases due to the consumption of N_2H_4 accompanied with the reduction reaction of Co(II) ions and EG. The mixed potential in Fe(II) solution remains constant value about −1.12 V after about 1 hour. The increase in a mixed potential due to the consumption of N_2H_4 is hardly observed because of a lower catalytic activity of iron in the oxidation of N_2H_4. The driving force of iron deposition is lower than that of cobalt deposition, indicating that the homogeneous nucleation is unfavorable during the formation of iron particles compared to that of cobalt particles.

Consequently, an inhibiting effect on the Fe-Co particle growth by the addition of Fe(II) becomes stronger with increasing a concentration of Fe(II), and the nucleation is reduced simultaneously. The lower nucleation rate of Fe-Co particles by addition of Fe(II) leads to the formation of bigger Fe-Co particles as shown in solutions of [Co(II)]:[Fe(II)]=100:0 to 40:60 (Figs. 6.6a-d). Further addition of Fe(II) results in the

decrease of yields of metal (as shown in Fig. 6.7) due to quite a low growth rate and nucleation rate of Fe-Co particles, as a result, a tiny amount of fine particles are formed in solutions of [Co(II)]:[Fe(II)]=30:70 and 0:100 (Figs. 6.6e and f). In this way, the morphological changes of the Fe-Co particles synthesized by N_2H_4 reduction can be explained by the different catalytic behaviors between cobalt and iron.

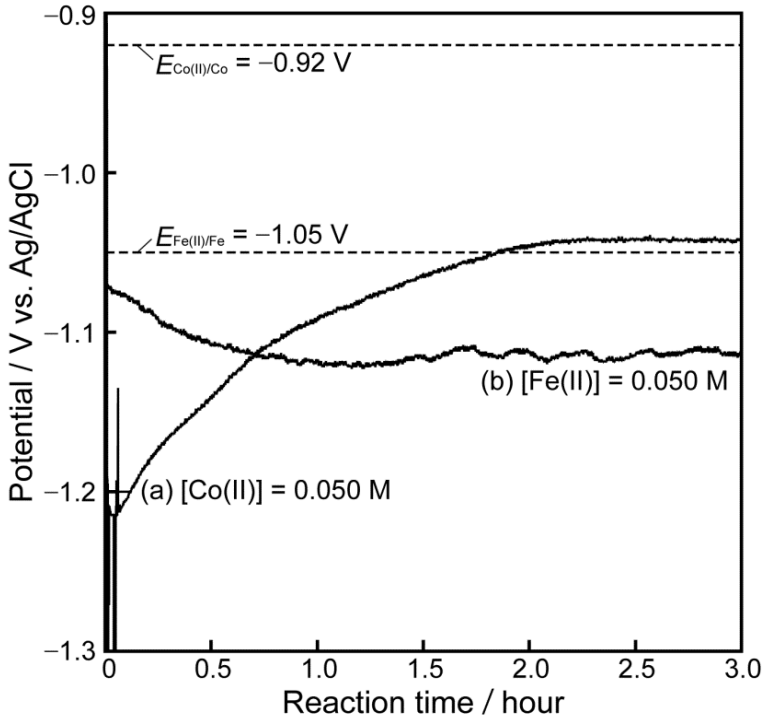

Figure 6.19 Time dependence of mixed potential in the solution containing 2.50 N_2H_4, 4.0 M NaOH, and (a) 0.050 M Co(II) or (b) 0.050 M Fe(II).

6.4.4 Formation of Fe-Co wires by hydrazine reduction

In the formation process of nanowires, first, nanoparticles are formed and aligned along a magnetic field due to the magnetic interaction, followed by the preferential deposition of metal between the particles to decrease the interfacial energy. In 100% Co(II) solution, the growth rate of particles is so high that the particles are connected just after the formation of particles, which results in the formation of wavy nanowires (Fig. 6.10b). In the solution containing both Co(II) and Fe(II), the growth rate is reduced by addition of Fe(II) so that there is enough time for the particles to linearly align along the magnetic field, and thus the straight and rigid wires are formed as shown in Figs. 6.10c-e. In 100% Fe(II) solution, the iron particles are not tightly connected because of their quite low deposition rate and the iron wires are not formed after 3 hours. Evidently, the deposition rate of metal strongly affects the formation of iron alloy wires, which drastically changes their appearance.

Due to the low growth rate of iron attributed to the low catalytic activity in the oxidation reaction of N_2H_4, it is difficult to obtain iron wires by electroless deposition using N_2H_4. In the present system, the formation of iron particles is mainly due to the disproportionation reaction of Fe(II), which is confirmed by the result that the yield of iron particles formed by disproportionation reaction is almost same value (6%) as that of iron particles obtained in solution containing N_2H_4 (Fig. 6.7b). Therefore, it is possible that the iron wires can be fabricated by disproportionaiton reaction under a magnetic field. In fact, as shown in Figure 6.20, the iron nanowires were formed for 3 hours reaction at 353 K in EG containing 4.0 M NaOH and 0.100 M $FeCl_2$ under a magnetic field. The cubic iron particles composing the iron wires align in a longitudinal direction because their shape magnetic anisotropy is stronger than the crystal magnetic anisotropy ([100] direction), as schematically depicted in Figure 6.21. In this way, we can obtain the cobalt, Fe-Co alloy, and iron wires by

the disproportionation reaction and the N_2H_4 reduction, where the electrochemical in-situ measurement is quite effective to understand the formation process of Fe-Co nanowires by electroless deposition.

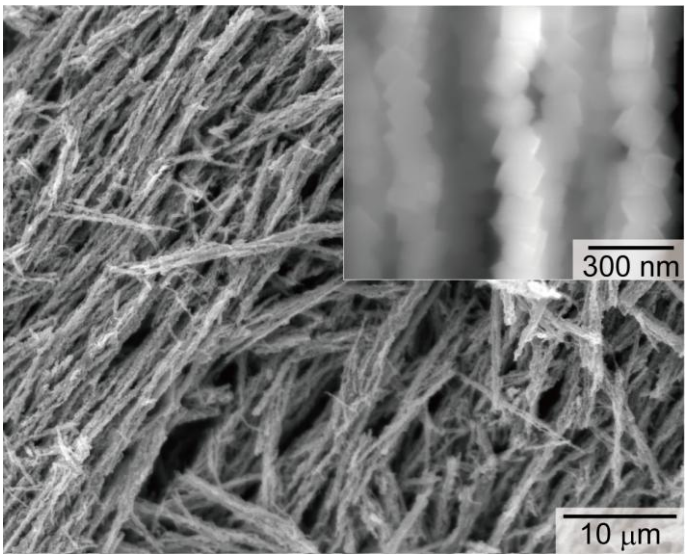

Figure 6.20 SEM images of iron wires synthesized from the solution containing 4.0 M NaOH and 0.100 M $FeCl_2$ under a magnetic field.

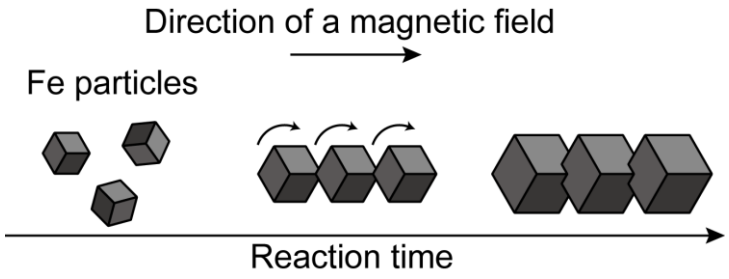

Figure 6.21 Schematic illustration of iron wires by the disproportionation reaction under a magnetic field.

6.5 Conclusion

In the present chapter, the formation process of Fe-Co particles and wires via electroless deposition was electrochemically investigated. Through the electrochemical in-situ measurements, we have obtained the following results.

1. The formation of cubic iron particles in EG with a high concentration of NaOH is mainly due to the disproportionation reaction of Fe(II), which supports the report of Viau *et al*.[7]
2. Fe(II) works as a strong reducing agent in EG solutions containing Co(II) and Fe(II), which leads to the formation of multifaceted Fe-Co particles. The deposition of the Fe-Co particles in EG solutions is "anomalous type" that the less noble metal (iron) is preferentially reduced, the mechanism of which is intriguing and needs further study.
3. The Fe-Co alloy with a higher concentration ratio of iron has the lower catalytic activity in the oxidation reaction of N_2H_4, which results in the lower growth rate of Fe-Co particles at a higher concentration of Fe(II). Namely, iron works as an inhibitor of the particle growth of Fe-Co particles.
4. Additionally, the nucleation becomes unfavorable at a higher concentration ratio of Fe(II) due to the relatively low redox potential of Fe(II)/Fe compared to that of Co(II)/Co.
5. The inhibiting effect of the particle growth and the decrease of the nucleation become more noticeable at a higher concentration ratio of Fe(II), which definitely affects the deposition behaviors, such as morphologies and yields of Fe-Co particles synthesized by N_2H_4 reduction.
6. The catalytic activities of Fe-Co alloy in the oxidation reaction of N_2H_4 also affects the morphology of Fe-Co wires; pure cobalt and Fe-Co wires can be obtained by N_2H_4 reduction owing to the relatively high catalytic activity, while it is difficult to fabricate iron wires due to its low catalytic activity.

7. The iron nanowires can be prepared by disproportionation reaction under a magnetic field.

References

1. M. Kawamori, S. Yagi, and E. Matsubara, *J. Electrochem. Soc*., **159**, E37 (2012).
2. M. Pourbaix: *Atlas of Electrochemical Equilibria in Aqueous Solutions*, Cebelcor, Brüssel (1966).
3. X. Fan, J. Guan, Z. Li, F. Mou, G. Tonga and W. Wanga, *J. Mater. Chem.*, **20**, 1676 (2010).
4. F. Dumestre, B. Chaudret, C. Amiens, P. Renaud, P. Fejes, *Science*, **303**, 821 (2004).
5. R. J. Joseyphus, K. Shinoda, D. Kodama, B. Jeyadevan, *Materials Chemistry and Physics*, **123**, 487 (2010).
6. D. Kodama, K. Shinoda, K. Sato, Y. Konno, R. J. Joseyphus, K. Motomiya, H. Takahashi, T. Matsumoto, Y. Sato, K. Tohji, and B. Jeyadevan, *Adv. Mater*., **18**, 3154 (2006).
7. G. Viau, F. Fiévet-Vincent and F. Fiévet, *J. Mater. Chem.*, **6**, 1047 (1996).
8. Ohnuma, H. Enoki, O. Ikeda, R. Kainuma, H. Ohtani, B. Sundman, K. Ishida, *Acta Materialia*, **50**, 379 (2002).
9. T. Nishizawa and K. Ishida, *Bull. Alloy Phase Diagrams*, **5**, 250 (1984).
10. Q. Zhu, L. Li, M. S. Masteller, and J. D. Corso, *Appl. Phys. Lett.*, **69**, 3917 (1996).
11. Y. Ustinovshikov and B. Pushkarev, *J. Alloys Compd.*, **424**, 145 (2006).
12. G. B. Chon, K. Shinoda, S. Suzuki, and B. Jeyadevan, *Materials Transactions*, **51**, 707 (2010).
13. P. L. Fan and L. O. Brockway, *J. Electrochem. Soc*., **121**, 1534 (1974).

14. L. E. Collins and O. S. Heavens, *Proc. Phys. Soc.*, **70**, 265 (1956).

15. M. J. Graham and R. J. Hussey, *Oxidation of Metals*, **15**, 407 (1981).

16. Z. L. Wang, *J. Phys. Chem. B*, **104**, 1153 (2000).

17. B. Beverskog and I. Puigdomenech, *Corros. Sci.*, **38**, 2121 (1996).

18. G. Schikorr, *Z. Anorg. Allg. Chem.*, **212**, 33 (1933).

19. T. Osaka and J. Sayama, *Electrochim. Acta*, **52**, 2884 (2007).

20. A. Brenner, *Electrodeposition of Alloys, Vol. 1-2*, Academic Press, New York (1963).

21. I. Shao, P. M. Vereecken, C. L. Chien, R. C. Cammarata, and P. C. Searson, *J. Electrochem. Soc*., **150**, C184 (2003).

22. N. Zech, E. J. Podlaha, and D. Landolt, *J. Electrochem. Soc*., **146**, 2886 (1999).

23. A. Bai and C.-C. Hua, *Electrochim. Acta*, **50**, 1335 (2005).

24. J. Matulis and R. Slizys, *Electrochim. Acta*, **9**, 1177 (1964).

25. H. Dahms and I.M. Croll, *J. Electrochem. Soc.*, **112**, 771 (1965).

26. B.V. Tilak, A.S. Gendron, and M.A. Mosoiu, *J. Appl. Electrochem.*, **7**, 495 (1977).

27. B.N. Popov, K.-M. Yin, and R.E. White, *J. Electrochem. Soc.*, **140**, 1321 (1993).

28. D.L. Grimmett, M. Schwartz, and K. Nobe, *J. Electrochem. Soc.*, **137**, 3414 (1990).

29. S. Hessami and C.W. Tobias, *J. Electrochem. Soc.*, **136**, 3611 (1989).

30. M. Matlosz, *J. Electrochem. Soc.*, 140, 2272 (1993).

Chapter 7 *(Application part)*

Application of Metal-nanowire-nonwoven Cloth for a New Type of High-cyclability Integrated Electrode

7.1 Introduction

Commercially widespread Li storage batteries currently employ composite electrodes consisting of binders, conductive additives, and current collectors.[1,2] In terms of the cyclability and capacity, however, they are encountering the limitation, as discussed in section 1.4. In the present work, we propose an integral-type electrode prepared by a metal-nanowire-nonwoven cloth (MNNC) as a new design of high-cyclability and high-rate electrode. The electrode consists of three-dimensionally-tangled conductive metallic nanowires and active materials deposited or coated on the nanowires, which is schematically shown in Fig.1.2b. It is expected that large surface areas can provide efficient ion/electron transports as well as very short solid-state diffusion lengths, and sufficient opening among the wires can accommodate a large volume change, which is especially demanded for the high-capacity negative electrode of LIBs. MNNC plays a role of the most efficient conductive additive as well as the 3D current collectors, and active materials cladded on the surface of the nanowires are the nano-meter sized active materials with high cyclability without any binder. Thus, the present integral-type electrode is so-called all-in-one electrode to replace the present composite electrode.

In the previous chapters, we have fabricated iron group metallic nanowires, such as iron, cobalt, nickel, Co-Ni, and Fe-Co alloys.[3,4] Among them, we selected nickel for the base material of MNNC, due to its low reactivity with lithium, high oxidation resistivity, and

relatively low cost. To demonstrate the advantages of integrated nanowire electrode, we have fabricated a NiO-covered nickel-nanowire-nonwoven cloth (NNNC) as a prototype by a simple two-step method. First, NNNC was synthesized in an aqueous solution via electroless deposition under a magnetic field and, subsequently, annealed in air to obtain the core-clad structure of the NiO-covered nickel nanowires. The electrochemical performance of the electrode was evaluated and compared with a conventional composite electrode.

7.2 Experimental

7.2.1 Fabrication of nickel-nanowire-nonwoven cloth via elecroless deposition

The nickel-nanowire-nonwoven cloth (NNNC) was synthesized by the electroless deposition. The reaction solution was prepared from nickel chloride hexahydrate ($NiCl_2 \cdot 6H_2O$) as a source of nickel ions, hydrazine monohydrate ($N_2H_4 \cdot H_2O$) as a reducing agent, trisodium citrate dihydrate ($Na_3C_6H_5O_7 \cdot 2H_2O$) as a complexing agent, chloroplatinic acid hexahydrate ($H_2PtCl_6 \cdot 6H_2O$) as a nucleating agent, and sodium hydroxide (NaOH) for adjusting pH of the reaction solution. These reagents are all reagent-grade (Nacarai Tesque, Inc.) and used without further purification.

First, 50 cm^3 ion-exchanged water containing 0.100 M $NiCl_2$, 0 - 37.5 mM $Na_3C_6H_5O_7$, 0 - 0.20 mM H_2PtCl_6 was prepared, where M corresponds to mol dm^{-3}. Then, the same amount of ion-exchanged water (50 cm^3) containing 1.00 M N_2H_4 was also prepared. The pH of the both solutions was adjusted to be 11.0 or 12.5 at 298 K using a NaOH aqueous solution. The compositions of reaction solutions are summarized in Table 7.1. The temperature of the solutions was kept at 353 K with nitrogen gas bubbling to remove the dissolved oxygen. The metallic salt solution and the hydrazine solution were mixed at 353 K. After mixing of the metallic salt solution and the hydrazine solution, the concentrations

of Ni(II) and N_2H_4 are 0.050 M and 0.50 M, respectively. The reaction solution was agitated at a rate of 500 rpm with a magnetic stirring unit at 353 K during the reaction for the synthesis of nickel particles. For the synthesis of nickel wires, the reaction solution was kept at 353 K in a water bath located inside the two parallel neodymium magnets. Magnetic field inside the magnets was set to be about 200 mT, which was measured by a Tesla meter (KANETEC Co., Ltd., TM-601). After the reaction, the precipitates were magnetically separated from the solution and washed several times with ion-exchanged water and ethanol.

During the synthesis of nickel particles, a gold-sputtered QCM electrode (SEIKO EG&G, QA-A9M-AU) was immersed in the reaction solution and the mixed potential on the QCM electrode was measured by a potentiostat/galvanostat (Hokuto Denko Co., Ltd., HA-151) using a Ag/AgCl (3.33 M KCl) electrode (Horiba, 2565A-10T) as a reference electrode. The weight of nickel deposited on the QCM electrode, Δm, was calculated from the change in resonance frequency of the QCM electrode, Δf, by Sauerbrey's equation.

Table 7.1 Compositions of the metallic salt solutions and the hydrazine solutions for the synthesis of nickel particles and wires.

	Compositions of metallic salt solutions				Compositions of hydrazine solutions	
	$[NiCl_2]$ (M)	pH	$[H_2PtCl_6]$ (mM)	$[Na_3C_6H_5O_7]$ (mM)	$[N_2H_4]$ (M)	pH
(a)	0.100	11.0	–	–	1.00	11.0
(b)	0.100	12.5	–	–	1.00	12.5
(c)	0.100	12.5	0.20	–	1.00	12.5
(d)	0.100	12.5	0.20	20.0	1.00	12.5
(e)	0.100	12.5	0.20	37.5	1.00	12.5

7.2.2 Fabrication of NiO-covered NNNCs by heat treatment

After the drying process in a desiccator, the NNNCs were annealed at 523, 543, and 573 K in air atmosphere for 16 hours to obtain a NiO active material on the nanowire surfaces. The morphology of the nanowires was observed by a field-emission scanning electron microscope (SEM, JEOL Ltd., JSM-6500F) and a transmission electron microscope (TEM, JEOL Ltd., JEM-2010). The mean diameter and size distribution of the nanowires was determined from the SEM image analysis of the randomly selected 200 wires in each sample. The composition of the nanowires was analyzed with energy-dispersive X-ray (EDX) spectrometry. The oxidation ratio of the nickel nanowires was evaluated by the mass measurement of the nanowires before and after the annealing. According to the oxidation reaction ($2Ni + O_2 \rightarrow 2NiO$), the weight of NiO was calculated from the weight change of the nanowires before and after the annealing. The crystalline structure of the products was investigated by X-ray diffraction (XRD, Rigaku Co., Ltd., RINT-2200) using Cr $K\alpha$ radiation.

7.2.3 Electrochemical evaluation of NiO-covered NNNCs

The half cells were assembled in an argon-filled glove box. The NiO-covered NNNC of 16 ϕ in diameter was used as a working (positive) electrode. The NiO-covered NNNC was used as the electrode without the current collector and the binder. The Li foil and the polypropylene film (Celgard 2500) were used as a counter (negative) electrode and a separator, respectively. A solution of ethylene carbonate (EC) and dimethyl carbonate (DMC) with a 1:2 volume ratio containing 1 M $LiPF_6$ was used as an electrolyte. The charge-discharge profiles were measured at room temperature using a Versatile Multichannel Potentiostat (VMP3, Biologic). For the morphological observation, the electrodes were washed several times with a mixed solution of EC and DMC, and then rinsed using DMC

after the charge-discharge experiments. The washed electrodes were transferred to the sample chamber of the SEM using a transfer vessel to avoid an exposure to air. The CV was also measured by the potentiostat/galvanostat (SP300, Biologic) using a NNNC annealed at 523 K as a working electrode and Li foils as counter and reference electrodes.

7.3 Results and discussion

7.3.1 Formation of nickel-nanowire-nonwoven cloth via elecroless deposition

The reaction solution for the synthesis of NNNCs was optimized by using the electrochemical in-situ measurements. In the present work, pH of the solutions was initially adjusted at 298 K, and actual pH at reaction temperatures was different from the adjusted value. pH decreases with increasing temperature and becomes 9.4 and 10.6, which is initially adjusted to 11.0 and 12.5 at 298 K, respectively. Figure 7.1 shows the potential-pH diagram calculated from the thermodynamic data as shown in Table 7.2 (see chapter 2 for details of calculation methods). The time-dependence of mixed potential and the weight change of nickel deposited on the QCM substrate are also indicated in Figs. 7.1b and c. The metal deposition was observed on the QCM substrate at pH 10.6 (Fig. 7.1c), where the mixed potential is lower than the redox potential of Ni(II)/Ni, however, the formation of nickel particles were not observed in the reaction solution. The $Ni(OH)_2$ flakes remain in the reaction solution at pH 10.6 as shown in Figure 7.2 (i), indicating that this solution is a condition for the electroless plating of nickel. For the formation of nickel nanoparticles, it is necessary to prompt the nucleation. Thus, H_2PtCl_6 was added as a nucleating agent in the reaction solution. Figure 7.2a (ii) shows the XRD patterns of precipitates synthesized in the solution containing 0.10 mM H_2PtCl_6. The peaks of $Ni(OH)_2$ disappears after 15 minutes reaction, and the fcc peaks of nickel are only observed in the XRD patterns of the precipitates.

The nickel nanoparticles about 100 nm in diameter were obtained at 0.10 mM H_2PtCl_6 as shown in Fig 7.2b (ii).

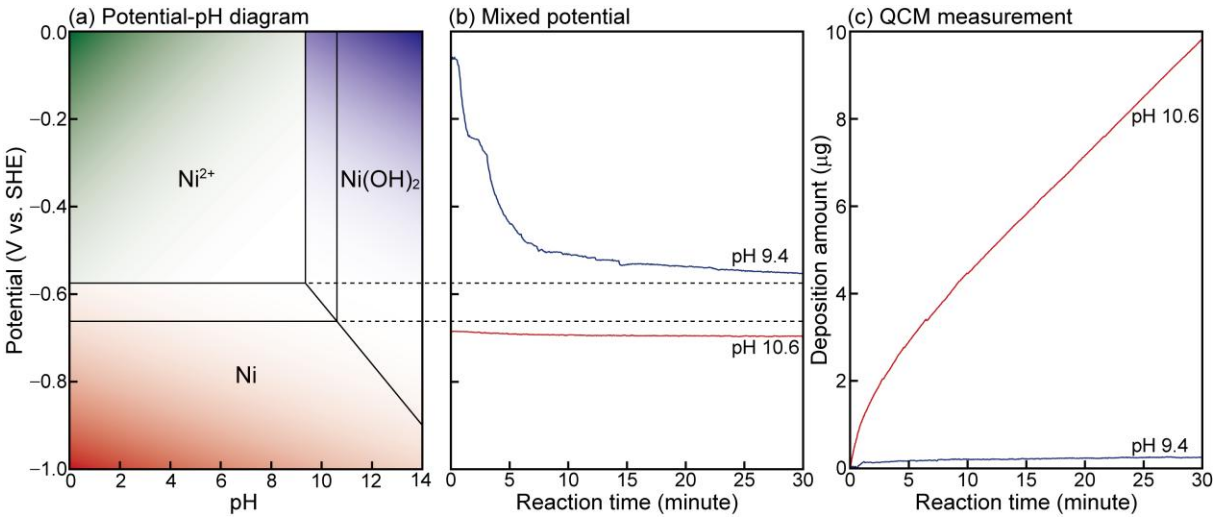

Figure 7.1 (a) Potential–pH diagrams drawn at the equilibrium activities of Ni^{2+} aquo ions at pH 9.4 and 10.6 at 353 K considering the chemical species of Ni^{2+}, $Ni(OH)_2$, Ni, H_2O, H^+, and OH^-. (b) Time dependence of mixed potential and (c) weight change of metal deposited on the gold-sputtered QCM substrate immersed in the solution containing 0.050 M Ni(II) and 0.50 N_2H_4 at pH 9.4 and 10.6.

Table 7.2 List of Gibbs free energy, entropy at 298 K and 1 atm, and specific heat at constant pressure (1 atm) considered and used for thermodynamic calculation.

Chemical speicies	Standard Gibbs free energy $\Delta G^0_{298\,K}$ (kJ mol^{-1})	Standard entropy $S^0_{298\,K}$ (J K^{-1} mol^{-1})	Specific heat at constant pressure $C_p = a + b \times 10^{-3}\,T + c \times 10^5\,T^2$ (J K^{-1} mol^{-1})			References
			a	b	c	
H^+ (aq)	0.0	0.0	0.0	–	–	[5]
H_2O (l)	−237.1	70.0	75.3	–	–	[6]
Ni (s)	0.0	29.9	11.17	37.78	3.18	[7]
Ni^{2+} (aq)	−46.3	−132.2	−41	–	–	[7]
$Ni(OH)_2$ (s)	−458.9	52.9	90	–	–	[7]

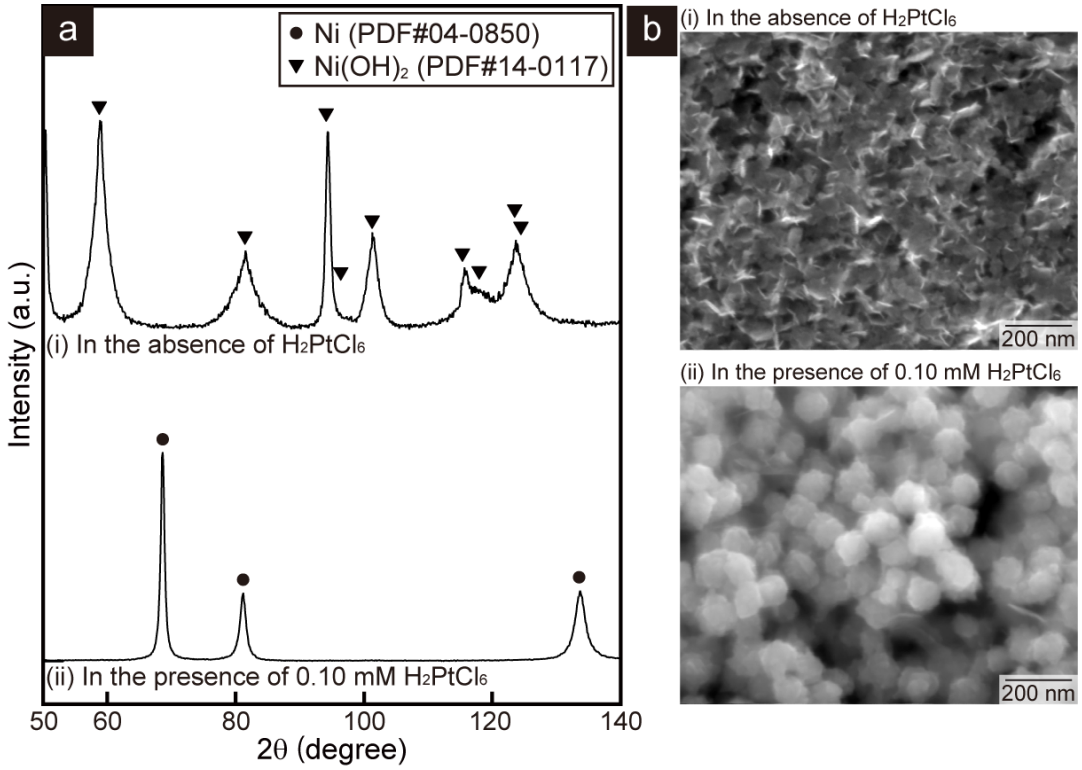

Figure 7.2 (a) XRD patterns and (b) SEM images of the precipitates synthesized at 353 K from the solutions containing 0.050 M $NiCl_2$ and 0.500 M N_2H_4 (i) in the absence of H_2PtCl_6 or (ii) in the presence of 0.10 mM H_2PtCl_6.

Figure 7.3 show the SEM images of nickel particles and wires synthesized from the solutions under a magnetic field at different concentrations of a complexing agent. In the absence of a complexing agent, the nickel particles about 100 nm in diameter were formed. According to the formation mechanism of nanowires,[3] it is necessary to suppress the deposition rate of nickel in order to obtain the nickel nanowires with a smooth surface. For the control of the deposition rate of nickel, $Na_3C_6H_5O_7$ was added as a complexing agent in the reaction solution. As a result, the beads-like nickel wires (Fig. 7.3b) and nickel nanowires with a smooth surface (Fig. 7.3c) were formed at 10.0 and 18.8 mM $Na_3C_6H_5O_7$, respectively. In the solution containing 18.8 mM $Na_3C_6H_5O_7$, NNNC was obtained at about 15 minutes after applying a magnetic field via the formation mechanism[3] schematically

depicted in Figure 7.4a. First, nickel nanoparticles are formed in the solution and aligned along a magnetic field due to the shape magnetic anisotropy, followed by surface smoothing with preferential deposition of nickel at chasms between nanoparticles to lower the interfacial energy. Subsequently, the nanoparticles are tightly connected with each other to become a nanowire, and eventually the nickel nanowires are tangled to form a self-assembled nonwoven cloth. NNNC sheeted by press can be flexibly used as a free-standing electrode as shown in Fig. 7.4b. The scanning electron microscopic (SEM) image shows that NNNC is composed of the three-dimensionally-tangled nickel nanowires of 120 nm in diameter and several dozen μm in length (Fig. 7.4c) It is noted that NNNC has a mechanical strength enough to twist and tie as shown in Figs. 7.4d and e.

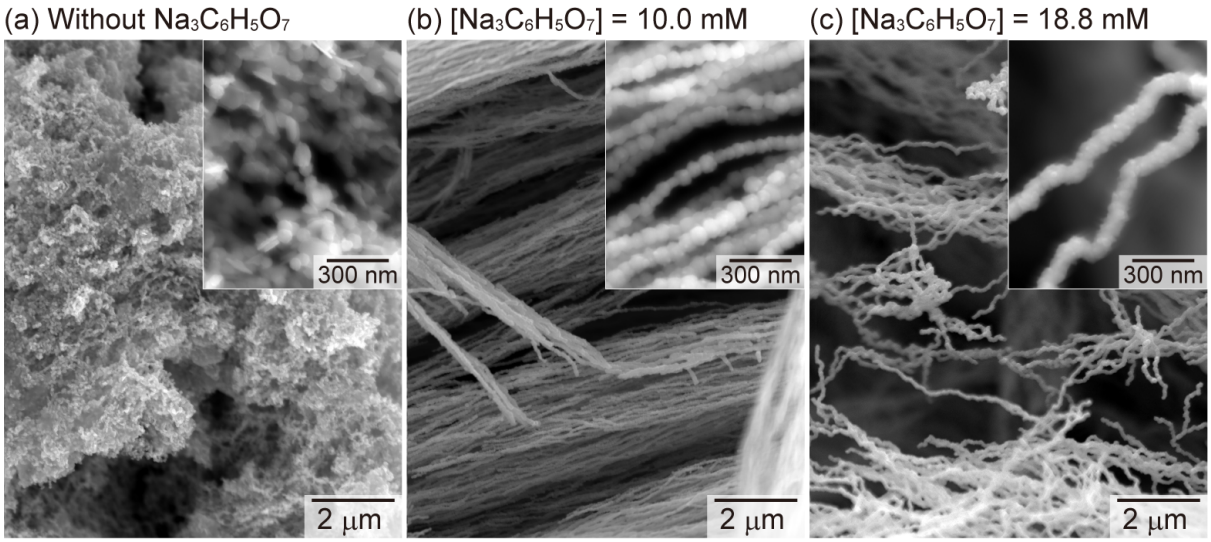

Figure 7.3 SEM images of nickel particles and wires synthesized from solutions containing 0.050 M $NiCl_2$, 0.500 M N_2H_4, (a) 0 mM, (b) 10.0 mM, and (c) 18.8 mM $Na_3C_6H_5O_7$ under a magnetic field.

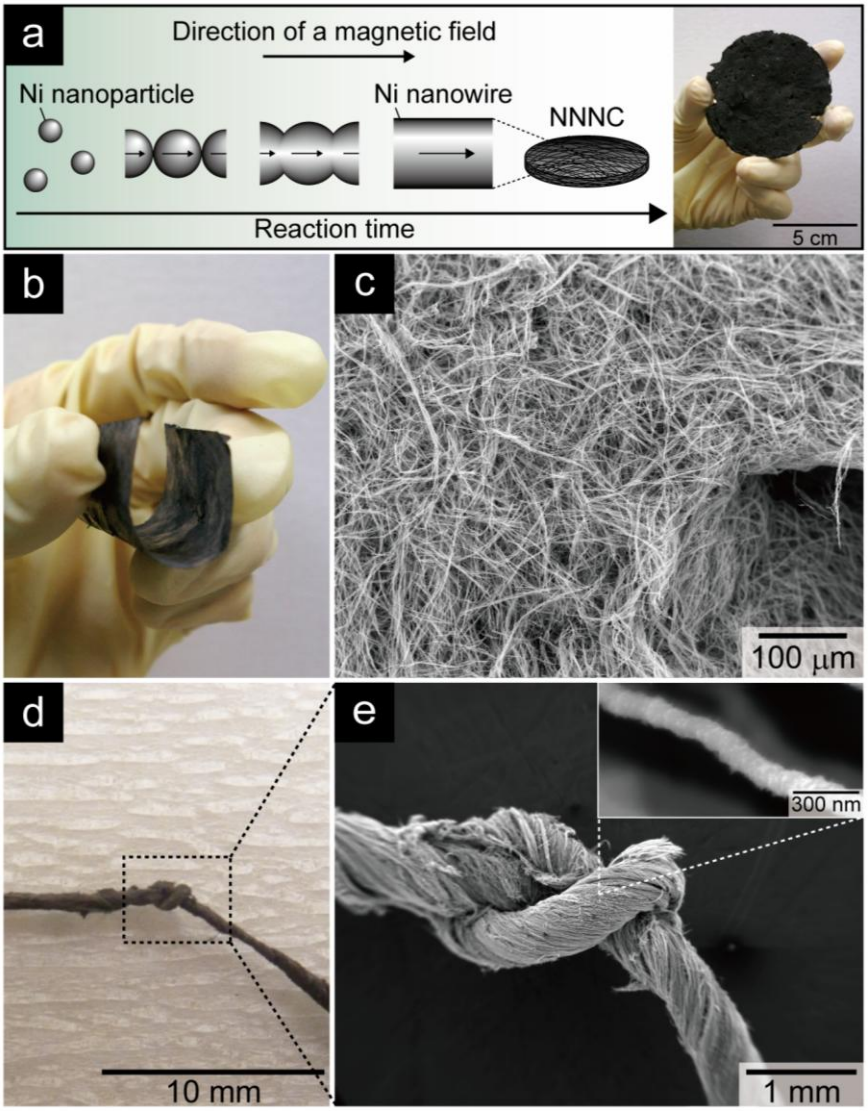

Figure 7.4 (a) Schematic illustration of the formation process of the NNNC synthesized by electroless deposition under a magnetic field. (b) Photographic image and (c) SEM image of the sheet-like NNNC. (d) Photographic image and (e) SEM images of the twisted and tied nickel nanowires.

7.3.2 Formation of NiO-covered NNNCs by heat treatment

Poizot *et al*. reported that nanoparticles of the transition metal oxides, FeO, CoO, and NiO, react with lithium ions at a low potential with a relatively high capacity exceeding 700 mAh/g.[8] According to their paper, the active materials are reported to be of the conversion reaction type,

$$MO + 2Li^+ + 2e \rightarrow M + Li_2O \quad (M = Fe, Co, Ni) , \qquad [7.1]$$

where the redox potential of the conversion reaction for NiO is calculated to be about 1.8 V (vs. Li^+/Li) from the thermodynamic data.[9] Hence, the surface-oxidized NNNC can be used as a negative electrode of LIBs (too low potential as a positive electrode for LIBs), and is a good example to compare the difference between cyclability of the integrated nanowire electrode and the conventional composite electrode.

Figure 7.5a shows the XRD patterns of the nickel nanowires measured before and after anneal at 523-573 K for 16 h. The face-centered cubic (fcc) peaks of nickel (PDF#04-0850) are only observed before anneal. In the XRD patterns of the nanowires after anneal, both fcc Ni and the rock salt type NiO peaks (PDF#04-0835) are observed. The relative intensity of NiO peaks to Ni peaks increases with increasing a heat treatment temperature. Fig. 7.5b shows the SEM images and the size distributions of the nickel nanowires. The mean diameter of the nanowires becomes thicker with an increase in heat treatment temperature due to the growth of a nickel oxide layer.[10] The mean diameter of the nanowires annealed at 573 K is 215 nm which is 1.8 times thicker than that of pristine nanowires. Figure 7.5c shows the atomic ratio of oxygen to nickel (the oxidation ratio) in NNNCs evaluated by the EDX analysis and the mass measurement. The oxidation ratio of the nickel nanowires increases with an increase of heat treatment temperature. According to the mass measurement, the oxidation ratios are about 12, 15, and 39% for NNNC prepared at the heat treatment temperature of 523, 543, and 573 K, respectively, which is in good agreement with the result of the EDX analysis. The transmission electron microscopic (TEM) images show that a thin nickel oxide layer of 20 nm forms on the nickel nanowires annealed at 523 K (Fig. 7.5d), indicating the NiO-covered NNNC is fabricated by the simple processes with the electroless deposition and the heat treatment.

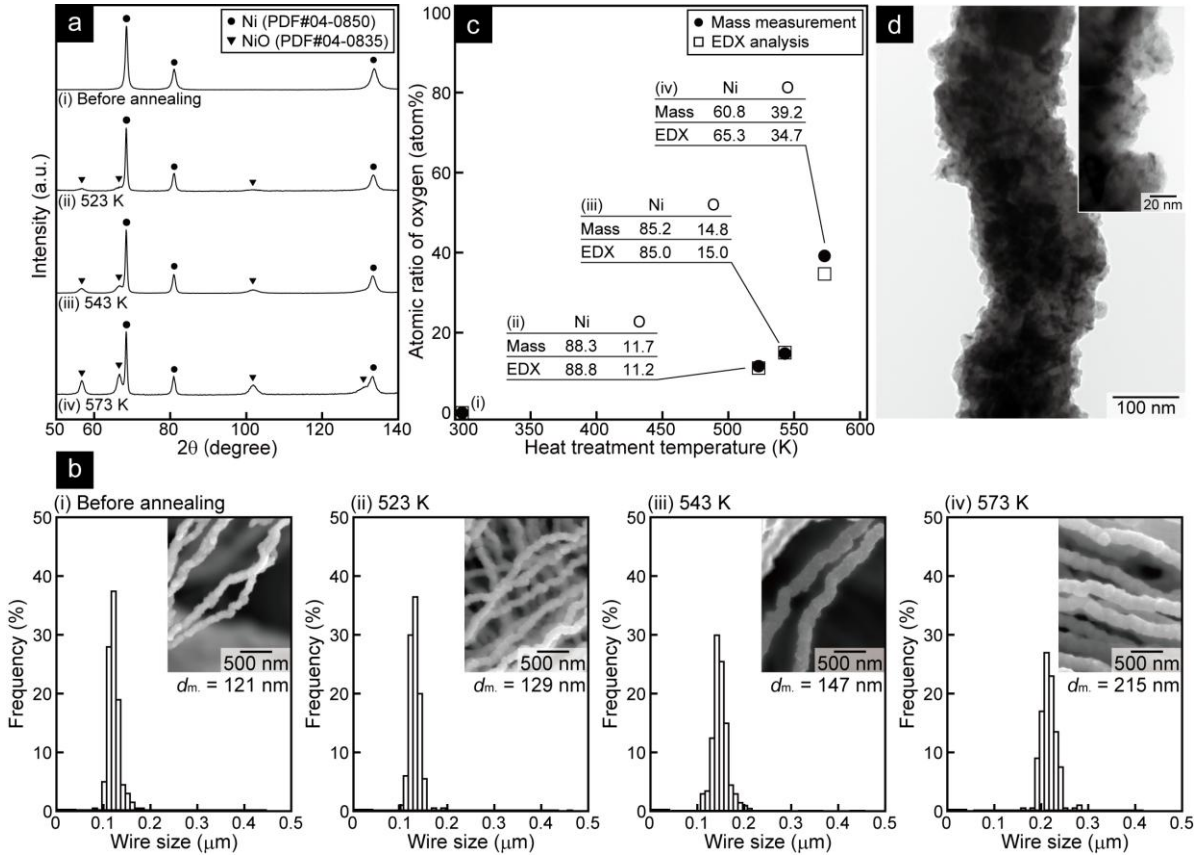

Figure 7.5 (a) XRD patterns, (b) SEM images and diameter size distributions, and (c) atomic ratios of oxygen of the nickel nanowires (i) before and after anneal at (ii) 523, (iii) 543, (iv) 573 K. (d) TEM images of the nickel nanowires obtained after anneal at 523 K.

7.3.3 Electrochemical performances of NiO-covered NNNCs

To examine whether the NiO-covered NNNCs indeed act as a conversion-type electrode, the cyclic voltammogram (CV) of the NNNCs annealed at 523 K was measured using a solution of ethylene carbonate (EC) and dimethyl carbonate (DMC) with a 1:2 volume ratio containing 1 M $LiPF_6$. As shown in Figure 7.6, in the first cathodic sweep, a strong cathodic current is observed below 1.0 V (vs. Li^+/Li), which corresponds to the conversion reaction and the formation of a solid-electrolyte interface (SEI) and/or a polymer/gel-like film containing LiF, Li_2CO_3, and lithium alkyl carbonate.[11] Since the redox potential of the conversion reaction in the NiO active material is calculated to be 1.79 V (vs. Li^+/Li) from the

thermodynamic data,[9] the overpotential for the conversion reaction at the first cycle is found to be large. The anodic current is always observed around 1.0 to 1.7 V in all the anodic sweeps, which is due to the reversible formation/dissolution process of the polymer/gel-like film showing the pseudocapacitive nature.[12] In the anodic sweep, the reverse reaction of the conversion reaction, $Ni + Li_2O \rightarrow NiO + 2Li^+ + 2e$, proceeds above 1.8 V, and after the first cycle, the cathodic onset of the conversion reaction shifts from 0.8 V to 1.6 V, that is, the conversion reaction proceeds with a smaller overpotential after the first cycle. This CV is the typical profile of the NiO conversion-type electrode as reported in the literature.[13,14]

Figure 7.6b shows the galvanostatic charge-discharge curves of the NNNC annealed at 523 K in the voltage range between 0.02-2.50 V at a rate of C/10 and 1 C. The weight of NiO obtained by the mass-change measurement was used for the evaluation of the weight capacity and the C rate of each sample. In the first discharge, the potential drop is observed and becomes stable at about 0.8 V. The first discharge capacity was about 1800 mAh/g, which is much higher than the theoretical capacity of 718 mAh/g due to the formation of the SEI and/or the polymer/gel-like surface film already shown as the large peak below 1.0 V in the first cycle of CV (Fig. 7.6a). The irreversible capacity of 610 mAh/g is observed after the first charge, which reflects the irreversible reaction of the film formation during the first discharge. The irreversible capacity significantly decreased after the first cycle. The second discharge proceeds at a higher potential compared to that at the first cycle, indicating the conversion reaction occurs reversibly with a smaller potential hysteresis once the reaction proceeds. This is consistent with the result of the CV measurements in Fig. 7.6a that the overpotential for the conversion reaction becomes lower after the first cycle.

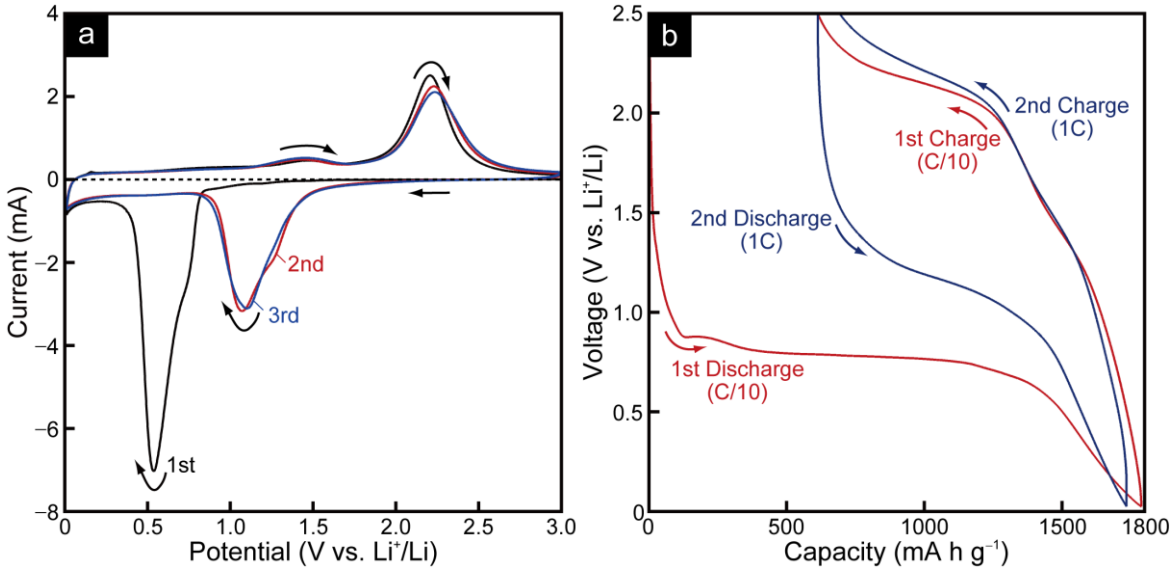

Figure 7.6 (a) Cyclic voltammogram of the NNNC annealed at 523 K measured at a scan rate of 0.1 mV s^{-1} in a solution of 33% ethylene carbonate and 67% dimethyl carbonate containing 1 M $LiPF_6$. The cycle numbers are indicated in the graph. (b) Galvanostatic charge-discharge curves of the NNNC annealed at 523 K in the voltage range 0.02-2.50 V (vs. Li^+/Li) at a rate of C/10 and 1 C for the first and second cycles, respectively.

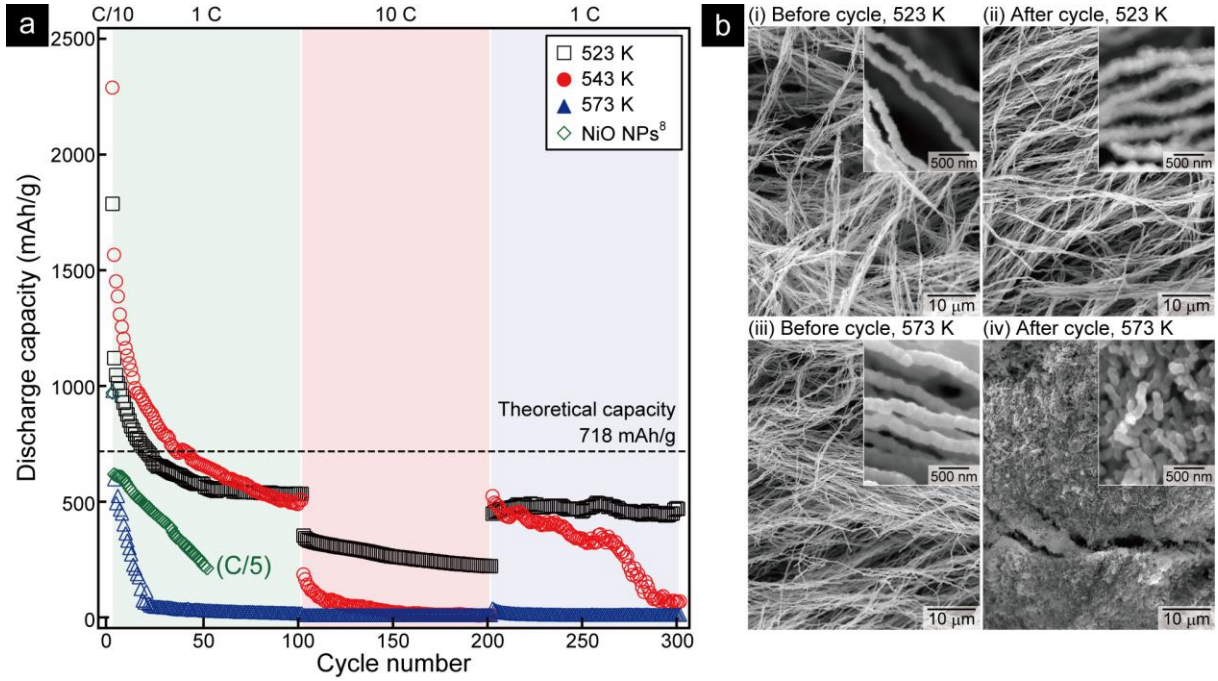

Figure 7.7 (a) Cycle performance of the NNNCs annealed at various temperatures. The charge-discharge experiments were conducted at room temperature between 0.02 and 2.50 V at a rate of C/10, 1 C, and 10 C. The capacity of the composite electrode with NiO nanoparticles, which was reported by Poizot *et al*.,[8] is also indicated for comparison. (b) SEM images of the NNNCs annealed at 523 and 573 K measured before and after the 300 cycles of charge-discharge experiments as shown in (a).

Figure 7.7a shows the discharge capacities measured at different C rates for NNNCs annealed at various temperatures. The first cycle was conducted at C/10 and the current densities were changed to 1 C, 10 C, and 1 C in each 100 cycle. The cycle performance of a composite electrode with NiO nanoparticles at C/5 reported by Poizot *et al*. is also shown for comparison.[8] NNNC annealed at 523 K exhibits best cycle performance compared to the electrodes annealed at 543 and 573 K. The discharge capacity of the electrode annealed at 523 K can be kept constant at 550 mAh/g after the 50 cycles. Even at a higher current density of 10 C, the electrode is shown to exceed 220 mAh/g during the 100 cycles, and, subsequently when returning to 1 C, the capacity is back to 500 mAh/g and is kept constant without fading during the next 100 cycles. For the electrode annealed at 573 K, the capacity decreases with the cycle number and drops down below 50 mAh/g after 20 cycles. Thus, the NiO-covered NNNC annealed at 523 K shows the prominent cycle performance, except for the large irreversible capacity due to the formation of surface films enhanced by its large specific surface areas.

Figure 7.7b shows the SEM images before and after the charge-discharge experiments. For the electrode annealed at 523 K, as found from Figs. 7.7b (i) and (ii), the 3D interconnected structure remains unchanged after 300 cycles and pulverization of the nanowires is hardly observed. Moreover, certain thin films are observed on the surface of the nickel nanowires after many cycles [see the inset of Fig. 7.7b (ii)], which would be formed due to the large irreversible capacity observed in the early cycles. In contrast, for the electrode annealed at 573 K, pulverization is noticeable and many clacks are observed after the cycles in Fig. 7.7b (iv), which is due to the embrittlement of the nanowires accompanied with an increase in the fraction of NiO by annealing at a higher temperature. The pulverization of the electrode results in the lack of an electronic conducting path, leading to

the rapid degradation in the discharge capacity as shown in Fig. 7.7a. Therefore, the control of the fraction of nickel oxide in the nickel nanowires is the key factor to fabricate a high-cyclability NiO-covered NNNC electrode that possesses a mechanical flexibility to tolerate a volume change during the lithiation/delithiation process; in the present study, this was achieved by oxidizing the surface of the NNNC for 12%. Consequently, we could obtain an excellent electrode that exhibits a much higher cyclability compared to that for the NiO nanoparticle composite electrode[8] even at the higher C rate used in the present experiment. This strongly indicates that the integrated nanowire electrode is superior to the conventional composite electrode in terms of the cyclability and rate capabilities.

7.4 Conclusions

In conclusion, we have proposed a novel concept of an electrode design "integrated nanowire electrode" by using the metal-nanowire-nonwoven cloth (MNNC). The electrode proposed here consists simply of an active material deposited or coated on MNNC, which does not need any binders, conductive additives, and current collectors. Due to its structural simplicity with keeping the nanoscale of the metal nanowires, the electrode has high surface areas and sufficient interspaces, which can provide efficient ion/electron transports and accommodate a large volume change accompanied by lithiation/delithiation processes, and thereby it shows a high cyclability. As a prototype of the MNNC-based electrode, we fabricated the NiO-covered NNNC by the electroless deposition and the annealing to demonstrate the high cyclability of the MNNC-based electrode; the adequately-annealed NNNC exhibit a better cycle performance in the conversion reaction, compared to the composite electrode with NiO nanoparticles.

The unique structure of nonwoven cloth comprised of core-clad type nanowires has

several advantages for LIB electrodes, which can be sorted out as follows; (i) The MNNC-based electrode can be used as a flexible electrode without any binders due to its 3D interconnected architecture. (ii) The MNNC ensures the interspaces between respective nanowires, which yields the large electrolyte/nanowires interfaces. (iii) The electrolyte-filled interspace enables rapid Li-ion transports. (iv) The interspaces and the loose textures of the electrode can accommodate drastic volume changes of the active materials accompanied by lithiation/delithiation processes. (v) The electrode requires no current collectors because the core of nanowires provides the electronic path ways. (vi) The thin clad layer of active materials minimizes the effect of sluggish solid-state ion transports. Namely, this electrode design "integrates" all functions which are hitherto assumed by four components in the composite electrode, and thereby the electrode can solely work as an LIB electrode.

Here we only presented the case of NiO active material showing the conversion reaction. In the NiO conversion reaction, the total volume of Ni + Li_2O is about 2.5 times as large as that of NiO. Nevertheless, we have successfully demonstrated that the present MNNC-based electrode can be substantially sustained after 300 cycles. Therefore, fundamentally this MNNC-based electrode can be widely produced by replacing NiO with a more attractive high capacity/low potential active material such as Si or Sn, in which significant volume change accompanied by the lithiation and delithiation process affects the cyclability as well.

References

1. M. Armand, J.-M. Tarascon, *Nature*, **451**, 652 (2008).
2. J.-M. Tarascon, M. Armand, *Nature*, **414**, 359 (2001).
3. M. Kawamori, S. Yagi, E. Matsubara, *J. Electrochem. Soc*., **158**, E79 (2011).
4. M. Kawamori, S. Yagi, E. Matsubara, *J. Electrochem. Soc*., **159**, E37 (2012).
5. J. Chivot, L. Mendoza, C. Mansour, T. Pauporté, and M. Cassir, *Corr. Sci.*, **50**, 62 (2008).
6. D. R. Stull, and H. Prophet, *JANAF Thermochemical Tables*, 2nd ed., NSRDS-NBS, Washington, DC (1971).
7. B. Beverskog and I. Puigdomenech, *Corr. Sci.*, **39**, 969 (1997).
8. P. Poizot, S. Laruelle, S. Grugeon, L. Dupont, J.-M. Tarascon, *Nature*, **407**, 496 (2000).
9. P. Poizot, S. Laruelle, S. Grugeon, J.-M. Tarascon, *J. Electrochem. Soc*., **149**, A1212 (2002).
10. A. Atkinson, R. I. Taylor, and P. D. Goode, *Oxidation of Metals*, **13**, 519 (1979).
11. G. Gachot, S. Grugeon, M. Armand, S. Pilard, P. Guenot, J.-M. Tarascon, S. Laruelle, *J. Power Sources*, **178**, 409 (2008).
12. S. Laruelle, S. Grugeon, P. Poizot, M. Dolle, L. Dupont, J-M. Tarascon, *J. Electrochem. Soc*., **149**, A627 (2002).
13. X. H. Huang, J. P. Tub, C. Q. Zhang, F. Zhou, *Electrochim. Acta*, **55**, 8981 (2010).
14. B. Varghese, M. V. Reddy, Z. Yanwu, C. S. Lit, T. C. Hoong, G. V. S. Rao, B. V. R. Chowdari, A. T. S. Wee, C. T. Lim, C.-H. Sow, *Chem. Mater*., **20**, 3360 (2008).

Chapter 8

Summary

The iron group metallic nanomaterials (i.e., nanoparticles, nanowires, and nanowire-nonwoven cloths) are attractive for a wide variety of applications, such as magnetic, catalytic, and battery materials. Among numerous synthesis methods of iron group metallic nanomaterials, the electroless deposition is especially one of the promising approaches for practical applications, however, the fabrication of nanomaterials by electroless deposition is existential, and the reaction solutions have been optimized by a repeated trial and error method. In the present work, for the quantitative assessment of the reaction system, the electrochemical in-situ measurements are proposed and applied them to the synthesis process of iron group metallic nanomaterials via electroless deposition. In the first fundamental part (chapters 2-6), we attempted to obtain policies for designing of iron group metallic nanomaterials by using the electrochemical measurements. In the second application part (chapter 7), based on the electrochemical investigation, we have fabricated a novel metal-nanowire-nonwoven cloth (MNNC) and applied it to electrodes of Li ion batteries (LIBs). The results obtained in this study are summarized as follows;

Chapter 2 Application of Electrochemical in-situ Measurements for Formation of Cobalt Nanoparticles in Aqueous Solution

The formation of cobalt particles in aqueous solution was electrochemically investigated. The deposition behavior of cobalt is strongly affected by pH of a solution; the formation of cobalt particles is more favorable at a higher pH. For evaluation of the driving force of metal deposition, the mixed potential was measured and compared with the

thermodynamically calculated potential-pH diagram. The mixed potential becomes lower at a higher pH, and the cobalt deposition is observed from the aqueous solution of pH 11.9 at 353 K, where the mixed potential is lower than the redox potential of Co^{2+}/Co redox pair. We have experimentally demonstrated that the mixed potential is the effective indicator of the reduction ability in the reaction solution, which is useful for the prediction of what chemical species will be synthesized via electroless deposition.

Chapter 3 Application of Electrochemical in-situ Measurements for Formation of Cobalt Nanoparticles in Nonaqueous Solution

Owing to the lack of thermodynamic data, the thermodynamic calculation cannot be easily adopted to reaction systems in nonaqueous solutions, which are often used as a solvent for the syntheses of iron group nanoparticles by electroless deposition. Therefore, it is necessary to experimentally obtain the redox potential of metal, however, the reduction current of relatively-less noble metals (Fe, Co, Ni, etc.) is hardly separated from the total current by the usual voltammetry due to the large contribution of the decomposition of the solvent. Hence, both a weight of deposited metal and a total current of the electrochemical reaction are simultaneously measured by EQCM method.

The formation of cobalt particles is strongly affected by a concentration of N_2H_4; the cobalt deposition is more favorable at a higher concentration of N_2H_4. The driving force of metal deposition in nonaqueous solution is evaluated by comparison of the mixed potential and the redox potential of metal experimentally obtained by EQCM. The mixed potential becomes lower at a higher concentration of N_2H_4, and the cobalt particles are formed by the homogenous nucleation at a high concentration of N_2H_4 0.50 M, where the mixed potential is much lower than the redox potential of Co(II)/Co redox pair. By using the in-situ mixed

potential measurement in conjunction with EQCM method, we have experimentally demonstrated that the driving force of metal deposition can be evaluated even in nonaqueous system, which is especially effective in the reaction systems where thermodynamic data are insufficient.

Chapter 4 Formation of Nickel Nanowires via Electroless Deposition under a Magnetic Field

The effect of an external magnetic field on the formation of metallic nanoparticles was investigated by using the electrochemical in-situ measurements. The deposition behavior of nickel is strongly affected by a concentration of NaOH; the formation of nickel wires is more favorable at a lower concentration of NaOH. The electrochemical measurements revealed that the reduction ability of hydrazine oxidation reactions becomes lower at a lower concentration of NaOH, resulting in a longer terminal time of the nickel deposition reaction and realizing the formation of smooth nickel wires. The morphological change in nickel wires is explained by the formation mechanism; first, nickel particles are formed and aligned along a magnetic field due to the magnetic shape anisotropy, followed by the nickel deposition on their surface. Then, they are tightly connected and become a wire. Therefore, the necessary condition for the formation of nickel wires is that the alignment of particles occurs prior to the completion of the reduction reaction. According to the mechanism, nickel wires 100 - 370 nm in diameter with several dozen μm of length were successfully prepared by controlling the reduction rate by varying a concentration of sodium hydroxide, trisodium citrate, and chloroplatinic acid.

Chapter 5 Nickel Alloying Effect on Formation of Cobalt Nanoparticles and Nanowires

The alloying effect on the formation of metallic nanoparticles and nanowires was investigated by using the electrochemical in-situ measurements, taking Co-Ni system as an example. The deposition behavior of Co-Ni is strongly affected by a concentration ratio of Ni(II); the smaller particles and thinner wires are formed at a higher concentration ratio of Ni(II). The nickel alloying effect on the formation of cobalt nanoparticles and nanowires can be explained by different electrode behaviors between cobalt and nickel in the oxidation reactions of hydrazine and the reduction reactions of metallic ions. The current of both reactions is much smaller on nickel than that on cobalt, indicating that the growth rate of nickel particles is lower than cobalt. An inhibiting effect on the Co-Ni particle growth by the addition of Ni(II) becomes stronger with increasing a concentration of Ni(II) and the nucleation is prompted in comparison. This is the formation mechanism of the smaller particles and thinner wires at a higher concentration ratio of Ni(II). Additionally, the different electrode behavior between cobalt and nickel results in a small composition gradient in Co-Ni alloy particles, where cobalt-rich core of particles mainly has the hcp phase and the edge of particles has the fcc phase.

The morphology of Co-Ni nanowires is also strongly affected by the magnetization of Co-Ni alloy nanoparticles which are precursors in the formation of nanowire, for example, a lower deposition rate is required in fabrication of smooth wires whose magnetization is relatively weak, such as nickel. Both the magnetization and the deposition rate in Co-Ni alloys are the key parameters to control the aspect ratio and surface morphology of nanowires.

Chapter 6 Iron Alloying Effect on Formation of Cobalt Nanoparticles and Nanowires

The formation process of iron-based nanomaterials is more complex compared to that of Co-Ni nanomaterials owing to the presence of trivalent iron ions, and thus, there are several theories as to the formation mechanism of iron nanoparticles. Therefore, the formation process of iron and Fe-Co alloy particles and wires was electrochemically investigated. The in-situ mixed potential measurement revealed that the Fe(II), rather than EG and N_2H_4, works as a strong reducing agent in the formation of iron particles. The deposition behaviors of Fe-Co alloys is strongly affected by the different electrode behavior between iron and cobalt. The Fe-Co alloy with a higher concentration ratio of iron has the lower catalytic activity in the oxidation reaction of N_2H_4, which results in the lower growth rate of Fe-Co particles at a higher concentration of Fe(II). The inhibiting effect of the particle growth becomes more noticeable at a higher concentration of Fe(II), which definitely affects the deposition behaviors, such as morphologies and yields, of Fe-Co particles and nanowires synthesized by N_2H_4 reduction. For example, pure cobalt and Fe-Co alloy wires can be obtained by N_2H_4 reduction owing to the relatively high catalytic activity, while iron wires are difficult to fabricate because of the low catalytic activity. Based on the result of the mixed potential measurement, the iron nanowires can be successfully prepared by disproportionation reaction under a magnetic field.

The experimental results obtained in chapters 5 and 6 clearly show that the formation of particles and wires is strongly affected by its own electrode behavior in both the reduction reaction of metallic ions and the oxidation reaction of reducing agents. Thus, in order to fabricate the particles and wires with desired morphologies, composition ratios, and crystal structures, we should pay attention to the electrode reactions of metal which have been extensively studied through the ages. In addition, the electrochemical in-situ measurements

enable us to monitor a reduction ability in a solution and the deposition behaviors of metal, which is effective for the optimization of the reaction solution. In the present work, we showed the case of iron group metallic nanomaterials, but fundamentally, the electrochemical analysis approach conducted above can be widely applied in other systems and helps us to thermodynamically and kinetically consider even those systems where insufficient thermodynamic data are available.

Chapter 7 (*Application part*)

Application of Metal-nanowire-nonwoven Cloth for a New Type of High-cyclability Integrated Electrode

Based on the formation mechanism of metallic nanoparticles and nanowires, we designed MNNC, which has great potential to a lot of applications which cannot be achieved by existing nanomaterials. As an application of MNNC, for example, we applied it to LIB electrodes.

Commercially widespread Li storage batteries currently employ composite electrodes consisting of binders, conductive additives, and current collectors. In terms of the cyclability and capacity, however, they are encountering the limitation. In the present work, we propose a new design of high-cyclability integrated-nanowire electrode based on a MNNC, in which an active material is deposited or coated on MNNC. The proposed electrode can work without any binders, conductive additives, and current collectors. Huge electrode surfaces provide efficient ion/electron transports, and sufficient interspaces between the respective nanowires accommodate large volume expansions of the active material.

To demonstrate these advantages, we have fabricated a NiO-covered nickel-nanowire-nonwoven cloth (NNNC) as a prototype by a simple two-step method. First,

NNNC was synthesized in an aqueous solution via electroless deposition under a magnetic field and, subsequently, annealed in air to obtain the core-clad structure of the NiO-covered nickel nanowires. The adequately-annealed NNNC was shown to be an excellent conversion-type electrode that exhibits a quite high cyclability, 500 mAh/g at 1 C after 300 cycles, compared to that of a composite electrode consisting of NiO nanoparticles. Thus, the present design concept will contribute to a game-changing technology in future LIB electrodes.

In the present work, we only demonstrated the application of MNNC to the negative electrode of LIBs, however, it will have strong potential to other applications. MNNC will show the diverse properties by conventional metallurgical treatments (e.g. electroplating, electroless deposition, alloying, carburizing, surface treatment by sol-gel method), which leads to the wide range of applications, as summarized in Figure 8.1. For example, MNNC coated with a high capacity/low potential active material such as Si or Sn will be a candidate of negative electrode for the future LIBs. MNNC coated with catalytic nanoparticles can be used as a catalytic electrode. In addition, MNNC works as a template for nonwoven-nanotube cloths. Finally, the author wishes that the electrochemical analysis approaches and MNNCs established in the present work will contribute to the advance in materials science.

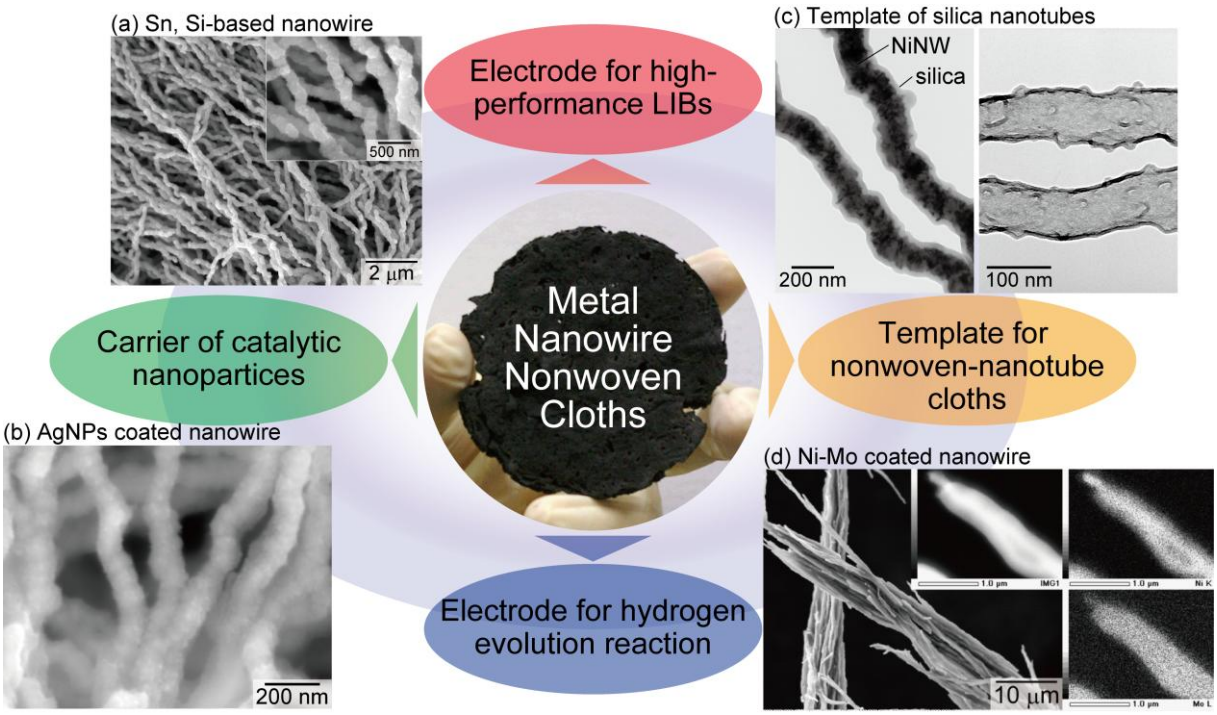

Figure 8.1 Schematic illustration of future applications of MNNCs. (a) SEM images of Sn-Ni electrodeposited NNNC for electrodes of high-performance LIBs. (b) SEM image of silver nanoparticles-coated NNNC for catalysts. (c) TEM images of silica-coated NNNC and silica nanotubes. (d) SEM images of Ni-Mo electrodeposited NNNC for electrodes of hydrogen evolution reaction.

List of Publications

Papers

1. "Electrochemical QCM Study of the Synthesis Process of Cobalt Nanoparticles via Electroless Deposition"

   Shunsuke Yagi, Makoto Kawamori, and Eiichiro Matsubara,

   Electrochem Solid-State Lett., **13(2)**, E1 (2010).

2. "Electrochemical Study on the Synthesis Process of Co-Ni Alloy Nanoparticles via Electroless Deposition"

   Shunsuke Yagi, Makoto Kawamori, and Eiichiro Matsubara,

   J. Electrochem. Soc., **157(5)**, E92 (2010).

3. "Electrochemical Analysis in Fabrication of Co-Ni Alloy Nanoparticles in Nonaqueous Solution"

   Makoto Kawamori, Shunsuke Yagi, and Eiichiro Matsubara,

   J. MMIJ, **127**, 103 (2011).

4. "Formation of Nickel Nanowires via Electroless deposition Under a Mangnetic field"

   Makoto Kawamori, Shunsuke Yagi, and Eiichiro Matsubara,

   J. Electrochem. Soc., **158(8)**, E79 (2011).

   (Selected for the June 27, 2011 issue of Virtual Journal of Nanoscale Science & Technology)

5. "Nickel Alloying Effect on Formation of Cobalt Nanoparticles and Nanowires via Electroless Deposition Under a Mangnetic Field"

   Makoto Kawamori, Shunsuke Yagi, and Eiichiro Matsubara,

   J. Electrochem. Soc., **159(2)**, E37 (2012).

6. “Iron Alloying Effect on Formation of Cobalt Nanoparticles and Nanowires via Electroless Deposition Under a Mangnetic Field”

   Makoto Kawamori, Shunsuke Yagi, and Eiichiro Matsubara,

   (in preparation)

7. “A New Design of High-cyclability Integrated-nanowire Electrode Based on Metal-nanowire-nonwoven Cloth”

   Makoto Kawamori, Takahiro Asai, Yoshimasa Shirai, Shunsuke Yagi, Masatsugu Oishi, Tetsu Ichitsubo, and Eiichiro Matsubara,

   (in preparation)

Proceedings

1. “Formation of Nickel Nanowires by Electroless Deposition”

   Makoto Kawamori, Shunsuke Yagi, and Eiichiro Matsubara,

   ECS Transactions, **40(30)**, 1 (2012).

Oral Presentation

International congress

1. “Formation of Nickel Nanowires by Electroless Deposition”

   Makoto Kawamori, Shunsuke Yagi, and Eiichiro Matsubara,

   The 220th Meeting of the Electrochemical Society, Boston, Massachusetts, October 9 to 14, 2011

2. “Nickel Alloying Effect on Cobalt Nanoparticles and Nanowires from Different Catalytic Behaviors on Cobalt and Nickel Electrodes”

   Makoto Kawamori, Shunsuke Yagi, and Eiichiro Matsubara

The 221st Meeting of the Electrochemical Society, Seattle, Washington, May 6 to 10, 2012

3. "Fe-Co Alloy Nanoparticles and Nanowires Prepared by Electroless Deposition"
   Makoto Kawamori, Shunsuke Yagi, and Eiichiro Matsubara,
   The 222nd Meeting of the Electrochemical Society, Honolulu, Hawaii, October 7 to 12, 2012

Domestic congress

1. "Fabrication of Cobalt Nanoparticles via Electroless Deposition"
   Makoto Kawamori, Shunsuke Yagi, and Eiichiro Matsubara,
   The 76th Meeting of the Electrochemical Society of Japan, Kyoto, March, 2009
2. "Fabrication of Co-Ni Nanoparticles via Electroless Deposition"
   Makoto Kawamori, Shunsuke Yagi, and Eiichiro Matsubara,
   The Fall Meeting of the Electrochemical Society of Japan, Tokyo, September, 2009
3. "Electrochemical QCM Study of the Synthesis Process of Metallic Nanoparticles in Nonaqueous Solution"
   Makoto Kawamori, Shunsuke Yagi, and Eiichiro Matsubara,
   The 6th Meeting of the Mining and Materials Processing Institute of Japan for Young Researchers and Students, Kyoto, December, 2009
4. "Proposal of Integrated Electrode for Rechargeable Batteries with High Performance"
   Makoto Kawamori, Takahiro Asai, Yoshimasa Shirai, Shunsuke Yagi, Masatsugu Oishi, Tetsu Ichitsubo, and Eiichiro Matsubara,
   The 21st Workshop of the Neo-material Creation, Kyoto, January, 2013

Poster Presentation

International congress

1. "Different Electrode Deposition Behavior in Co and Ni Nanoparticles Formation"

   Makoto Kawamori, Shunsuke Yagi, and Eiichiro Matsubara,

   2010 Joint Symposium on the Materials Science and Engineering for the 21st Century, Daejeon, Korea, June 27 to 30, 2010

2. "Nickel Alloying Effect on Fabrication of Cobalt Nanoparticles in Nonaqueous Solution"

   Makoto Kawamori, Shunsuke Yagi, and Eiichiro Matsubara,

   The 61st Annual Meeting of the International Society of Electrochemistry, Nice, France, September 26 to October 3, 2010

Domestic congress

1. "Fabrication of Cobalt Nanoparticles via Electroless Deposition"

   Makoto Kawamori, Shunsuke Yagi, and Eiichiro Matsubara,

   The 10th Meeting of the Kansai Surface Finishing Society of Japan, Hyogo, December, 2008

2. "Formation of Nickel-based Nanoparticles and Nanowires by Electroless Deposition"

   Makoto Kawamori, Shunsuke Yagi, and Eiichiro Matsubara,

   The 2nd Joint Symposium of Kyoto University GCOE and RIKEN, Kyoto, November, 2011

Acknowledgments

The author would like to express my deep gratitude to Professor Eiichiro Matsubara for invaluable comments, advices, and discussions as well as the ceaseless encouragement through the present work. The author would also like to thank Associate Professor Tetsu Ichitsubo for his insightful suggestions and discussions. The author owes much inspiration to his original ideas and witty advices. The author is deeply grateful to Dr. Shunsuke Yagi for his constant guidance, coaching of the experimental works, and helpful discussions. Thanks to him, I have gained passion for the electrochemistry. The author would like to express my gratitude to Professor Hiroyuki Sugimura and Professor Kuniaki Murase for their valuable advices and educational supports from the baccalaureate degree program to the present work. The author would like to express my thanks to Dr. Masatsugu Oishi and Kenji Kazumi for their assistance in experimental works and helpful discussions.

The author also withes to express my gratitude to Ms. Mari Otogawa and Ms. Tomoe Weedall for a wide variety of support and assistance.

The author would like to express my special thanks to Dr. Yu-ki Taninouchi, Dr. Mary Donnabelle Lirio Balela, Mr. Hidetaka Nakanishi, Mr. Shohei Shiomi, Mr. Tomoya Kawaguchi, Mr. Naoki Kaneko, and Mr. Takahiro Asai for their pleasant assistance and useful discussions. Also, I would like to express my gratitude to all other members of Professor Matsubara’s laboratory.

Finally, the author is particularly grateful to my parents, Kiyofumi Kawamori, Hiroko Kawamori, my grandmother, Fumiko Nishinaka, and my sister, Mio Kawamori for their perpetual support and continuous encouragement.

Makoto Kawamori